Boundary Element Method for Wave Propagation in Partially Saturated Poroelastic Continua

Zur Erlangung des akademischen Grades eines
Doktors der technischen Wissenschaften
ausgeführte Dissertation

eingereicht an der
Fakultät für Bauingenieurwissenschaften
der Technischen Universität Graz

von

Peng Li

Berichter: Prof. Dr.-Ing. Martin Schanz
               Prof. Alexander H.-D. Cheng

Graz, September 26, 2012

Abstract

Wave propagation in partially saturated porous continua is an interesting subject in Civil Engineering, Petroleum Engineering, Bioengineering, Earthquake Engineering, and Geophysics, etc. For such problems, there exist different theories, e.g., an extension of Biot's theory, the Theory of Porous Media and the Mixture theory. Based on the Mixture theory, a dynamic three–phase model for partially saturated poroelasticity is established as well as the corresponding governing equations in Laplace domain. This model is applied to a one dimensional column and the related analytical solution in Laplace domain is deduced.The three different compressional waves, the fast wave, the second, and the third slow waves are calculated and validated with the Biot–Gassmann prediction and Murphy's experimental results. The time domain results are obtained with the convolution quadrature method. Within the limit of a saturation nearly to one the results are as well compared with the corresponding results of saturated poroelasticity. For the three-dimensional governing equations, the fundamental solutions are deduced following Hörmander's method. The boundary integral equations are established based on the weighted residual method. After regularization, spatial discretization, and the time discretization with the convolution quadrature method the boundary element formulation in time domain for partial saturated media is obtained. The implementation is done with the help of the open source C++ BEM library HyENA. Finally, the code is validated with the analytical one-dimensional solutions of the column. Two half-space applications are as well presented.

Zusammenfassung

Die Wellenausbreitung in porösen teilgesättigten Materialien ist von Interesse im Bauwesen, der Erdölindustrie, der Biomechanik, zur Berechnung von Erdbeben, in der Geophysik usw. Die Modellierung kann durch unterschiedliche Theorien erfolgen, wie z.B. eine erweiterte Biot-Theorie, der Theorie poröser Medien oder der Mischungstheorie. Aufbauend auf der Mischungstheorie wird ein Drei–Phasen–Modell aufgestellt und die zugehörigen Grundgleichungen im Bildbereich der Laplacetransformation formuliert. Für die eindimensionale Problemstellung einer teilgesättigten porösen Säule wird eine analytische Lösung präsentiert. Die Zeitbereichslösung wird mit Hilfe der Faltungsquadratur ermittelt. Die drei Kompressionswellen in diesem Modell können damit studiert werden. Diese Ergebnisse werden mit der Biot-Gassmann-Gleichung validiert und mit Experimenten von Murphy verifiziert. Ebenso wird der Grenzfall eines gesättigten Materials mit der entsprechenden Lösung der gesättigten Poroelastizität verglichen. Für die dreidimensionalen Gleichungen werden die Fundamentallösungen mit Hilfe der Methode von Hörmander entwickelt. Die Randintegralgleichungen können damit, ausgehend von der Methode der gewichteten Residuen, formuliert werden. Nach Regularisierung, Diskretisierung im Ort und der Zeitdiskretisierung mit der Faltungsquadratur erhält man

die Randelementmethode im Zeitbereich für teilgesättigte poröse Medien. Die Implementierung erfolgt mit der frei verfügbaren C++-Bibliothek HyENA. Das Programm wird mit der analytischen eindimensionalen Lösung validiert und im Anschluss daran werden zwei Halbraum-Beispiele präsentiert.

CONTENTS

Notation

Except if an explicit statement is made to the contrary, the meaning of the symbols used throughout this thesis corresponds to the following notation list.

General symbols

$a, b, \ldots$	Scalars
$\mathbf{a}, \mathbf{b}, \ldots$	Vectors
$a_i, b_i, \ldots$	Vector components of $\mathbf{a} = \sum_{i=1}^{3} a_i \mathbf{e_i}$
i, j, k	Latin indices taking values $1, 2, 3$
A_{ij}	Matrix element of $\mathbf{A}$
$()_{,i}, \partial_i$	Differentiation with respect to x_i
$()_{,ii}, \Delta$	Laplacian, $\Delta = \sum_{i=1}^{3} \frac{\partial^2}{\partial x_i^2}$
$a_{,i}$	Gradient of scalar field a in component notation
$a_{i,i}$	Divergence of vector field $\mathbf{a}$ in component notation
$a_{i,j}$	Gradient of vector field $\mathbf{a}$ in component notation
$\nabla \cdot \mathbf{a}$	Divergence of vector field $\mathbf{a}$ in symbolic notation
∇	Nabla operator $\nabla = \sum_{i=1}^{3} \mathbf{e_i} \frac{\partial}{\partial x_i}$
$\mathcal{L}$	Differential operator
δ_{ij}	Kronecker delta
x_i	Components of location vector $\mathbf{x} = \sum_{i=1}^{3} x_i \mathbf{e_i}$
t	Time
ω	Angular frequency
i	Imaginary unit $i = \sqrt{-1}$

Special symbols

V	Volume
n	Porosity
ρ_s	Solid density
ρ_w	Wetting fluid density
ρ_a	Non–wetting fluid density
u_i	Components of solid displacement vector

p^w	Wetting fluid pore pressure
p^a	Non–wetting fluid pore pressure
p^c	Capillary pressure, $p^c = p^a - p^w$
p^d	Non–wetting fluid entry pressure
v_{p_i}	Fast / slow compressional wave speed, $i = 1, 2, 3$
a_{p_i}	Fast / slow compressional wave attenuation, $i = 1, 2, 3$
v_s	Shear wave speed
v_r	Rayleigh wave speed
F_i	Components of bulk body force vector
I^w, I^a	Components of fluid source terms
σ_{ij}	Components of total stress tensor
σ'_{ij}	Components of effective stress tensor
ϵ_{ij}	Components of solid strain tensor
E	Young's modulus
ν	Poisson's ratio
G	Shear modulus
K	Bulk modulus of the mixture
K_s	Bulk modulus of the solid skeleton
K_f	Bulk modulus of the fluid, $f = w, a$
S_f	fluid saturation, $f = w, a$
S_e	Effective wetting fluid saturation
ϑ	Pore size distribution
S_{rw}	Residual wetting fluid saturation
S_{ra}	Non–wetting fluid entry saturation
α	Biot's effective stress coefficient
β, γ	Dimensionless, frequency dependent quantity
κ_f	Fluid permeability, $f = w, a$
η_f	Fluid viscosity, $f = w, a$
k	Intrinsic fluid permeability
K_{rf}	Relative fluid phase permeability, $f = w, a$
q_i	Components of fluid flux vector $\mathbf{q}$
n_i	Components of outward normal vector $\mathbf{n}$
$\mathcal{B}$	Differential operator for partially saturated poroelasticity
$\mathcal{L}\{f(t)\}$	Laplace transform of $f(t)$
$\hat{()}$	Laplace transform, $\hat{()} = \mathcal{L}\{()\}$
$\mathbf{U}$	Fundamental solutions
Ψ	Solution of the Helmholtz equation
$\mathbf{S}$	Surface curl
$\mathcal{M}$	Günter derivatives
$\hat{\mathcal{T}}^e$	Elastic stress operator
$\hat{\mathcal{V}}$	Single layer operator

$\hat{\mathcal{K}}$	Double layer operator
$H(t)$	Heaviside step function
β_{CFL}	Courant–Friedrichs–Levy number
r_e	Characteristic element length
Ω	Domain
$\Gamma, \partial\Omega$	Boundary of Ω

1 INTRODUCTION

Elastic wave propagation in porous media is of great importance in many areas of applied science and engineering as acoustics, geomechanics, biomechanics, petroleum engineering, geophysics, materials science, etc. In geotechnical engineering, the porous media are mainly soils and rocks. The analysis of such geomaterials under dynamic loadings is of great interest for various applications in the field of geotechnical engineering as pile driving, dynamic compaction, vibratory isolation, earthquake engineering, etc.

Generally, under natural conditions, absolutely saturated or dry geomaterials may never exist but in a state of partially saturation. This partially saturated medium may have a property of multiphase coupling (solid phase, liquid phase, gas phase). In other words, it has a property of multifield coupling such as, coupling of stress and seepage field (e.g., earth and rockfill dam), coupling of stress and temperature field (e.g., mass concrete pouring), coupling of stress, temperature, and chemical field (e.g., landfill), etc. The partially saturated medium has a structure of solid skeleton and distributed pores filled with different viscous fluids. The fluids can be either continuous or discontinuous in the pores depending on the corresponding degrees of saturation. The pore fluids can affect the physical characteristics of the porous medium a lot, while one important effect is the damping of the wave propagation in this medium caused by the fluid viscosity. For wave propagation in saturated poroelasticity, it is well–known that there is a so called slow compressional wave caused by the interactions between the solid and the pore fluid, beside the fast compressional wave and the shear wave. For partially saturated case, where there may be more than two different pore fluids, the interactions of the multiphases are more complex. Therefore, besides the slow compressional wave, a slower compressional wave exists for a partially saturated porous medium with a wetting and a non–wetting fluid in the pores. However, due to the extreme high attenuation of the slow compressional waves, they (i.e., the second and the third slow compressional wave) are difficult to be detected. Beside the porosity, the degree of saturation has an obvious influence on the waves including the wave speed and wave attenuation. It can be easily understood that the value of the saturation degree can affect the average compressibility of the porous medium. The interaction between the solid and the fluids can also be affected by the value of the saturation degree. The concept of surface tension and capillary pressure is of special interest, and they may have great effects on the partially saturated porous medium such as the dynamic response.

The governing equations for a partially saturated poroelastic continuum can be derived based on the usual equations in continuum mechanics, where an analytical solution may be obtained only for a special choice of boundary conditions. This analytical solution is

sometimes quite useful because it is much easier to be applied and implemented, besides, it can be used to validate the corresponding numerical results. Applications of numerical methods such as finite element method (FEM), boundary element method (BEM), finite difference method (FDM), etc, only the finite element method in the field of partially saturated soil is known from literature [71]. FEM and FDM are two powerful numerical methods which can almost model any complex geometry and are easy to be implemented. Unfortunately, for the three dimensional case both need volume discretization which are time consuming. Compared with FEM and FDM, for BEM, only a mesh of the boundary is required which is more efficient for the construction of meshes for complicated objects. The values on the boundary (more interesting for most problems) are calculated first, then the values inside the domain can be calculated. The tractions have the same accuracy as the displacements. The approximation only happens on the boundary. Besides, BEM is quite suitable for semi–infinite and infinite domain problems such as wave propagation. On the other hand, disadvantages also exist. The so called fundamental solution must be known. Fully populated non–symmetric matrices are introduced. The integrals are more difficult to evaluate because of the existing weak, strong or hyper singularities. This method can not be straight forward applied to non–linear or non–homogeneous problems. Finally, the implementation work might be much more difficult.

1.1 State of the art

Partially saturated poroelasticity.   According to volume relationships and movement properties of the fluids in the pores, the porous media can be divided into the following different types:

1. Dry media: The non–wetting fluid is continuous in the solid skeleton, and there is no free wetting fluid flow. The saturation degree of this type of porous media is zero;

2. Low saturated media: The pores are occupied by both the wetting and non–wetting fluids but with less wetting fluid. The wetting fluid is not continuous, and is not an unconfined flow;

3. Intermediate saturated media: Both of the wetting and non–wetting fluids can flow freely in the pores;

4. High saturated media: The non–wetting fluid can not flow freely but only exist in the pore wetting fluid and it might have an obvious effect on the wetting fluid flow;

5. Saturated media: Only the wetting fluid exist in the pores while the saturation degree turns to 1.

All the five different types of porous media may be called partially saturated media where the dry and saturated media are two extreme cases.

For saturated porous media there are in principle three similar theories available – that of Biot [16, 17], the Theory of Porous Media (e.g., [42]), and the simple mixture theory [126]. The latter ones are based on the principles of continuum mechanics and the mixture theory. Their extension to the partially saturated case may be found in [71]. Another approach for porous media like rocks is the double porosity model based on Biot's theory [128].

The pore fluids flow for partially saturated media include the wetting fluid flow and the non–wetting fluid flow where both are driven by the respective pressure gradient. For the saturated case, Darcy's law [41] is often used to describe the pore fluid flow and the applicability has been validated by Biot's theory [18] and the mixture theory [25]. Darcy's law is also suitable for the unsaturated case which can be used for both the wetting and non–wetting fluids [23, 35, 36].

Partially saturated poroelastic dynamics.   For partially saturated porous media, Philippacopoulos [91] studied a "partially" saturated poroelastic half-space problem, where exact analytical expressions have been obtained for the wave propagation due to a point load acting vertically at the surface of a medium that consists of a dry-type layer overlying a fluid-saturated porous substratum. Zienkiewicz et al. [131] extended the formulation of static and dynamic saturated soils to problems of semi-saturated behaviour with the assumption of free air ingress. Berryman [14] derived the equations of poroelasticity for partially saturated materials by using the physically reasonable assumption of negligible capillary pressure change during the passage of an acoustic signal through the media. Smeulders et al. [107] studied the propagation of the compressional waves in a porous medium for a pore liquid containing a small volume fraction of gas. Further, the effect of oscillating gas bubbles was taken into account by introducing a frequency-dependent fluid bulk modulus, which was incorporated in Biot's theory. Thomas [110, 111] established a finite element model for the analysis of wave induced stresses, displacements and pore pressures in an unsaturated seabed. Meissner and Becker [80] identified the significance of capillary effects on the dynamic behaviour of partially saturated sand. It is accomplished through an experimental investigation of the factors affecting the shear modulus ratio. The capillarity has an influence on the degree of saturation of partially saturated sand. An exact stiffness formalism is presented by Degrande et al. [43] to study harmonic and transient wave propagation in multilayered dry, saturated and unsaturated isotropic poroelastic media. Smeulders' extension of Biot's poroelastic theory is used to incorporate unsaturated porous media with a small gas fraction.

A poroelastic model using the theory of mixture with interfaces, which can be used to analyze the propagation conditions and characteristics of acoustical waves in unsaturated

porous media has been published by Muraleetharan and Wei [84] (see also [119, 120]). Yang [130] studied the influence of water saturation on the horizontal and the vertical motion at the interface between porous soil and rock formation due to an incident compressional wave. Velea et al. [114] compared measured and calculated values of elastic compressional and shear wave velocities in partially saturated Ottawa sand. Schrefler and Scotta [104] presented a fully coupled dynamic model for the analysis of water and air flow in deforming porous media under fully or partially saturated conditions. They discussed the drainage problem of a soil column, the air storage problem in an aquifer, and the dynamic analysis of a sand column subjected to a step load. Nie et al. [88] investigated the wave dispersion and attenuation in partially water–saturated sandstones based on the improved Biot–Squirt (BISQ) model, in which the saturation is introduced. Carcione et al. [30] simulated wave propagation in a partially saturated porous medium, where the novel feature is the presence of a second slow wave due to capillary forces. A numerical model capable of modeling the multiphase structure of soils under shock loading is presented by Wang et al. [116]. By using the three–phase model, numerical simulations are carried out to investigate the blast wave propagation in four cases of soils with different water saturation degree ($37.5 - 100\%$). Based on the experimental and the more detailed numerical results, it can be observed that the water saturation has significant influences on the propagation of the wave caused by the blast.

An analytical solution is presented by Lo et al. [73] for the low–frequency behavior of dilatational waves propagating through a homogeneous elastic porous medium containing two immiscible fluids. The theory is based on the Berryman–Thigpen–Chin (BTC) model, in which capillary pressure effects are neglected. Albers [4] investigated the propagation of sound waves in partially saturated soils with a macroscopic linear model, which was based on the two component model of Biot and on the Simple Mixture Model by Wilmanski [126]. In this work, a porous medium consisting of a deformable skeleton and two compressible, chemically non-reacting, pore fluids (liquid and gas) has been modelled.

The analytical solution of wave propagation in saturated porous media has been deduced by Garg et al. [49]. There are also other one dimensional solutions available which can be found in the review article [101]. However, for other than saturated models there are not too many one dimensional solutions available. It may only be mentioned the solution by Vgenopoulou and Beskos [115] based on the double porosity model. Li and Schanz [72] derived an analytical solution for a one dimensional partially saturated poroelastic column. By using the convolution quadrature method the solution in the time domain is obtained. Three different compressional waves, the fast wave, the second slow wave, and the third slow wave, are calculated and validated with the Biot–Gassmann prediction. The wave propagation behaviour in terms of displacement and pore pressure is also examined with the analytical solution. By neglecting the viscous behaviour of the interaction between the fluids and the solid the second and the third slow compressional waves are identified. Ravichandran and Muraleetharan [92] compared the complete and reduced Finite Element

formulations for an unsaturated soil. The permanent deformations were predicted taking elastoplastic effects into account.

Boundary Element Method. In order to establish the boundary integral equations, one crucial condition is the knowledge of corresponding fundamental solutions. Gatmiri and Jabbari [51, 52] published the closed form two and three dimensional quasistatic Green's functions of the governing differential equations for an unsaturated deformable porous medium. The two dimensional and three dimensional thermo–hydro–mechanical fundamental solutions of multiphase porous media in frequency and time domains are presented by Gatmiri et al. [53] and Maghoul et al. [77]. Subsequently, the closed form time domain fundamental solutions are derived by analytical inversion of the Laplace transform solutions. An explicit 3D Laplace transform fundamental solution for partially saturated soils is obtained by Ashayeri et al. [9]. A closed form analytical transient 3D fundamental solution is presented by means of an analytical inverse Laplace transform technique by simplifying the Laplace transform solutions into summation of fractions in terms of Laplace parameter.

In this thesis, the collocation boundary element method is applied which is by far the most frequently used approach due to its versatility and computational efficiency. For the first boundary integral equations, the evaluation of the double layer operator (Cauchy Principal Values) is expected. There are mainly two different types of methods for dealing with this problem either analytical approaches e.g., [57] or numerical approaches e.g., [99]. Of course hybrid approaches are also possible. However, for the analytical method, the disadvantages could be that the formulae are very complicated and sensitive concerning a correct, robust, and stable implementation. The numerical treatment of singular integrals can be subdivided into two different approaches. One approach leaves the singularity untouched and uses special quadrature rules, while the other removes the singularities by special coordinate transformations. The simplest solution is to choose rigid–body displacments of the whole body in the directions of the coordinate axes which is also called rigid–body translation [40, 117, 118]. In the axisymmetric formulation, the rigid–body translation is useful only in the axial direction, since it does not exist in the radial direction. Therefore, other elementary solutions have to be used as the inflation mode [98]. The methods discussed above avoid the direct computation of CPV integrals. Guiggiani and Casalini [58] show that special type of CPV integrals defined even on curved contours and surfaces can always be converted to regular integrals plus simple additional terms. This direct method can be successfully applied to two–dimensional, axisymmetric and three–dimensional boundary element formulations, which shows regular behavior like elasticity, independent of the type and the order of the boundary element employed. The numerical formulation requires only straightforward applications of Gauss–Legendre quadrature formulae.

Regularization approaches of integration by parts is used in this thesis. This technique

was firstly published by Maue [79] for solving Laplace equation in the frequency domain and improved by Nedelec [87] with introducing regularized hypersingular bilinear forms for the Laplace equation, the Helmholtz equation as well as for the system of linear elastostatics. Nishimura and Kobayashi [89] and Becache et al. [13] later presented the regularizations for three dimensional time–harmonic elastodynamics. Based on the work of Kupradze et al. [69], Han [60] presented another regularization of the hypersingular bilinear form for three dimensional elastostatics. Following Han's method, Kielhorn and Schanz [66] and Messner and Schanz [81] applied the regularization approach in viscoelastodynamics and poroelasticity, respectively.

The boundary element formulation for partially saturated poroelasticity is rarely reported at present. In this thesis, with the fundamental solutions in Laplace domain, a corresponding CQM based boundary element time stepping formulation is established.

1.2 Outline

In *chapter 2*, the governing equations for a partially saturated poroelastic continuum are derived based on the average mixture theory. By Laplace transform, the final set of governing equations are obtained.

In *chapter 3*, for a one dimensional partially saturated poroelastic column, the fast and slow compressional wave speeds and attenuations are investigated and compared with Biot–Gassmann's prediction. The one dimensional analytical solutions of the displacement and pore pressures in Laplace domain are presented. The time domain results are obtained by using the Convolution Quadrature Method (CQM). All results are validated by comparing with the saturated results in a limiting process. The slow compressional waves are detected by neglecting the viscosity of the fluids.

In *chapter 4*, by following Hörmander's method, the three dimensional dynamic fundamental solutions for a partially saturated porous continuum are presented. The solutions are validated by comparing with the saturated poroelasticity fundamental solutions in a limiting process.

In *chapter 5*, with the method of weighted residuals, the boundary integral equations are established. The singular behavior of the fundamental solutions in *chapter 4* is investigated. The strong singularity of the double layer operator is regularized with integrating by part. With the spatial and time discretisation, the CQM based time stepping boundary element formulation is established.

In *chapter 6*, the validation of the proposed Collocation Boundary Element Method is done by comparing the three dimensional partially saturated poroelastic column results with the one dimensional analytical solutions of *chapter 3*. A half space problem is also

calculated with the collocation BEM. Finally, a surface vibration isolation by open trenchs is studied.

In *chapter 7*, a short summary of this thesis is given. A discussion of the proposed method and the possible extensions are presented.

In *appendix A*, all the abbreviations for the one dimensional analytical solutions and fundamental solutions are given. The fast compressional wave velocities of the Massilon sandstone are calculated for varying saturation degrees. A short description of the Convolution Quadrature Method is presented. Finally, the full form of the three dimensional fundamental solutions are presented.

2 GOVERNING EQUATIONS FOR PARTIALLY SATURATED POROELASTIC MEDIA

For poroelasticity, three theories of different complexity can be used, i.e., the Theory of Porous Media (e.g., [42, 124]), the Biot theory ([16, 17, 128]), and the Simple Mixture Theory [71, 121, 122, 126]. Under some simplifying assumptions, the Biot theory fits to the Theory of Porous Media, and by neglecting some conditions, the Simple Mixture Theory equals to Biot's theory.

The Theory of Porous Media is based on the assumption of a two component mixture like continuum. The two components include a solid (or called skeleton) part and a pore fluid part. The Biot theory might be the most frequently used in fluid saturated porous materials. Biot used this theory the first time to study the wave propagation in porous media. Compared with the Biot theory, the Simple Mixture Theory is simplified by neglecting the added mass effect reflected in Biot theory, the static coupling effect between partial stresses, and the dependence of the permeability parameter on the frequency [5]. The first simplification removes the non–objectivity of Biot's equations (see [125]). Even though, it has been shown that Biot's theory follows by linearization from a nonlinear thermodynamically objective model, the fact persists that the relative accelerations which are part of the Biot theory are non objective. For the coupling of partial stresses, it is neglected because it is assumed to yield only quantitative corrections without changing the qualitative behavior of the system, at least in the range of a relatively high stiffness of the skeleton in comparison with the fluid [6]. It has been shown within the classical thermodynamic theory of mixtures of fluids by Müller [83] that such coupling are eliminated in macroscopic models by the second law of thermodynamics if one does not account for gradients of partial mass densities. Such a model without coupling terms are named simple mixtures. Considering the third simplification, for low frequencies, there is only a small influence on the waves. However, for high frequencies, the wave speed which has been achieved with the constant parameter will be slightly smaller as well as the attenuation.

As concluded above, for convenience, a linear form of the model for a three component partially saturated poroelastic model is presented on a macroscopic level. It is assumed that each phase of the mixture fills up the entire domain. This is also the level of interest of continuum mechanics, where the continuous distribution of the constituents through a macroscopic control space is assumed. Besides, an isothermal process is considered, i.e., the temperature of the mixture stays constant during any process.

2.1 Model of partially saturated poroelasticity

2.1.1 Basic assumptions

In order to simplify the complex problem, the following assumptions are made for the partially saturated porous media:

1. The partially saturated porous medium is a mixture of the solid phase (solid skeleton), wetting fluid phase (i.e., pore water), and non–wetting phase (i.e., pore air);

2. The state transformation of the three phases is not allowed during the fluids infiltration into the solid skeleton, the evaporation of the wetting fluid, and non–wetting fluid dissolving into the wetting fluid is neglected;

3. All three phases have the same temperature and any temperature change is ignored;

4. All the three phases are compressible.

2.1.2 Averaging process

For a given partially saturated porous continuum, a total volume V_{total} formed by three different components $N^m (m = 1, 2, 3)$ in a given space is assumed. Each point of the total volume V_{total} is considered to be the centroid of a representative elementary volume. The position of the centre of a representative elementary volume in a global coordinate system is described by position vector $\mathbf{x}$.

The density of the mixture is given by

$$\rho(\mathbf{x}, t) = \sum_{m=1}^{3} \bar{\rho}_m(\mathbf{x}, t) \quad , \tag{2.1}$$

where t is the time, $\bar{\rho}_m$ denotes the average bulk density of the $m - th$ component. Corresponding to the average bulk density, ρ_m represents the true density or material density of the $m - th$ component. The volume fraction n_m can now be defined as

$$n_m(\mathbf{x}, t) = \frac{\bar{\rho}_m(\mathbf{x}, t)}{\rho_m(\mathbf{x}, t)} \quad , \tag{2.2}$$

where n_m represents the volume occupied by the $m - th$ component per unit volume of the mixture. $n_m (m = 1, 2, 3)$ can be a rough description for the local structure of the mixture. The situation that $\sum_{m=1}^{3} n_m = 1$, which represents a saturated mixture (no gap among the components), is discussed in the following.

Since the mixture consists of a solid skeleton and two fluids in the pores of the skeleton, the void ratio is defined as

$$n = 1 - n_s = \sum_{f=2}^{3} n_f \quad , \tag{2.3}$$

where n_s denotes the solid volume fraction, and $n_f (f = 2, 3)$ denotes the volume fraction of the corresponding pore fluids.

The saturation degree of the $f - th$ fluid in the mixture is defined as

$$S_f = \frac{n_f}{1 - n_s} \qquad (f = 2, 3) \quad , \tag{2.4}$$

where obviously $\sum_f S_f = 1$ holds.

Remark: The size of the representative elementary volume is important, because the average quantities have to be independent of the size of the average volume, and they should also be continuous in space and time. The representative elementary volume must fulfill the requirements that the average volume element has to be small enough to be considered as infinitesimal, and large enough with respect to the heterogeneity of the material.

2.1.3 Physical models

Porosity. The porosity n is an additional micro structural variable of a macroscopic model in which the components are immiscible. It does not appear in models of miscible mixtures [112]. It measures the void spaces and is given by

$$n = \frac{V_{void}}{V_{total}} = \frac{V_w + V_a}{V_s + V_w + V_a} \quad , \tag{2.5}$$

which is the ratio of the volume of voids V_{void} over the total volume V_{total} as shown in figure 2.1, and it is the same as (2.3).

Take geomechanics as an example, soils and rocks are composed of a mixture of grains of different sizes and of voids which may be filled by, for instance, a mixture of water and air in soil mechanics, or a mixture of oil and water in petroleum engineering. The particles are either loose or compact. The value of the porosity depends mainly on the degree of cementation which is especially influenced by the ratio of very fine particles [56]. In table 2.1, porosity values of some geomaterials are given [12].

The porosity is a micro structural variable of the porous media, and it requires a relation to determine its change. Wilmanski [127] discussed five different methods to describe the changes of porosity:

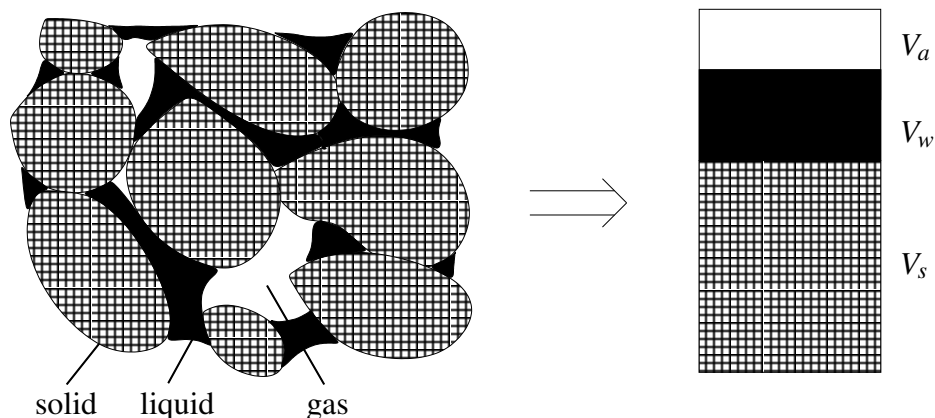   1. By constitutive assumptions;

Figure 2.1: Volume averaging of a partially saturated continuum

2. By an assumption on the incompressibility of true components [25];

3. By an evolution equation for porosity typical for a micro structural variable [24, 26];

4. By a balance equation following from the so called principle of equilibrating pressures [46, 54, 67];

5. By a balance equation of porosity [121, 123].

Table 2.1: Porosity values of some geomaterials [12]

Type	Porosity value	Type	Porosity value
peat soil	$0.60 - 0.80$	fine sand	$0.30 - 0.35$
granular soil	$0.50 - 0.60$	gravel	$0.30 - 0.40$
clay	$0.45 - 0.55$	gravel and sand	$0.30 - 0.35$
silt	$0.40 - 0.50$	sandstone	$0.10 - 0.20$
medium sand	$0.35 - 0.40$	shale	$0.01 - 0.10$
uniform sand	$0.30 - 0.40$	limestone	$0.01 - 0.10$

Saturation degree. For a partially saturated porous continuum, the saturation degrees in (2.4) can also be defined as the ratios of the volume occupied by the fluid V_w or V_a to the void volume, i.e., it holds

$$S_w = \frac{V_w}{V_{void}} \tag{2.6a}$$

$$S_a = \frac{V_a}{V_{void}} \quad . \tag{2.6b}$$

For partially saturated soil, S_w represents the water saturation and S_a represents the air saturation. When the two fluids completely fill out the void, $S_w + S_a = 1$ holds. The water saturation S_w can be used to subdivide soils to different groups,

1. Dry soils: $S_w = 0$, which consist of soil skeleton and air. There is no water in the void;

2. Saturated soils: $S_w = 1.0$, where the void of soils is filled out with water;

3. Partially saturated soils: $0 < S_w < 1$, where the void of soils is filled out with a mixture of water and air.

Surface tension and capillary pressure.   Take also the partially saturated soil as an example, the water–air interface possesses a property named surface tension. This surface tension results from the intermolecular forces acting on molecules in the interface. A molecule in the interior of the water experiences equal forces in all directions, where a molecule within the interface experiences an unbalanced force towards the interior of the water. In order to balance, the surface tension is generated along the interface. The surface tension is tangential to the interface and its magnitude decreases as temperature increases. The surface tension make the interface behave like a membrane. For partially saturated soil, the interface is subjected to the difference between the pore water pressure p^w and pore air pressure p^a which is defined as the capillary pressure.

The concept suction is raised and developed in the early 1900's [28, 38, 48, 94]. It is commonly referred to the free energy state of the water in the soil skeleton [45]. The free energy of the water in the soil can be measured in terms of the partial vapor pressure [96]. The suction is usually referred to the total suction. The total suction consists of two parts as matric suction and osmotic suction [2]. The total suction p^t corresponds to the free energy of the water in the soil, while the capillary suction p^c and osmotic suction p^o are two components of the free energy

$$p^t = p^c + p^o \quad . \tag{2.7}$$

For partially saturated porous media, the capillary pressure p^c can be expressed as a function of the saturation degree, see Brooks and Corey [27], who has introduced a two parameter equation of the form

$$p^c = p^a - p^w = p^d S_e^{-1/\vartheta} \quad . \tag{2.8}$$

The symbol p^d is the non–wetting fluid entry pressure, which is the capillary pressure required to displace the wetting fluid from the largest occurring pore (see [62]). ϑ is the pore size distribution index while the value of ϑ lies between 0.2 and 3, normally. A

small value of ϑ describe single grain size materials while a large one describe highly non uniform materials. S_e denotes the effective wetting fluid saturation degree given by

$$
S_e = \begin{cases} 0 & S_w \leq S_{rw} \\ \dfrac{S_w - S_{rw}}{S_{ra} - S_{rw}} & S_{rw} < S_w < S_{ra} \\ 1 & S_w \geq S_{ra} \end{cases} \quad , \tag{2.9}
$$

where S_{rw} is the residual wetting fluid saturation and S_{ra} is the residual non–wetting fluid saturation. The typical capillary pressure characteristic curve according to Brooks and Corey [27] is plotted in Figure 2.2.
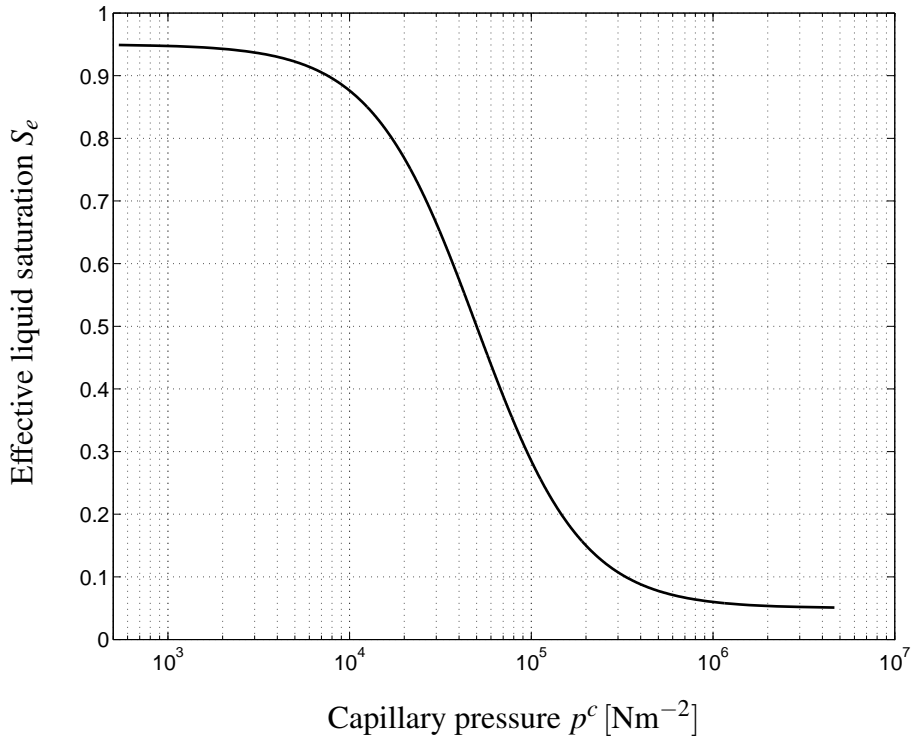
Figure 2.2: Typical curve of effective liquid saturation S_e versus capillary pressure p^c

Stress state variables. The mechanical behavior of the partially saturated porous media can be described in terms of the state of stress. The effective stress is simply a stress state variable which can be used to describe the behavior of a partially saturated porous continuum. The stress analysis for a partially saturated porous continuum is mostly an extension of the saturated poroelastic theory. The principles used in the stress analysis

of a saturated porous continuum are also applicable to the unsaturated case. The concept of effective stress has been well accepted and studied for saturated porous media, while for the more complex unsaturated case, numerous attempts have been made to develop a unified form of effective stress.

For the saturated porous media, Terzaghi [109] firstly introduced the stress state variable controlling the behavior of a saturated soil. The stress state variable for a saturated soil is named the effective stress σ'_{ij} which is expressed as

$$\sigma'_{ij} = \sigma_{ij} - \delta_{ij}p^w \quad , \tag{2.10}$$

where σ_{ij} denotes the total stress, p^w is the pore water pressure, and δ_{ij} is the Kronecker delta. The theory of effective stress is well developed and has been experimentally verified by Bishop and Eldin [22], and Skempton [106], respectively.

The partially saturated porous media is usually modelled as a three phase mixture [70] while, recently, the interface between the fluids has been introduced as a fourth and independent phase [47]. Biot [15] presented a general theory of consolidation for an unsaturated soil with occluded air bubbles. Bishop [19] suggested an expression for effective stress which has been widely used and is given by

$$\sigma'_{ij} = (\sigma_{ij} - \delta_{ij}p^a) + \chi\delta_{ij}(p^a - p^w) \quad , \tag{2.11}$$

where χ is a parameter related to the saturation degree. The value of χ is unity for the saturated case and zero for the dry case. The relationship between χ and the saturation degree can be obtained through the experiments by Bishop [20].

Richards [95] introduced the osmotic suction component into the effective stress equation as

$$\sigma'_{ij} = \sigma_{ij} - \delta_{ij}p^a + \chi_c\delta_{ij}(p^c + p^a) + \chi_o\delta_{ij}(p^o + p^a) \quad , \tag{2.12}$$

where χ_c denotes the effective stress parameter for capillary pressure and χ_o denotes the effective stress parameter for osmotic suction.

Aitchison [3] presented an effective stress equation by slightly modifying that of Richards [95] to

$$\sigma'_{ij} = \sigma_{ij} + \chi_c\delta_{ij}p^c + \chi_o\delta_{ij}p^o \quad . \tag{2.13}$$

By assuming χ(or χ_c) $= S_w$, which has been experimentally verified by Skempton [106] and is applicable for many materials [21], and by neglecting the part of osmotic suction, the total stress σ_{ij} [132] is given by

$$\sigma_{ij} = \sigma'_{ij} - \delta_{ij}\alpha(S_w p^w + S_a p^a) \,, \tag{2.14}$$

where $\alpha = 1 - K/K_s$ describes the compressibility of the solid skeleton with the drained bulk modulus of the mixture K, and K_s is the bulk modulus of the solid skeleton. The

introduction of the factor α is used to describe the compressibility of the solid skeleton, while $\alpha = 1$ fits to the incompressible case as in Terzaghi [109].

Next, for the case of an elastic isotropic skeleton, the constitutive model is given by

$$\sigma'_{ij} = (K - \frac{2}{3}G)\delta_{ij}u_{k,k} + G(u_{i,j} + u_{j,i}) \quad , \tag{2.15}$$

where G denotes the shear modulus. In (2.15) the linearized strain tensor

$$\epsilon_{ij} = \frac{1}{2}(u_{i,j} + u_{j,i}) \tag{2.16}$$

has been introduced.

This constitutive model is used in the following derivation.

2.1.4 Balance equations

For dynamic partially saturated poroelasticity the governing equations are stated following the work of Lewis and Schrefler [71]. To obtain a representation with less as possible unknowns, the solid displacements u_i, the pore wetting fluid pressure p^w, and the pore non–wetting fluid pressure p^a are used.

Balance of mass. The balances of mass for the solid phase and both fluid phases are

$$\frac{\partial[(1-n)\rho_s]}{\partial t} + \operatorname{div}\left[(1-n)\rho_s\frac{\partial u_i}{\partial t}\right] = 0 \tag{2.17a}$$

$$\frac{\partial(nS_w\rho_w)}{\partial t} + \operatorname{div}\left[nS_w\rho_w\frac{\partial(u_i+u_i^w)}{\partial t}\right] = \rho_w I^w \tag{2.17b}$$

$$\frac{\partial(nS_a\rho_a)}{\partial t} + \operatorname{div}\left[nS_a\rho_a\frac{\partial(u_i+u_i^a)}{\partial t}\right] = \rho_a I^a \quad , \tag{2.17c}$$

where ρ_s and $\rho_f(f = w,a)$ denote the density of the solid and the fluids, respectively. The displacements $u_i^f (f = w,a)$ are the relative displacement of the fluids according to the solid. $I^f (f = w,a)$ denotes fluid source terms. The equations (2.17) are formulated under the assumption that the dissolved non–wetting fluid into the wetting fluid can be neglected.

Carrying out the time derivative and neglecting the gradient of the porosity, density and saturation degree, (2.17a) follows to

$$\frac{\partial n}{\partial t} = \frac{1-n}{\rho_s}\frac{\partial \rho_s}{\partial t} + (1-n)\frac{\partial u_{i,i}}{\partial t} \quad . \tag{2.18}$$

Assuming that the solid density is a function of the average pressure p^s and the first stress invariant of the effective stress (see Lewis and Schrefler [71]), for the isothermal case, it holds

$$\frac{1}{\rho_s}\frac{\partial \rho_s}{\partial t} = \frac{1}{1-n}\left[(\alpha - n)\frac{1}{K_s}\frac{\partial p^s}{\partial t} - (1-\alpha)\frac{\partial u_{i,i}}{\partial t}\right] \quad . \tag{2.19}$$

From the entropy inequality given by Hassanizadeh and Gray [61], for the unsaturated flow, the average pressure p^s is given by

$$p^s = S_w p^w + S_a p^a \quad . \tag{2.20}$$

Inserting (2.20) into (2.19) yields

$$\frac{\partial n}{\partial t} - \zeta\left(S_{ww}\frac{\partial p^w}{\partial t} + S_{aa}\frac{\partial p^a}{\partial t}\right) + \zeta K_s\frac{\partial u_{i,i}}{\partial t} = 0 \quad , \tag{2.21}$$

where the abbreviations $\zeta = \dfrac{\alpha - n}{K_s}$, $S_{ww} = S_w + p^c\dfrac{\partial S_w}{\partial p^c}$, and $S_{aa} = S_a - p^c\dfrac{\partial S_w}{\partial p^c}$ are introduced.

Excluding the two extreme cases $S_w = 1$ for the saturated case and $S_w = 0$ for the dry case, the effective saturation degree S_e is given by

$$S_e = \frac{S_w - S_{rw}}{S_{ra} - S_w} \quad . \tag{2.22}$$

Inserting S_e of (2.22) into (2.8), the capillary pressure p^c is given by

$$p^c = p^d\left(\frac{S_w - S_{rw}}{S_{ra} - S_w}\right)^{-\frac{1}{\vartheta}} \quad , \tag{2.23}$$

where the saturation degree S_w can be expressed as

$$S_w = S_{rw} + (S_{ra} - S_{rw})\left(\frac{p^d}{p^c}\right)^{\vartheta} \quad . \tag{2.24}$$

The derivative of the saturation degree S_w with respect to the capillary pressure p^c can be calculated and is given by

$$\begin{aligned}
\frac{\partial S_w}{\partial p^c} &= -\vartheta(S_{ra} - S_{rw})(p^d)^{\vartheta}(p^c)^{-\vartheta-1} \\
&= -\frac{\vartheta(S_{ra} - S_{rw})}{p^d}\left(\frac{S_w - S_{rw}}{S_{ra} - S_w}\right)^{\frac{\vartheta+1}{\vartheta}} \quad .
\end{aligned} \tag{2.25}$$

Combining (2.25) with (2.23) yields

$$p^c \frac{\partial S_w}{\partial p^c} = -\vartheta(S_w - S_{rw}) \quad , \tag{2.26}$$

where the derivative of the saturation degree with respect to the capillary pressure multiplied by the capillary pressure is linearized.

Inserting the equations (2.21) and (2.26) into the mass balance equations of both fluid parts (2.17b) and (2.17c) results in the two continuity equations,

$$\alpha S_w \frac{\partial u_{i,i}}{\partial t} + \left(\zeta S_{ww} S_w + \frac{n}{K_w} S_w - S_u\right) \frac{\partial p^w}{\partial t} + \left(\zeta S_{aa} S_w + S_u\right) \frac{\partial p^a}{\partial t} + n S_w \frac{\partial u_{i,i}^w}{\partial t} = I^w \tag{2.27a}$$

$$\alpha S_a \frac{\partial u_{i,i}}{\partial t} + \left(\zeta S_{ww} S_a + S_u\right) \frac{\partial p^w}{\partial t} + \left(\zeta S_{aa} S_a + \frac{n}{K_a} S_a - S_u\right) \frac{\partial p^a}{\partial t} + n S_a \frac{\partial u_{i,i}^a}{\partial t} = I^a \quad . \tag{2.27b}$$

In (2.27), the gradient of the porosity ∇n, the gradient of the densities $\nabla \rho_s$, $\nabla \rho_f$ ($f = w, a$), and the gradient of the saturation degrees ∇S_w, ∇S_a vanish due to the linearization process. The symbol S_u is given by

$$S_u = -\frac{\vartheta(S_{ra} - S_{rw})}{p^d} \left(\frac{S_w - S_{rw}}{S_{ra} - S_{rw}}\right)^{\frac{\vartheta+1}{\vartheta}} \quad . \tag{2.28}$$

Balance of Momentum.   The momentum balance equation for the mixture is the sum of the equations for each individual constituent. Taking into account the constitutive assumption for the total stress (2.14), the momentum balance equation for the mixture is given by

$$G u_{i,jj} + \left(K + \frac{1}{3}G\right) u_{j,ij} - \alpha(S_w p_{,i}^w + S_a p_{,i}^a) + F_i = \rho \frac{\partial^2 u_i}{\partial t^2} + n S_w \rho_w \frac{\partial^2 u_i^w}{\partial t^2} + n S_a \rho_a \frac{\partial^2 u_i^a}{\partial t^2} \quad , \tag{2.29}$$

where F_i denotes the bulk body force. The bulk density ρ is the averaged density of the mixture and is denoted by

$$\rho = (1 - n)\rho_s + n S_w \rho_w + n S_a \rho_a \quad . \tag{2.30}$$

The momentum balance equations for each fluid phase yield the generalized form of Darcy's law, where the dissipative terms are taken into consideration. The momentum balance equations for each fluid phase are given by

$$n S_w \frac{\partial u_i^w}{\partial t} = -\kappa_w \left(p_{,i}^w + \rho_w \frac{\partial^2 u_i}{\partial t^2} + \rho_w \frac{\partial^2 u_i^w}{\partial t^2}\right) \tag{2.31a}$$

$$nS_a \frac{\partial u_i^a}{\partial t} = -\kappa_a \left(p_{,i}^a + \rho_a \frac{\partial^2 u_i}{\partial t^2} + \rho_a \frac{\partial^2 u_i^a}{\partial t^2} \right) \quad , \tag{2.31b}$$

where the phase permeability of the wetting fluid ($f = w$) and the non–wetting fluid ($f = a$) is given by

$$\kappa_f = \frac{K_{rf}k}{\eta_f} \quad (f = w, a) \quad . \tag{2.32}$$

K_{rf} denotes the relative fluid phase permeability, k denotes the intrinsic fluid permeability of a porous continuum, and η_f is the viscosity of the fluid.

The relative phase permeability K_{rf} is a dimensionless measure of the effective permeability of the $f - th$ phase. It is the ratio of the effective permeability of $f - th$ phase to the absolute permeability. Based on experiments, the relative permeability can be constructed as a function of the saturation degree. According to the literature, the relative permeability K_{rf} can be evaluated either following the method of Brooks and Corey [27] or van Genuchten [113].

In the following work, the equations of the relative permeability by Brooks and Corey are used, and are given by

$$K_{rw} = S_e^{(2+3\vartheta)/\vartheta} \tag{2.33}$$

$$K_{ra} = (1 - S_e)^2 \left[1 - S_e^{(2+\vartheta)/\vartheta} \right] \quad . \tag{2.34}$$

These empirical equations are based on the experiment of a water–gas mixture. For other mixtures such as a mixture of water–oil or oil–gas, the corresponding empirical equations are needed.

The curves of the relative permeability K_{rf} ($f = w, a$) versus effective saturation degree S_e according to Brooks and Corey's equations are plotted in figure 2.3.

2.2 Governing equations in the Laplace domain

Equations (2.27), (2.29), (2.31a) and (2.31b) are sufficient to solve the problem of partially saturated poroelasticity. Counting the unknown field variables, there could be two sets of unknown variables used for partially saturated poroelasticity. The combination of the solid displacement u_i and the relative displacement of the fluids u_i^f ($f = w, a$), and the combination of the solid displacement u_i and the fluids pore pressure p^f ($f = w, a$) may be selected. Normally, the pore pressure is of much more interests compared with the relative displacement of the fluid, and it would be natural to describe the fluids by the pressure. For the first combination, it is difficult to determine the boundary condition of the relative displacement of the fluids. Besides, in order to reduce the number of the
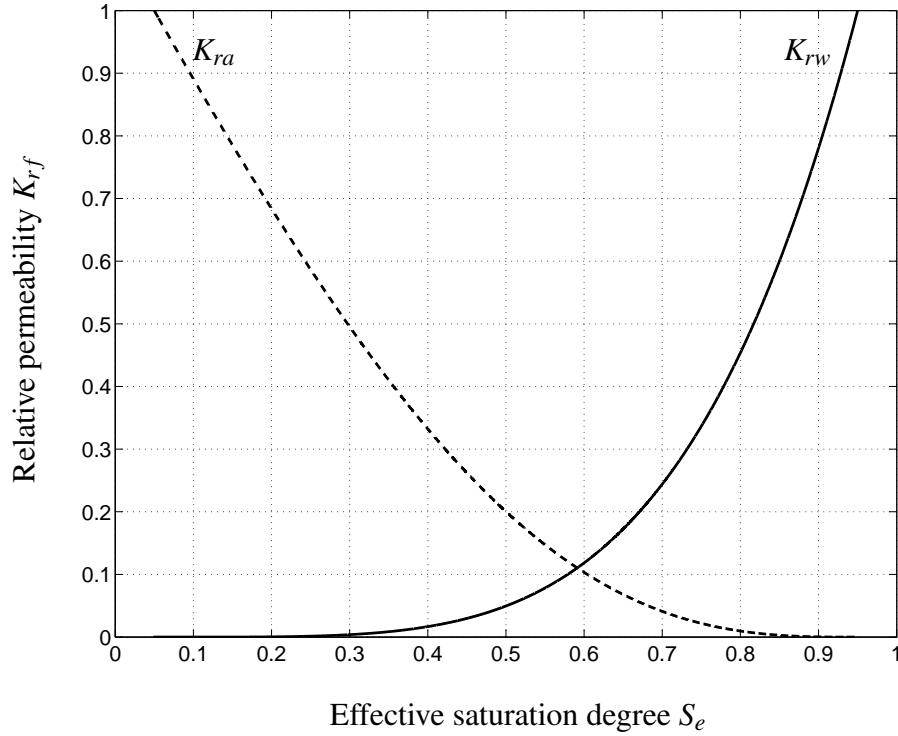
Figure 2.3: Relative permeability K_{rf} versus effective saturation degree S_e according to Brooks and Corey

unknown variables, the combination of the solid displacement and the pore pressure are chosen to be the unknown variables.

In time domain, however, the elimination of the relative displacement is not possible, because it appears in (2.27) and (2.29) in different orders of time derivatives. Hence, the Laplace transformation is introduced to eliminate the time derivatives. In the following, all the equations are transformed to the Laplace domain.

The Laplace transformation in (2.35) is a linear operator of a function $f(t)$ with a real argument t ($t \geq 0$) that transforms it to a function $\hat{f}(s)$ with a complex argument s. The definition of the Laplace transformation can be expressed as

$$\hat{f}(s) = \mathcal{L}\{f(t)\} = \int\limits_{0}^{\infty} e^{-st} f(t) dt \quad , \tag{2.35}$$

where the symbol $\hat{(\,)}$ represents the variables in the Laplace domain, and $\mathcal{L}$ denotes the Laplace transform operator.

Applying the Laplace transformation to (2.31a) and (2.31b), the momentum balance equations of the fluids are given by

$$nS_w\hat{u}_i^w s = -\kappa_w \left(\hat{p}_{,i}^w + \rho_w \hat{u}_i s^2 + \rho_w \hat{u}_i^w s^2 \right) \tag{2.36a}$$

$$nS_a\hat{u}_i^a s = -\kappa_a \left(\hat{p}_{,i}^a + \rho_a \hat{u}_i s^2 + \rho_a \hat{u}_i^a s^2 \right) \quad . \tag{2.36b}$$

In the following, for both equations in (2.36), the relative displacement of the fluids in the Laplace domain $\hat{u}_i^w$ and $\hat{u}_i^a$ can be extracted and are given by

$$\hat{q}_i^w = s\hat{u}_i^w = -\beta \frac{1}{n\rho_w s} \left(\hat{p}_{,i}^w + \rho_w s^2 \hat{u}_i \right) \tag{2.37a}$$

$$\hat{q}_i^a = s\hat{u}_i^a = -\gamma \frac{1}{n\rho_a s} \left(\hat{p}_{,i}^a + \rho_a s^2 \hat{u}_i \right) \quad , \tag{2.37b}$$

where $\hat{q}_i^f$ $(f = w, a)$ denotes the wetting fluid / non–wetting fluid flux, respectively. The symbols β and γ are Laplace parameter dependent variables and expressed as

$$\beta = \frac{\kappa_w n\rho_w s}{nS_w + \kappa_w \rho_w s} \tag{2.38a}$$

$$\gamma = \frac{\kappa_a n\rho_a s}{nS_a + \kappa_a \rho_a s} \quad . \tag{2.38b}$$

Substituting the relative displacements (2.37) in (2.27) and (2.29), the governing equations of partially saturated poroelasticity in the Laplace domain are obtained and given by

$$G\hat{u}_{i,jj} + (K + \frac{G}{3})\hat{u}_{j,ij} - (\rho - \beta S_w\rho_w - \gamma S_a\rho_a)s^2\hat{u}_i - (\alpha - \beta)S_w\hat{p}_{,i}^w - (\alpha - \gamma)S_a\hat{p}_{,i}^a = -\hat{F}_i \tag{2.39a}$$

$$-(\alpha - \beta)S_w s\hat{u}_{i,i} - (\zeta S_{ww}S_w + \frac{n}{K_w}S_w - S_u)s\hat{p}^w + \frac{\beta S_w}{\rho_w s}\hat{p}_{,ii}^w - (\zeta S_{aa}S_w + S_u)s\hat{p}^a = -\hat{I}^w \tag{2.39b}$$

$$-(\alpha - \gamma)S_a s\hat{u}_{i,i} - (\zeta S_{ww}S_a + S_u)s\hat{p}^w - (\zeta S_{aa}S_a + \frac{n}{K_a}S_a - S_u)s\hat{p}^a + \frac{\gamma S_a}{\rho_a s}\hat{p}_{,ii}^a = -\hat{I}^a \quad , \tag{2.39c}$$

with the unknown variables solid displacement $\hat{u}_i$, wetting fluid pore pressure $\hat{p}^w$, and non–wetting fluid pore pressure $\hat{p}^a$ in the Laplace domain.

For convenience, the coupled differential equations (2.39) are written in a more compact form as

$$\mathcal{B} \begin{bmatrix} \hat{u}_i \\ \hat{p}^w \\ \hat{p}^a \end{bmatrix} = \begin{bmatrix} -\hat{F}_i \\ -\hat{I}^w \\ -\hat{I}^a \end{bmatrix} \tag{2.40}$$

with

$$\mathcal{B} = \begin{bmatrix} A_1\delta_{ij} + A_2\partial_i\partial_j & A_3\partial_i & A_4\partial_i \\ A_5\partial_j & A_6 & A_7 \\ A_8\partial j & A_9 & A_{10} \end{bmatrix} \quad ,$$

$$A_1 = G\nabla^2 - (\rho - \beta S_w \rho_w - \gamma S_a \rho_a)s^2 \quad ,$$

$$A_2 = K + \frac{G}{3} \quad ,$$

$$A_3 = -(\alpha - \beta)S_w \quad ,$$

$$A_4 = -(\alpha - \gamma)S_a \quad ,$$

$$A_5 = -(\alpha - \beta)S_w s \quad ,$$

$$A_6 = -(\zeta S_{ww}S_w + \frac{n}{K_w}S_w - S_u)s + \frac{\beta S_w}{\rho_w s}\nabla^2 \quad ,$$

$$A_7 = -(\zeta S_{aa}S_w + S_u)s \quad ,$$

$$A_8 = -(\alpha - \gamma)S_a s \quad ,$$

$$A_9 = -(\zeta S_{ww}S_a + S_u)s \quad ,$$

$$A_{10} = -(\zeta S_{aa}S_a + \frac{n}{K_a}S_a - S_u)s + \frac{\gamma S_a}{\rho_a s}\nabla^2 \quad .$$

Remark 1.   A constant spatial distribution of the saturation degree is explicitly assumed in the above derived governing equations. Based on this the gradient of the saturation degree has been neglected. However, it should be remarked that this holds only for the initial saturation degree. This initial saturation degree could be equal to or within the range of the irreducible saturation degree (S_{rw}, S_{ra}), which is a minimum saturation degree in a porous medium. The irreducible saturation degree may vary depending on different kind of porous media according to the corresponding pore size. Therefore, the application of the proposed model is constrained and limited, i.e., for unsaturated soil (normally with large pore size), the value of the irreducible saturation degree is small; for unsaturated rock (normally with small pore size), the value of the irreducible water saturation is large.

Remark 2.   Due to the assumption that the extreme cases $S_w = 1$ and $S_w = 0$ are excluded (see (2.22)) in the linearization process (the derivative of the saturation degree S_w with respect to the capillary pressure p^c), the presented governing equations can only describe the properties of partially saturated poroelasticity when $0 < S_w < 1$.

For the extreme case $S_w = 0$, the equations turn out to be simple an elasticity problem. For the extreme case $S_w = 1$, the equation (2.39c) vanishes. Besides, since there is no

non–wetting fluid phase, the corresponding parameters such as the non–wetting fluid entry pressure p^d and the capillary pressure p^c vanish, and the derivative of the saturation degree S_w with respect to the capillary pressure p^c does not exist anymore. The symbols S_{ww} and S_{aa} equal to 1 and 0, respectively. Finally, the governing equations of saturated poroelasticity can be concluded as

$$G\hat{u}_{i,jj} + (K + \frac{G}{3})\hat{u}_{j,ij} - (\rho - \beta\rho_w)s^2\hat{u}_i - (\alpha - \beta)\hat{p}^w_{,i} = -\hat{F}_i \tag{2.41a}$$

$$-(\alpha - \beta)s\hat{u}_{i,i} - (\zeta + \frac{n}{K_w})s\hat{p}^w + \frac{\beta}{\rho_w s}\hat{p}^w_{,ii} = -\hat{I}^w \quad . \tag{2.41b}$$

The governing equations of saturated poroelasticity from Biot's theory [100] can be obtained by substituting the entry $(\zeta + \frac{n}{K_w})$ with $\frac{n^2}{R}$, where R in Biot's theory is a parameter used to describe the coupling between the solid the the fluid.

3 WAVE PROPAGATION IN A ONE DIMENSIONAL COLUMN

The dynamic three phase model for partially saturated poroelasticity is applied to a one dimensional column in this chapter, and an analytical solution in the Laplace domain is deduced. The purpose of the proposed one dimensional analytical solution is to study the wave properties in partially saturated porous media, to verify the presented model, and to validate the three dimensional numerical results in the following chapter.

By applying the convolution quadrature method the solution in the time domain is obtained. Using the material data of Massillon sandstone the three different compressional waves, the fast wave, the second slow wave, and the third slow wave, are calculated, and the fast compressional wave is verified with the Biot–Gassmann prediction. The wave propagation behavior in terms of displacement and pore pressure is also examined with the analytical solution. By neglecting the viscous behavior of the interaction between the fluids and the solid the second and the third slow compressional waves are identified.

3.1 Analytical solutions of a one dimensional partially saturated poroelastic column

To study the influence of partially saturated poroelastic parameters on wave propagation, a one dimensional column of length ℓ is considered (see figure 3.1).
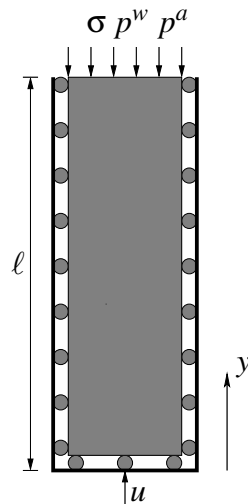
Figure 3.1: A one dimensional column under dynamic loads

It is assumed that on the side walls, the vertical displacements are zero, besides, the side walls are frictionless and impermeable. At the top of the column, a stress $\sigma = -S_0 H(t)$, a water pressure $p^w = P^w H(t)$, and an air pressure $p^a = P^a H(t)$ are prescribed. Therein, $H(t)$ denotes the unit step function in time, i.e., the load is applied at $t > 0$. The bottom of the column is assumed to be impermeable, and it might move with a constant displacement $u = U_0 H(t)$.

This one dimensional example can also be seen as an approximation of a partially saturated poroelastic halfspace with an infinite layer depth ($\ell \to \infty$). Due to all the prescribed restrictions, only the displacement u in y–direction, the pore water pressure p^w, and the pore air pressure p^a remain as the degrees of freedom.

For the above assumptions of vanishing body force F_i and source terms I^f ($f = w, a$), the governing equations in the Laplace domain given in (2.39) are reduced to three scalar coupled ordinary differential equations

$$(K + \frac{4}{3}G)\hat{u}_{,yy} - s^2(\rho - \beta S_w \rho_w - \gamma S_a \rho_a)\hat{u} - (\alpha - \beta)S_w \hat{p}^w_{,y} - (\alpha - \gamma)S_a \hat{p}^a_{,y} = 0 \quad \text{(3.1a)}$$

$$(\alpha - \beta)S_w s\hat{u}_{,y} + (\zeta S_{ww}S_w + \frac{n}{K_w}S_w - Su)s\hat{p}^w - \frac{\beta S_w}{\rho_w s}\hat{p}^w_{,yy} + (\zeta S_{aa}S_w + S_u)s\hat{p}^a = 0 \quad \text{(3.1b)}$$

$$(\alpha - \gamma)S_a s\hat{u}_{,y} + (\zeta S_{ww}S_a + S_u)s\hat{p}^w + (\zeta S_{aa}S_a + \frac{n}{K_a}S_a - S_u)s\hat{p}^a - \frac{\gamma S_a}{\rho_a s}\hat{p}^a_{,yy} = 0 \quad . \tag{3.1c}$$

According to the prescribed assumptions, the boundary conditions at the bottom and the top of the column in the Laplace domain are given by

$$\begin{aligned}
\hat{u}(y = 0) = U_0 \qquad & \hat{\sigma}(y = \ell) = -S_0 \\
\hat{p}^w(y = \ell) = P^w \qquad & \hat{q}^w(y = 0) = 0 \\
\hat{p}^a(y = \ell) = P^a \qquad & \hat{q}^a(y = 0) = 0 \quad .
\end{aligned}$$

This turns out to be a system of homogeneous ordinary differential equations with inhomogeneous boundary conditions. Such a system can be solved by using the exponential ansatz

$$\hat{u}(y) = U e^{\lambda s y} \tag{3.2a}$$

$$\hat{p}^w(y) = U^w e^{\lambda s y} \tag{3.2b}$$

$$\hat{p}^a(y) = U^a e^{\lambda s y} \quad . \tag{3.2c}$$

Inserting the ansatz into the equations (3.1), it follows

$$\begin{bmatrix} (B_1\lambda^2 - B_2)s & -B_3\lambda & -B_4\lambda \\ B_3\lambda s & (B_5 - B_6\lambda^2) & B_7 \\ B_4\lambda s & B_8 & (B_9 - B_{10}\lambda^2) \end{bmatrix} \begin{bmatrix} U \\ U^w \\ U^a \end{bmatrix} = 0 \quad , \tag{3.3}$$

which results in an eigenvalue problem for λ.

The characteristic equation for this eigenvalue problem is given by

$$C_1\lambda^6 + C_2\lambda^4 + C_3\lambda^2 + C_4 = 0 \quad . \tag{3.4}$$

For equation (3.4), there are six complex roots which correspond to the three different compressional waves (the fast compressional wave, the second slow compressional wave, and the third slow compressional wave) in this one dimensional partially saturated poroelastic column. These six complex roots are

$$\lambda_1 = -\lambda_4 = \sqrt{N_1 + \frac{N_2 C_2^2}{3C_1} - N_2 C_3 + \frac{1}{3N_2 C_1}} \tag{3.5a}$$

$$\lambda_2 = -\lambda_5 = \sqrt{N_1 + \frac{3C_1 C_3 - C_2^2}{6C_1} N_2(1 - i\sqrt{3}) - \frac{1}{6N_2 C_1}(1 + i\sqrt{3})} \tag{3.5b}$$

$$\lambda_3 = -\lambda_6 = \sqrt{N_1 + \frac{3C_1 C_3 - C_2^2}{6C_1} N_2(1 + i\sqrt{3}) - \frac{1}{6N_2 C_1}(1 - i\sqrt{3})} \quad . \tag{3.5c}$$

For this one dimensional case, the shear wave does not exist. However, the shear wave will be calculated in chapter 4.

All the symbols B_i, C_i, and N_i given in equations (3.3), (3.4), and (3.5) can be found in appendix A.1.1.

Corresponding to the six complex roots, the six solutions for the ansatz in (3.2) can be super–imposed as given in the following

$$\hat{u}(y) = \sum_{i=1}^{6} U_i e^{\lambda_i sy} \tag{3.6a}$$

$$\hat{p}^w(y) = \sum_{i=1}^{6} U_i^w e^{\lambda_i sy} \tag{3.6b}$$

$$\hat{p}^a(y) = \sum_{i=1}^{6} U_i^a e^{\lambda_i sy} \quad , \tag{3.6c}$$

which leads to the complete solutions for the homogeneous problem

According to (3.3), the relationships between U_i and U_i^w, U_i and U_i^a can be expressed as

$$U_i^w = \frac{(B_1 B_7 + B_3 B_4 S_a)\lambda_i^2 - B_2 B_7}{(B_4 B_6 S_a \lambda_i^2 + B_3 B_7 S_w - B_4 B_5 S_a)\lambda_i} sU_i = a_i sU_i \tag{3.7a}$$

$$U_i^a = \frac{(B_1 B_8 + B_3 B_4 S_w)\lambda_i^2 - B_2 B_8}{(B_3 B_{10} S_w \lambda_i^2 + B_4 B_8 S_a - B_3 B_9 S_w)\lambda_i} s U_i = b_i s U_i \ . \tag{3.7b}$$

Substituting U_i^w and U_i^a with U_i in equation (3.6), the solutions are

$$\hat{u}(y) = \sum_{i=1}^{6} U_i e^{\lambda_i s y} \tag{3.8a}$$

$$\hat{p}^w(y) = \sum_{i=1}^{6} a_i s U_i e^{\lambda_i s y} \tag{3.8b}$$

$$\hat{p}^a(y) = \sum_{i=1}^{6} b_i s U_i e^{\lambda_i s y} \quad . \tag{3.8c}$$

The stress boundary condition at the top of the column $(y = \ell)$

$$(K + \frac{4}{3}G)s \sum_{i=1}^{6} (\lambda_i e^{\lambda_i s \ell} U_i) = \alpha(S_w P^w + S_a P^a) - S_0 \tag{3.9}$$

are obtained by inserting the ansatz functions (3.2) and the relations (3.7) in the definition of the total stress (2.14).

The pressure boundary conditions at the top of the column are given by

$$s \sum_{i=1}^{6} (a_i e^{\lambda_i s \ell} U_i) = P^w \tag{3.10a}$$

$$s \sum_{i=1}^{6} (b_i e^{\lambda_i s \ell} U_i) = P^a \quad . \tag{3.10b}$$

At the bottom of the column $(y = 0)$, the flux and the displacement boundary conditions are prescribed and given by

$$\sum_{i=1}^{6} (a_i \lambda_i U_i) = -\rho_w U_0 \tag{3.11a}$$

$$\sum_{i=1}^{6} (b_i \lambda_i U_i) = -\rho_a U_0 \tag{3.11b}$$

$$\sum_{i=0}^{6} U_i = U_0 \quad . \tag{3.11c}$$

After determining the six constants U_i with the six boundary conditions (3.9) – (3.11), the analytical solutions of the partially saturated poroelastic column in the Laplace domain can be obtained. The solutions can be divided into four different load cases based on the superposition principle. The explicit analytical solutions are given in the following.

Solutions with the stress boundary condition ($\hat{u}|_{y=0} = 0$, $\hat{\sigma}|_{y=\ell} = -S_0$, $\hat{p}^w|_{y=\ell} = 0$, $\hat{p}^a|_{y=\ell} = 0$**).** The analytical solutions are given by

$$\hat{u} = \frac{S_0 s^{-1}}{M(K + \frac{4}{3}G)} \sum_{i=1}^{3} \left[\frac{e^{-\lambda_i s(y+\ell)} - e^{\lambda_i s(y-\ell)}}{1 + e^{-2\lambda_i s\ell}} t_i \right] \tag{3.12a}$$

$$\hat{p}^w = \frac{S_0}{M(K + \frac{4}{3}G)} \sum_{i=1}^{3} \left[\frac{e^{-\lambda_i s(y+\ell)} + e^{\lambda_i s(y-\ell)}}{1 + e^{-2\lambda_i s\ell}} t_i a_i \right] \tag{3.12b}$$

$$\hat{p}^a = \frac{S_0}{M(K + \frac{4}{3}G)} \sum_{i=1}^{3} \left[\frac{e^{-\lambda_i s(y+\ell)} + e^{\lambda_i s(y-\ell)}}{1 + e^{-2\lambda_i s\ell}} t_i b_i \right] \quad , \tag{3.12c}$$

where

$$t_1 = a_2 b_3 - a_3 b_2 \quad ,$$
$$t_2 = a_3 b_1 - a_1 b_3 \quad ,$$
$$t_3 = a_1 b_2 - a_2 b_1 \quad ,$$
$$M = t_1 \lambda_1 + t_2 \lambda_2 + t_3 \lambda_3 \quad .$$

Solutions with the pore water pressure boundary condition ($\hat{u}|_{y=0} = 0$, $\hat{\sigma}|_{y=\ell} = 0$, $\hat{p}^w|_{y=\ell} = P^w$, $\hat{p}^a|_{y=\ell} = 0$**).** The analytical solutions are given by

$$\hat{u} = \frac{P^w}{Ms} \sum_{i=1}^{3} \left[\left(\frac{\alpha S_w}{K + 4/3G} t_i + p_i \right) \frac{e^{\lambda_i s(y-\ell)} - e^{-\lambda_i s(y+\ell)}}{1 + e^{-2\lambda_i s\ell}} \right] \tag{3.13a}$$

$$\hat{p}^w = \frac{P^w}{M} \sum_{i=1}^{3} \left[a_i \left(\frac{\alpha S_w}{K + 4/3G} t_i + p_i \right) \frac{e^{\lambda_i s(y-\ell)} + e^{-\lambda_i s(y+\ell)}}{1 + e^{-2\lambda_i s\ell}} \right] \tag{3.13b}$$

$$\hat{p}^a = \frac{P^w}{M} \sum_{i=1}^{3} \left[b_i \left(\frac{\alpha S_w}{K + 4/3G} t_i + p_i \right) \frac{e^{\lambda_i s(y-\ell)} + e^{-\lambda_i s(y+\ell)}}{1 + e^{-2\lambda_i s\ell}} \right] \quad , \tag{3.13c}$$

where

$$p_1 = b_2 \lambda_3 - b_3 \lambda_2 \quad ,$$
$$p_2 = b_1 \lambda_3 - b_3 \lambda_1 \quad ,$$
$$p_3 = b_2 \lambda_1 - b_1 \lambda_2 \quad .$$

Solutions with the pore air pressure boundary condition ($\hat{u}|_{y=0} = 0$, $\hat{\sigma}|_{y=\ell} = 0$, $\hat{p}^w|_{y=\ell} = 0$, $\hat{p}^a|_{y=\ell} = P^a$**).** The analytical solutions are given by

$$\hat{u} = \frac{P_0^a}{Ms} \sum_{i=1}^{3} \left[\left(\frac{\alpha S_a}{K + 4/3G} t_i + q_i \right) \frac{e^{\lambda_i s(y-\ell)} - e^{-\lambda_i s(y+\ell)}}{1 + e^{-2\lambda_i s\ell}} \right] \tag{3.14a}$$

$$\hat{p}^w = \frac{P_0^a}{M} \sum_{i=1}^{3} \left[a_i \left(\frac{\alpha S_a}{K + 4/3G} t_i + q_i \right) \frac{e^{\lambda_i s(y-\ell)} + e^{-\lambda_i s(y+\ell)}}{1 + e^{-2\lambda_i s\ell}} \right] \tag{3.14b}$$

$$\hat{p}^a = \frac{P_0^a}{M} \sum_{i=1}^{3} \left[b_i \left(\frac{\alpha S_a}{K + 4/3G} t_i + q_i \right) \frac{e^{\lambda_i s(y-\ell)} + e^{-\lambda_i s(y+\ell)}}{1 + e^{-2\lambda_i s\ell}} \right] \quad, \tag{3.14c}$$

where

$$q_1 = a_3\lambda_2 - a_2\lambda_3 \quad,$$

$$q_2 = a_3\lambda_1 - a_1\lambda_3 \quad,$$

$$q_3 = a_1\lambda_2 - a_2\lambda_1 \quad.$$

Solutions with the displacement boundary condition ($\hat{u}|_{y=0} = U_0$, $\hat{\sigma}|_{y=\ell} = 0$, $\hat{p}^w|_{y=\ell} = 0$, $\hat{p}^a|_{y=\ell} = 0$). The analytical solutions are given by

$$\hat{u} = \frac{U_0}{N} \sum_{i=1}^{3} \left[(e_i\rho_w + f_i\rho_a + g_i t_i) \frac{e^{\lambda_i s(y-2\ell)} + e^{-\lambda_i sy}}{1 + e^{-2\lambda_i s\ell}} \right] \tag{3.15a}$$

$$\hat{p}^w = \frac{U_0}{N} \sum_{i=1}^{3} \left[(e_i\rho_w + f_i\rho_a + g_i t_i) a_i s \frac{e^{\lambda_i s(y-2\ell)} - e^{-\lambda_i sy}}{1 + e^{-2\lambda_i s\ell}} \right] \tag{3.15b}$$

$$\hat{p}^a = \frac{U_0}{N} \sum_{i=1}^{3} \left[(e_i\rho_w + f_i\rho_a + g_i t_i) b_i s \frac{e^{\lambda_i s(y-2\ell)} - e^{-\lambda_i sy}}{1 + e^{-2\lambda_i s\ell}} \right] \quad, \tag{3.15c}$$

where

$$e_1 = b_3\lambda_3 - b_2\lambda_2 \quad,$$

$$e_2 = b_1\lambda_1 - b_3\lambda_3 \quad,$$

$$e_3 = b_2\lambda_2 - b_1\lambda_1 \quad,$$

$$f_1 = a_2\lambda_2 - a_3\lambda_3 \quad,$$

$$f_2 = a_3\lambda_3 - a_a\lambda_1 \quad,$$

$$f_3 = a_1\lambda_1 - a_2\lambda_2 \quad,$$

$$g_1 = \lambda_2\lambda_3 \quad,$$

$$g_2 = \lambda_1\lambda_3 \quad,$$

$$g_3 = \lambda_1\lambda_2 \quad,$$

$$N = \lambda_2\lambda_3 t_1 + \lambda_1\lambda_3 t_2 + \lambda_1\lambda_2 t_3 \quad.$$

The corresponding stress and flux can be calculated following the definitions in (2.14) and (2.37).

For the obtained one dimensional analytical solutions, by applying the Convolution Quadrature Method (CQM) (see appendix A.3), the time domain solution $u(n\Delta t)$

$$u(n\Delta t) = \sum_{k=0}^{n} \omega_{n-k}(\hat{u}, \Delta t)\sigma(k\Delta t) \quad , \quad n = 0, 1, ..., N , \qquad (3.16)$$

with the weighting function $\omega_{n-k}(\Delta t)$ determined by

$$\omega_{n-k}(\hat{u}, \Delta t) = \frac{\mathcal{R} \, e^{-(n-k)}}{L} \sum_{\ell=0}^{L-1} \hat{u}\left(\frac{\gamma(\mathcal{R} \, e^{i\ell\frac{2\pi}{L}})}{\Delta t}\right) e^{-i(n-k)\ell\frac{2\pi}{L}} . \qquad (3.17)$$

In the following calculations, a BDF 2 as underlying multistep method $\gamma(z) = 1.5 - 2z + 0.5z^2$ and $\mathcal{R}^N = 10^{-5}$ are used.

3.2 Wave propagation in a one dimensional partially saturated poroelastic column

Wave propagation in a one dimensional partially saturated poroelastic column is studied in the following using the developed analytical solution. To be confident of the solution, verifications of the phase velocities with experiments [85, 86] and validations of the displacement and the pore pressure solutions with analytical solutions of special cases [50, 102] are performed. The material data of Massilon sandstone measured by Murphy [86] are used in the calculations. Hence, the fluids are water and air. These data are given in table 3.1. The pore size distribution index ϑ is set to 1.5, the residual water saturation S_{rw} is set to 0, and the air entry saturation S_{ra} is set to 1. The two latter values may somehow vary for different materials but enable to evaluate the solutions in the extreme case when $S_w = S_e$. This is done only for comparison reasons.

First, the wave velocities are calculated and studied. Based on the governing equations, there are three compressional waves: the fast wave p_1, the second slow wave p_2, and the third slow wave p_3. The shear wave is also included in section 2.2 but does not exist in the one dimensional case.

The wave speed and the attenuation are calculated from the complex roots λ_i of equation (3.4). Taking the Laplace parameter $s = i\omega$, i.e., the real part is set to zero, the inverse of the real part of λ_i represents the phase velocities v_{pi}, and the imaginary part of λ_i multiplied by the frequency ω represents the attenuation a_{pi} (see [4]),

$$v_{pi} = \frac{1}{\Re(\lambda_i)} \qquad (3.18a)$$

$$a_{pi} = \omega\Im(\lambda_i) \quad . \qquad (3.18b)$$

Table 3.1: Parameters of Massilon sandstone

Parameter type	Symbol	Value	Unit
Porosity	n	0.23	-
Density of the solid skeleton	ρ_s	2650	$\mathrm{kg/m^3}$
Density of the water	ρ_w	997	$\mathrm{kg/m^3}$
Density of the air	ρ_a	1.10	$\mathrm{kg/m^3}$
Drained bulk modulus of the mixture	K	1.02×10^9	$\mathrm{N/m^2}$
Shear modulus of the mixture	G	1.44×10^9	$\mathrm{N/m^2}$
Bulk modulus of the solid skeleton	K_s	3.5×10^{10}	$\mathrm{N/m^2}$
Bulk modulus of the water	K_w	2.25×10^9	$\mathrm{N/m^2}$
Bulk modulus of the air	K_a	1.10×10^5	$\mathrm{N/m^2}$
Intrinsic permeability	k	2.5×10^{-12}	$\mathrm{m^2}$
Viscosity of the water	η_w	1.0×10^{-3}	$\mathrm{Ns/m^2}$
Viscosity of the air	η_a	1.8×10^{-5}	$\mathrm{Ns/m^2}$
Gas entry pressure	p^d	5×10^4	$\mathrm{N/m^2}$

The velocities and attenuation of the fast and slow compressional waves are plotted versus the saturation degree in figure 3.2 – 3.4. Varying the frequency ω, the fast compressional wave speed v_{p1} is compared to the compressional wave speed v_p^G calculated from Gassmann's equation [50] which is given by

$$K^* = K + \frac{\alpha^2}{\dfrac{\alpha - n}{K_s} + n\left(\dfrac{S_w}{K_w} + \dfrac{S_a}{K_a}\right)} \tag{3.19a}$$

$$v_p^G = \sqrt{\frac{K^* + \dfrac{4}{3}G}{\rho}} \quad, \tag{3.19b}$$

where K^* is the effective bulk modulus of the undrained fluid mixture of a saturated porous medium. Murphy [86] tested the Massillon sandstone and verified Gassmann's prediction. Hence, the square dots in figure 3.2 representing the results from the Gassmann's equations have been verified by the experiment. For later use, a list of the fast compressional wave velocity of the Massilon sandstone calculated by the Gassmann's equations with varying the water saturation S_w can be found in appendix A.2.

The known effect that the fast wave velocity v_{p1} decreases with increasing the water saturation is visible in figure 3.2(a), as well as the drastic increase for the nearly saturated case. This result matches Gassmann's predictions. According to them, with increasing the water saturation the averaged mixture density ρ increases and this slows down v_{p1}. The effective bulk modulus K^* also increases and this speeds up v_{p1}. However, for the air phase,
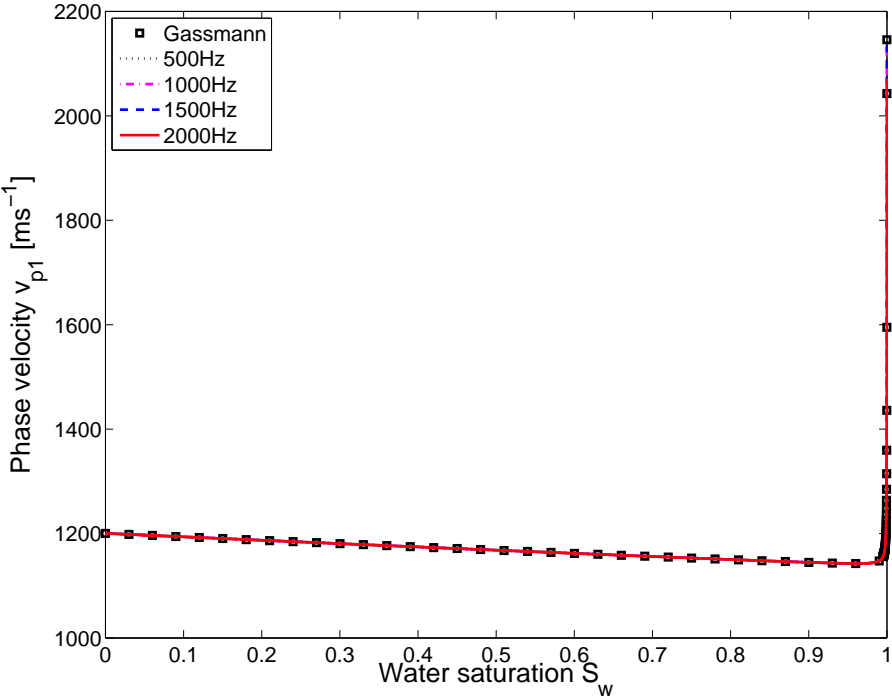
(a) Velocity
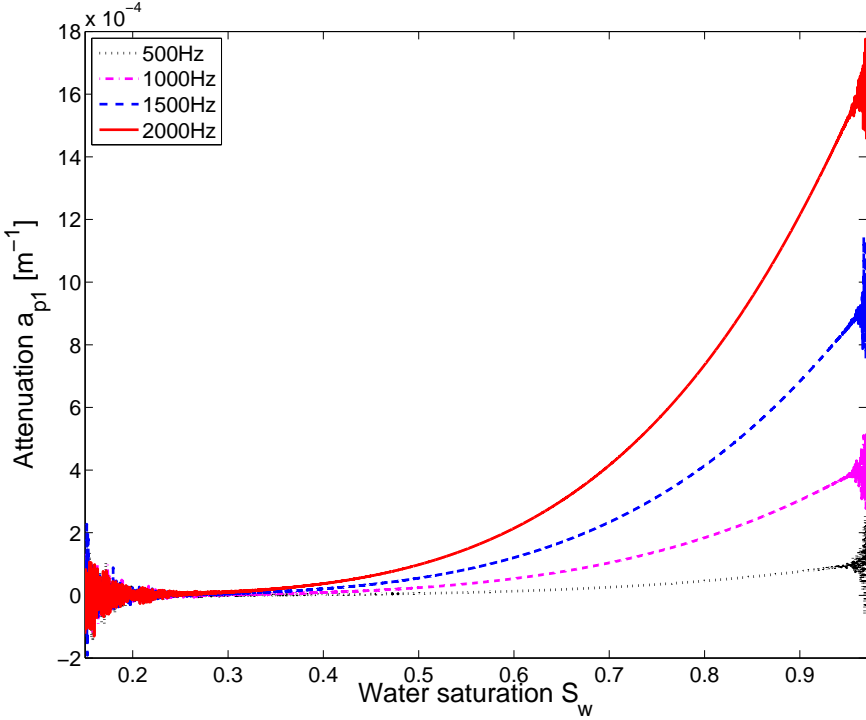
(b) Attenuation

Figure 3.2: The fast compressional wave versus water saturation
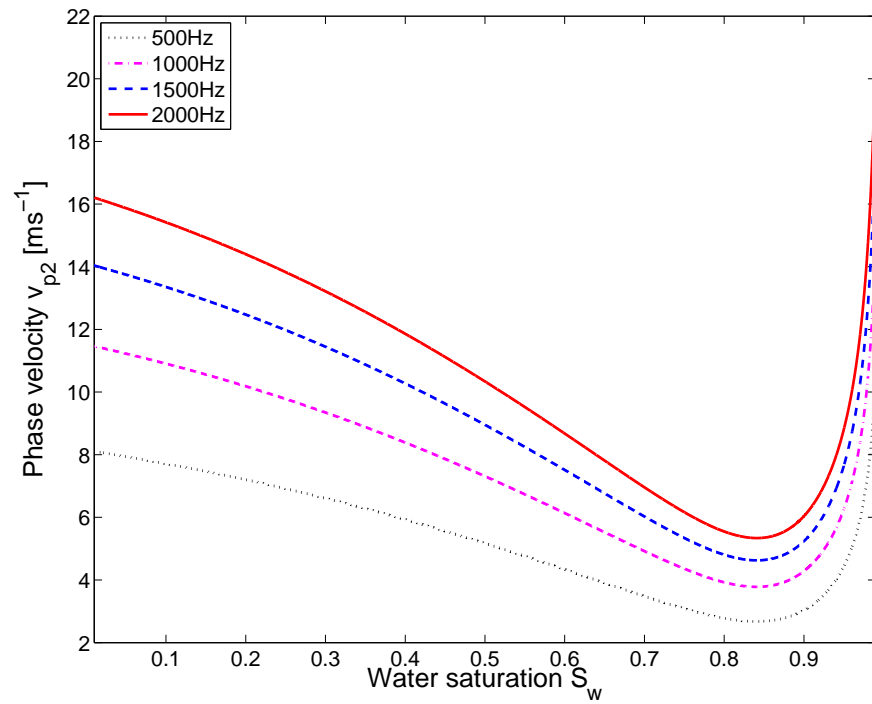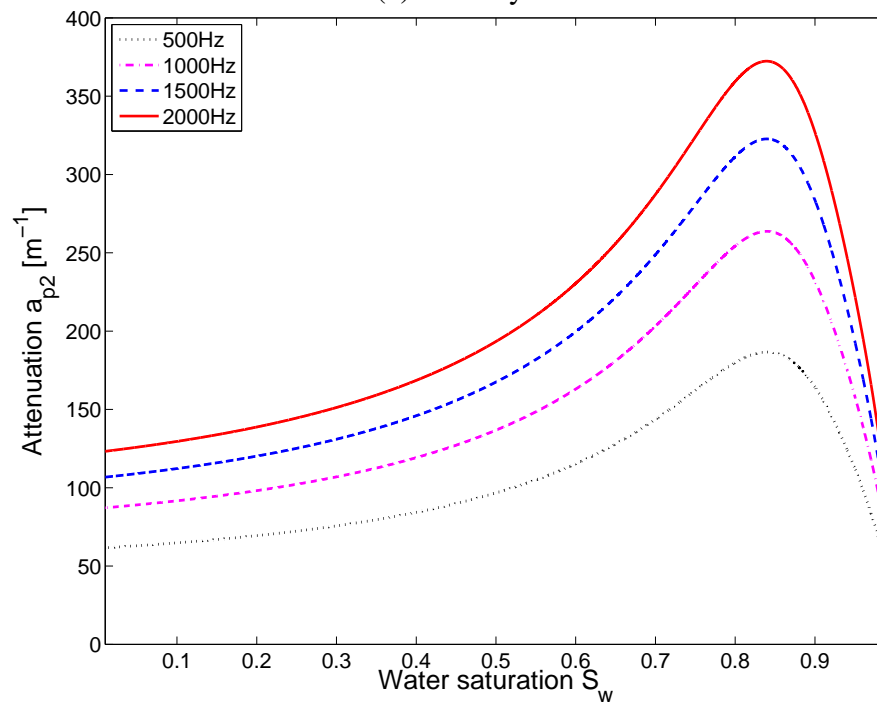
(a) Velocity

(b) Attenuation

Figure 3.3: The second slow compressional wave versus water saturation
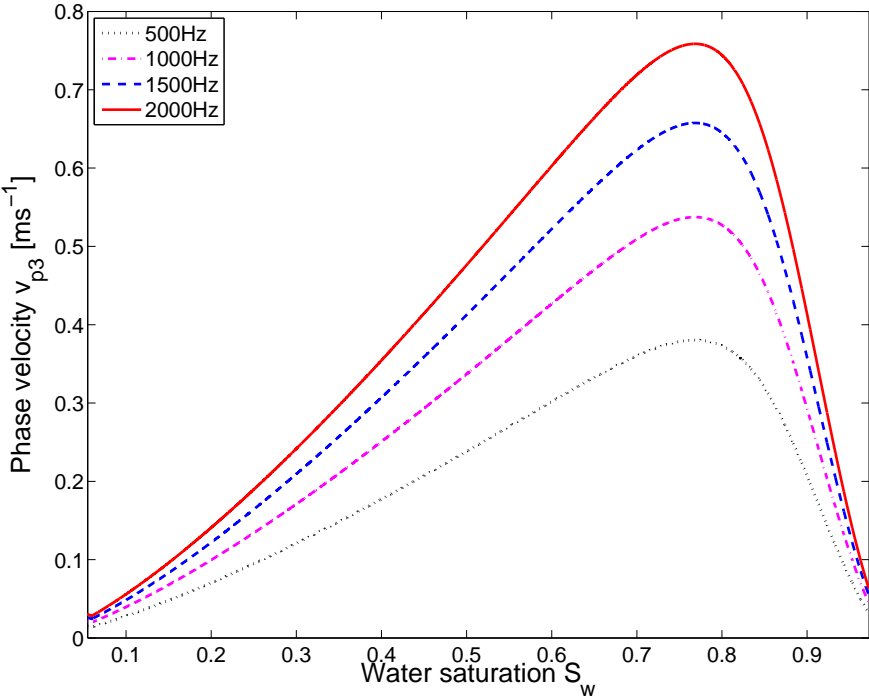
(a) Velocity
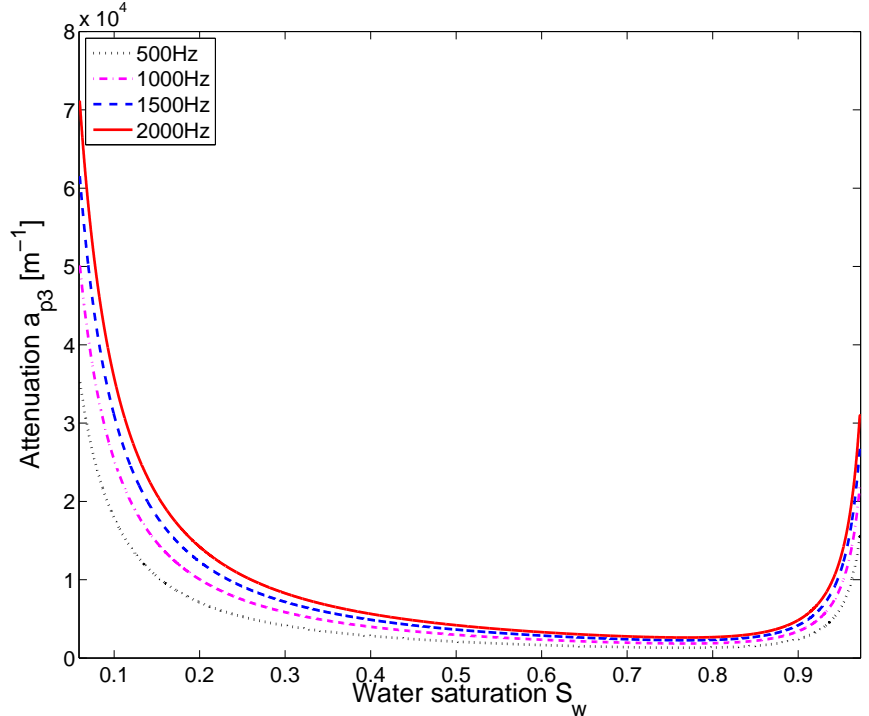
(b) Attenuation

Figure 3.4: The third slow compressional wave versus water saturation

since K_a is very small compared to K_w, K^* will not change too much until S_w increases to some value, i.e., $S_w = 0.999$, when K^* increases rapidly. Besides, the fast wave is almost frequency independent. Only when the water saturation is very close to 1 there exist tiny differences of the wave velocity for different frequencies.

The second and the third slow waves are much slower compared to the fast wave. The second slow wave velocity v_{p_2} decreases with increasing the saturation degree to the value $S_w = 0.85$, then it increases very fast (see figure 3.3(a)). The third slow wave velocity v_{p_3} increases with increasing the saturation degree to the value $S_w = 0.75$, then it decreases very fast (see figure 3.4(a)). Both slow waves are frequency dependent and the wave velocities increase with increasing the frequency. This fits to the results of Albers [4] and can be understood if the different states of the fluid combinations are considered. Bao et al. [11] summarized the different features for the four air phase patterns:

1. Wholly continuous stage ($S_w < 0.55$), where the moisture only exists in the smaller voids and the water is not necessarily interconnected, the air phase is continuous in the soil mass and connected to the atmosphere.

2. Partially continuous stage ($0.55 \leq S_w \leq 0.85$), where the moisture will gradually occupy all the smaller pore passageways, the air phase is accumulating in the larger voids and it is still connected to the atmosphere.

3. Internally continuous stage ($0.85 \leq S_w \leq 0.90$), where the water will begin to occupy the larger pore passageways and seal off the boundary voids of the soil mass, the air phase is not connected to the atmosphere, but inside the soil mass it remains to be connected.

4. Completely sealed stage ($S_w > 0.90$), where the water with occluded air bubbles occupy all the pore passageways, the air phase will appear only in the form of occluded air bubbles suspended in and moving with the water.

Based on these considerations it is clear why there is a turning point for both phase velocities.

In figure 3.2(b), the attenuation of the fast wave is extremely small and may be neglected. This is the reason why the fast wave is always easy to detect. On the other hand, the attenuation of the two slow waves is very large (see figure 3.3(b) and 3.4(b)), especially for the third slow wave, the value can be as high as $a_{p3} = 7 \times 10^4 \, 1/\text{m}$. The two slow waves are highly damped caused by the viscous interaction of the fluids with the solid and the suction effect. The attenuation of all the three waves is frequency dependent and the attenuation becomes higher with increasing the frequency.

After investigating the wave behavior, next the behavior of the displacement and the pore pressure is studied under a stress boundary condition. Assuming the values $S_0 = 1 \, \text{N}/\text{m}^2$ and $\ell = 10 \, \text{m}$, the displacement at the top of the column ($y = \ell$) and the pore pressure at the bottom of the column ($y = 0$) are calculated with varying saturation degree.

Results in the frequency domain   As shown in figure 3.5 – 3.7, the curves of the absolute displacement $abs(u(\omega, y = \ell))$ at the top of the column and the absolute pore pressure $abs(p^f(\omega, y = 0))$ $(f = w, a)$ at the bottom of the column versus frequency with varying saturation degree are plotted.

The displacement results are compared with the solution of a one dimensional saturated poroelastic column [102]. The saturation degree S_w is changed in figure 3.5 from $S_w = 0.50$ to $S_w = 0.99999$. The different values of the initial saturation degree chosen in the calculations only aim to study the effects caused by the partial saturation. Some of the given values may not be the realistic cases. The value $S_w = 0.99999$ can be seen as limit to the saturated case and it is shown in figure 3.5 that the eigenfrequencies of the saturated and nearly saturated cases coincide. The number of the eigenfrequencies in a given frequency range (ω varies from 0 to 1500 according to the figure) is for the partially saturated cases twice more than that of the saturated and nearly saturated case. For the starting point of the curves in figure 3.5(a), it is observed that the displacement value of the partially saturated cases is larger than that of the saturated and nearly saturated cases. Since the very low frequency behavior may reflect a long time behavior, the difference between the starting points can be explained. Because the long time or static displacement depends on the compressibility of the continuum. For the saturated and nearly saturated cases, the material shows a larger compressibility value which can lead to a smaller displacement. Similarly, a larger compressibility also results in less number of eigenfrequencies in a given frequency range.

For the pore water and pore air pressure, the results show similar behavior as the displacement result (see figure 3.6 and 3.7). For the saturated and nearly saturated cases, the number of the eigenfrequencies is less compared with that of the partially saturated cases. It is interesting that for the nearly saturated case, the starting point of the pore water pressure is much higher compared with that of the partially saturated cases, while the starting point of the pore air pressure for the nearly saturated case is smaller compared with that of the partially saturated cases. This phenomenon is reasonable because for a nearly saturated condition, the stress applied on the solid skeleton can be more effectively transferred to the pore water while the effect induced by the water air interaction is too small to be considered.

Results in the time domain   The time domain results are calculated by using the convolution quadrature method as mentioned before by choosing the time step size to $\Delta t = 1 \times 10^{-5}$ s. The displacement at the top of the column ($y = \ell$) are calculated and displayed in figure 3.8 versus time with varying saturation degree.

For the nearly saturated case $S_w = 0.9999$, the result coincides well with that of the saturated case [102]. For smaller water saturation, larger displacements and slower wave
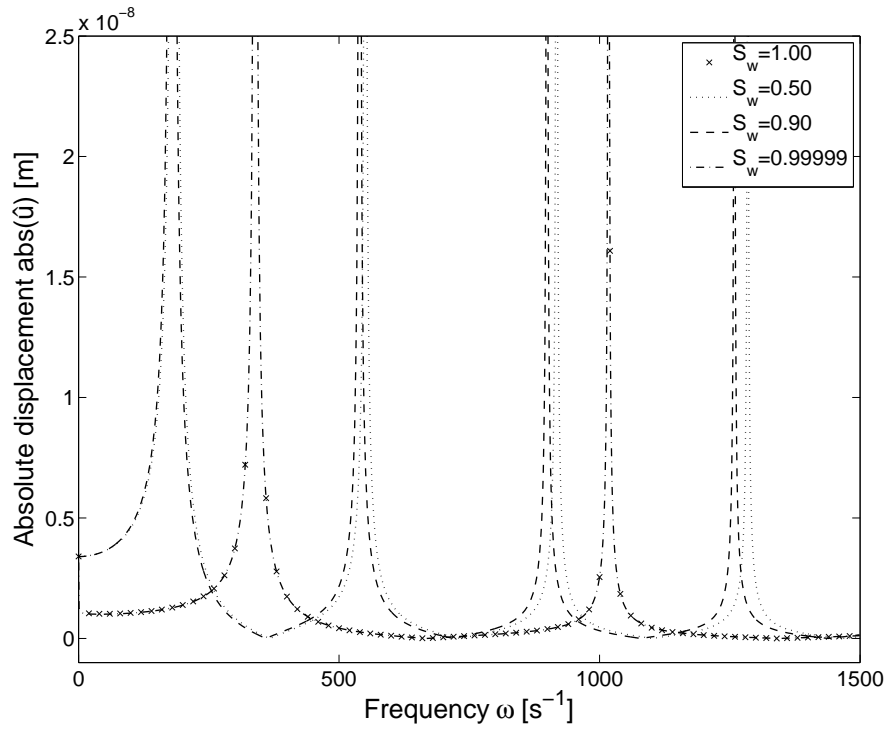
Figure 3.5: Absolute displacement abs($\hat{u}(\omega, y = \ell)$) versus frequency with varying water saturation

velocities are observed. It is also clear that no matter whether S_w is 0.5 or 0.9, the displacements and the wave velocities are nearly the same because the effective bulk modulus will not change too much for this range of the water saturation.

Similar results are found for the pore water pressure. In figure 3.10(a), it is plotted versus time at the bottom of the column ($y = 0$) under the same stress boundary condition as above.

The pore air pressure has much smaller values as displayed in figure 3.9. Clearly, the smallest value of the pore air pressure is given for the nearly saturated case. By decreasing the saturation degree the pore air pressure firstly increases and then decreases.

The pore water pressure of the nearly saturated case ($S_w = 0.9999$) is very close to that of the saturated case, and the value is about 1.5 times larger than that created by the static Skempton effect. However, for smaller water saturation, the pore water pressure is very low (see the zoom in figure 3.10(b)).

Remark 1.   It should be remarked that the oscillations at the jumps in the pressure solutions are numerical effects. They can not be avoided but changed by the time step size and the chosen multistep method.
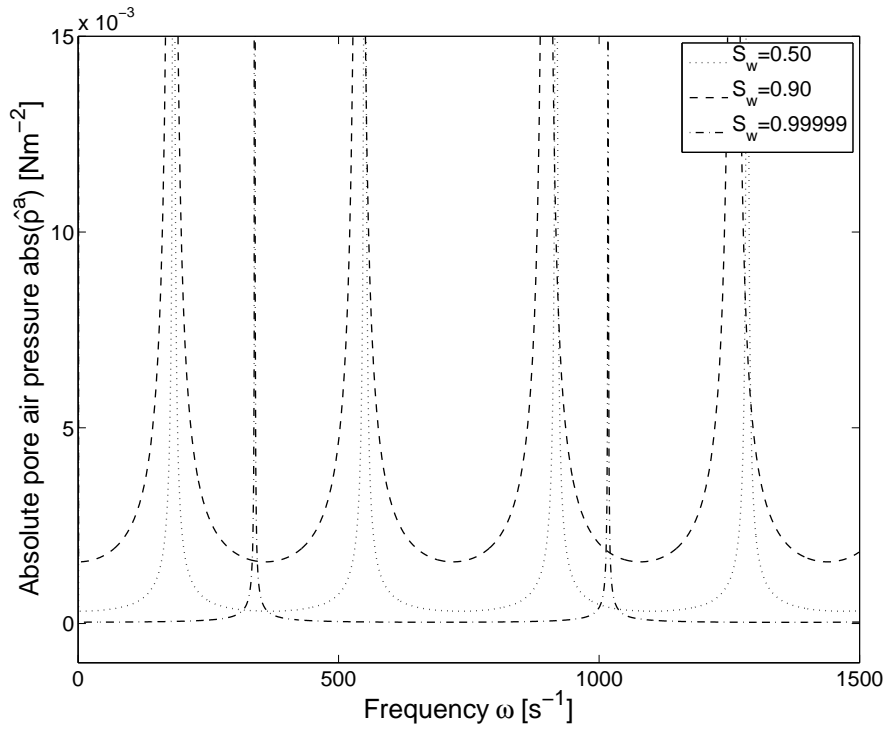
Figure 3.6: Absolute pore air pressure abs($\hat{p}^a(\omega, y = 0)$) versus frequency with varying water saturation

In figure 3.8 – 3.10, it is impossible to detect the two slow compressional waves due to the high attenuation. This can be overcome by reducing the viscosity artificially, i.e., two arbitrarily large permeability

$$\kappa_w = 1.0 \times 10^3 \, {}^{\text{m}^4}\!/\text{Ns}$$
$$\kappa_a = 1.0 \times 10^3 \, {}^{\text{m}^4}\!/\text{Ns}$$

are chosen.

Further, because of the higher wave speed of the fast compressional wave, several reflections would disturb the figure before the slow waves are visible. That is why an "infinite" column with a length $\ell = 1000\,\text{m}$ is set and the pressures are observed thirty meters below the excitation point. The water saturation is set to $S_w = 0.99$ in the calculation.

As shown in figure 3.11 and 3.12, the pore water pressure has two step jumps while the pore air pressure has three. This phenomenon can be rationalized as follows. For the pore water pressure, the first jump is the arrival of the fast wave. The second slow wave, arriving at a later time, is of negative amplitude and cancels the fast wave. However, the third slow wave can not be detected. For the pore air pressure, the fast wave and the second slow wave arrive at the same time as the waves visible in the pore water pressure solution.
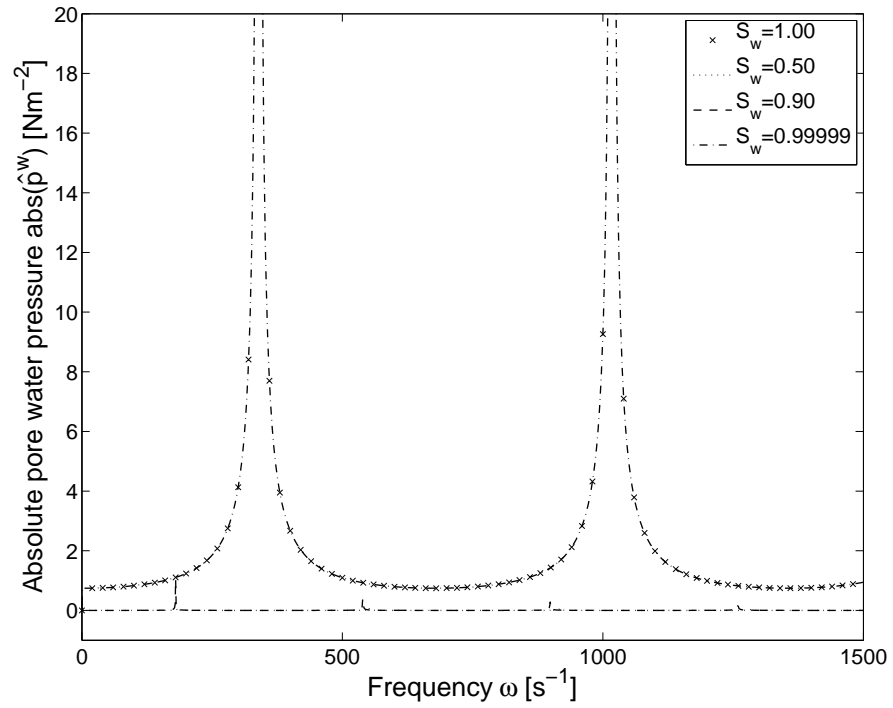
(a) Full scale
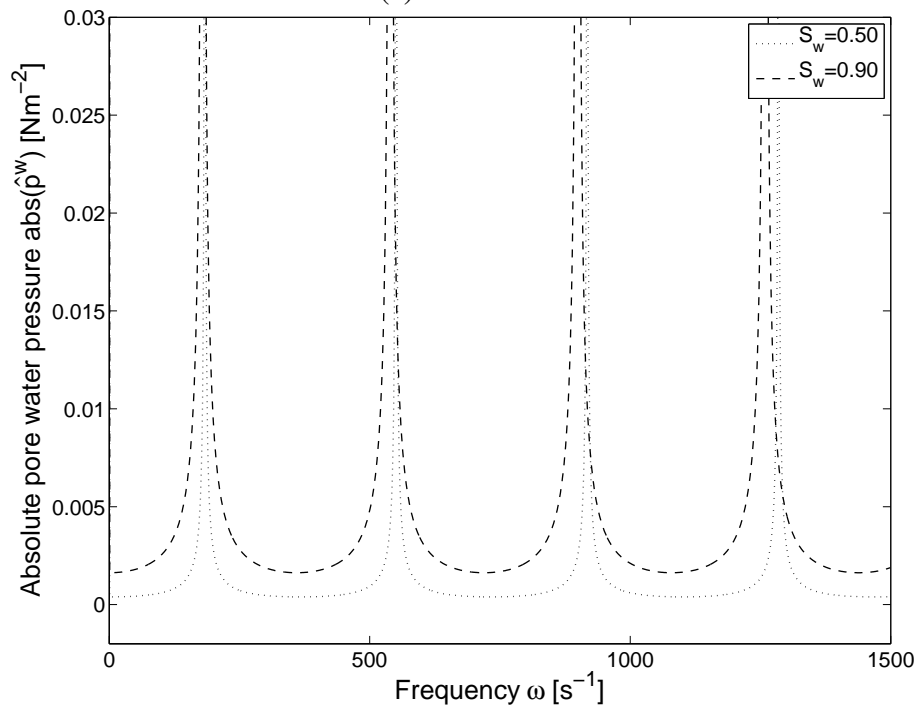
(b) Zoom

Figure 3.7: Absolute pore water pressure abs($\hat{p}^w(\omega, y = 0)$) versus frequency with varying water saturation
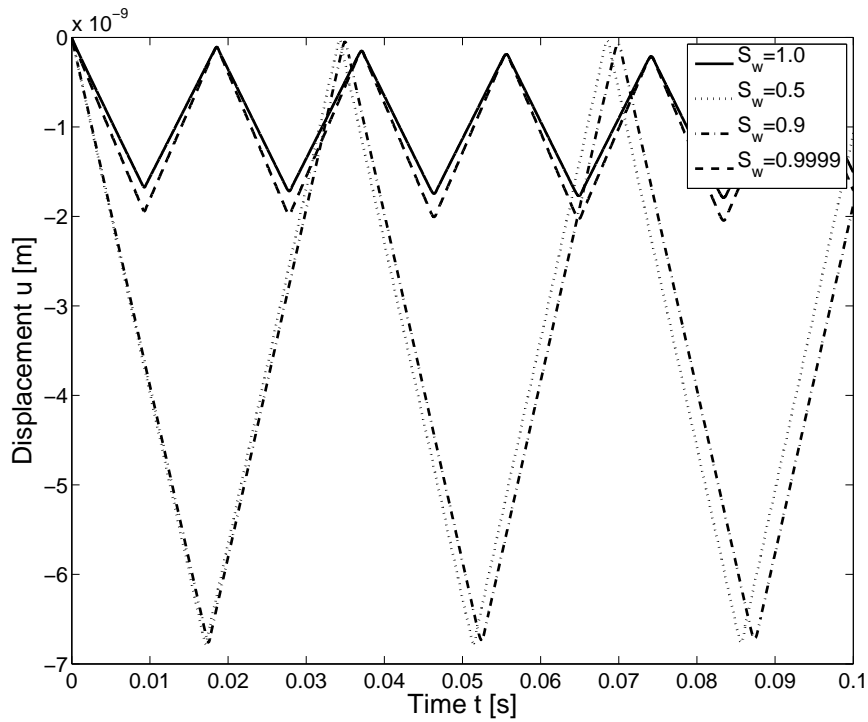
Figure 3.8: Displacement $u(t, y = \ell)$ versus time with varying water saturation
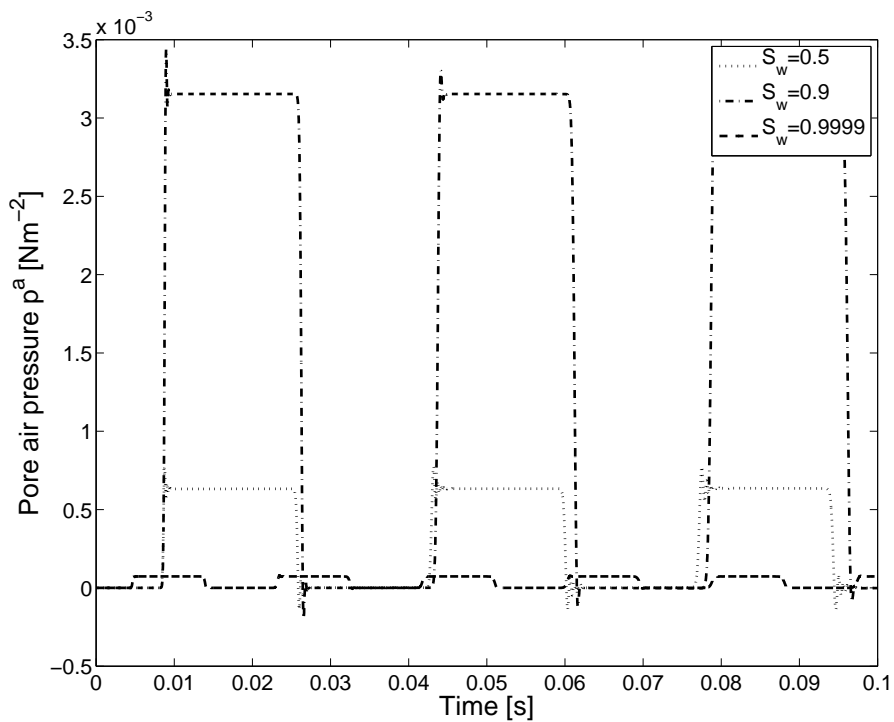
Figure 3.9: Pore air pressure $p^a(t, y = 0)$ versus time with varying water saturation

(a) Full scale

(b) Zoom
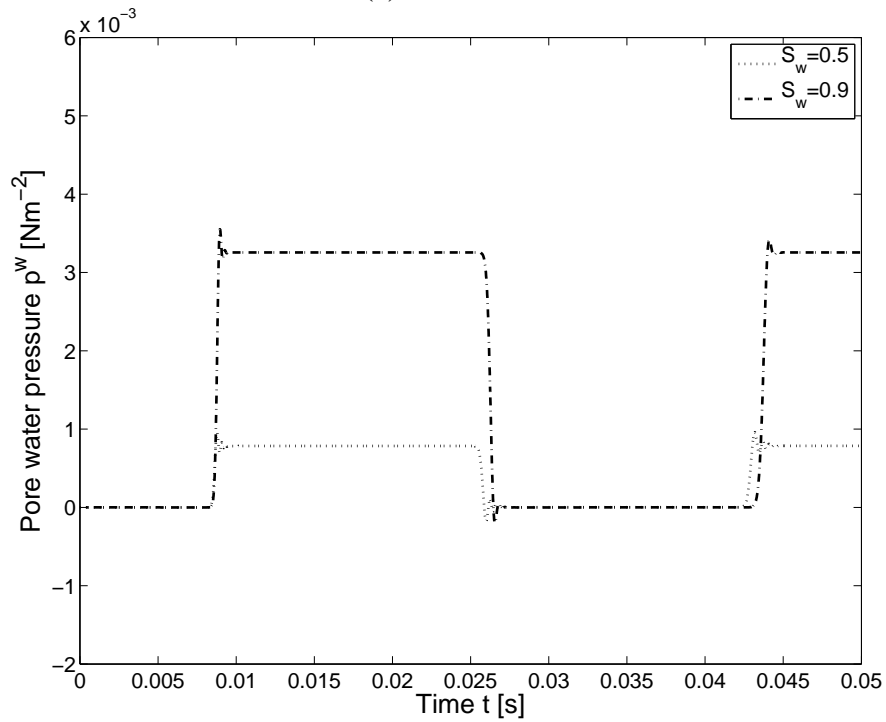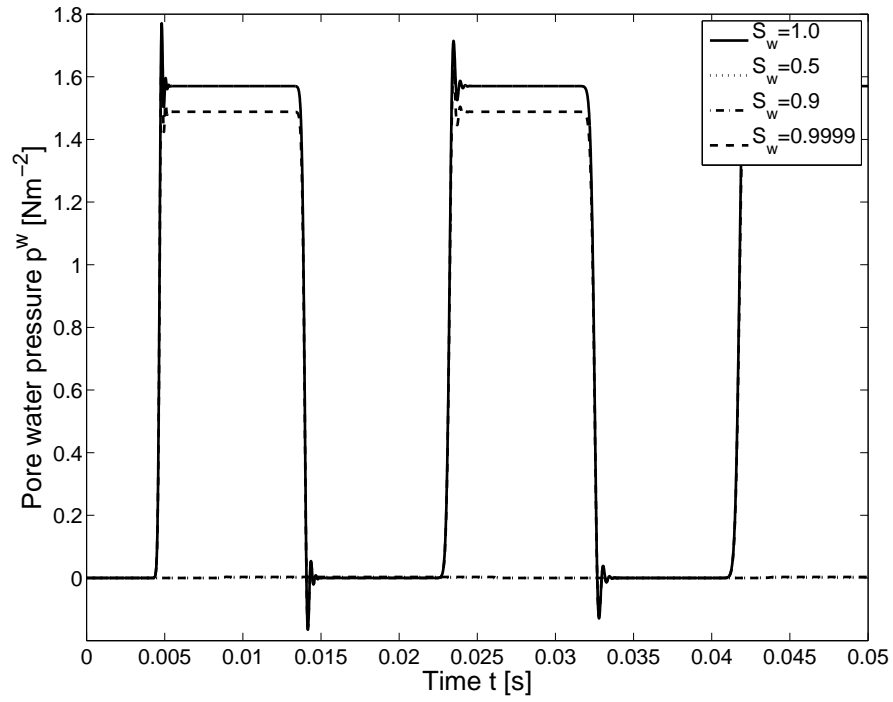
Figure 3.10: Pore water pressure $p^w(t, y = 0)$ versus time with varying water saturation
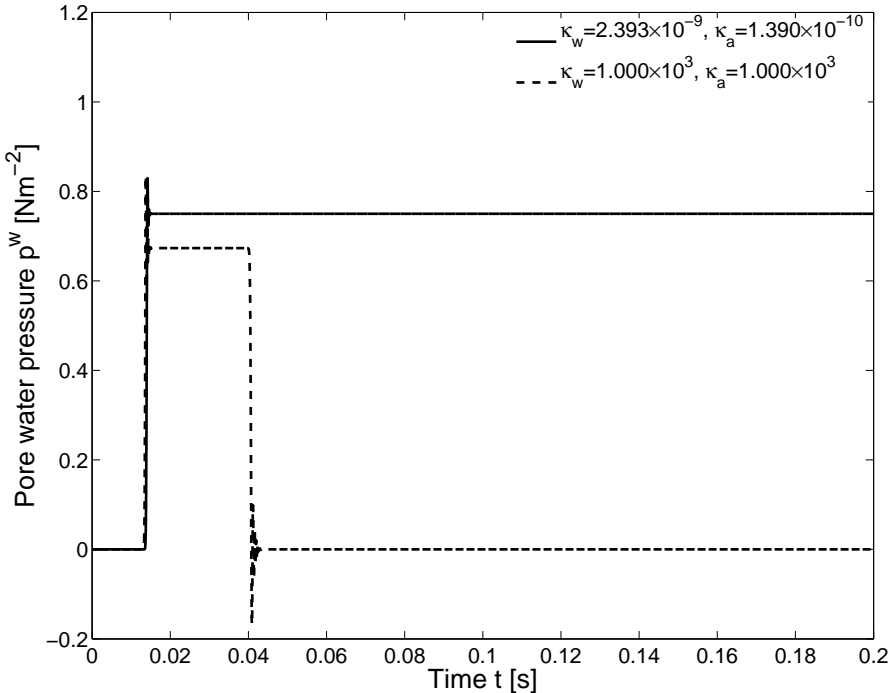
Figure 3.11: Pore water pressure $p^w(t, y = 970)$ versus time with varying κ_w
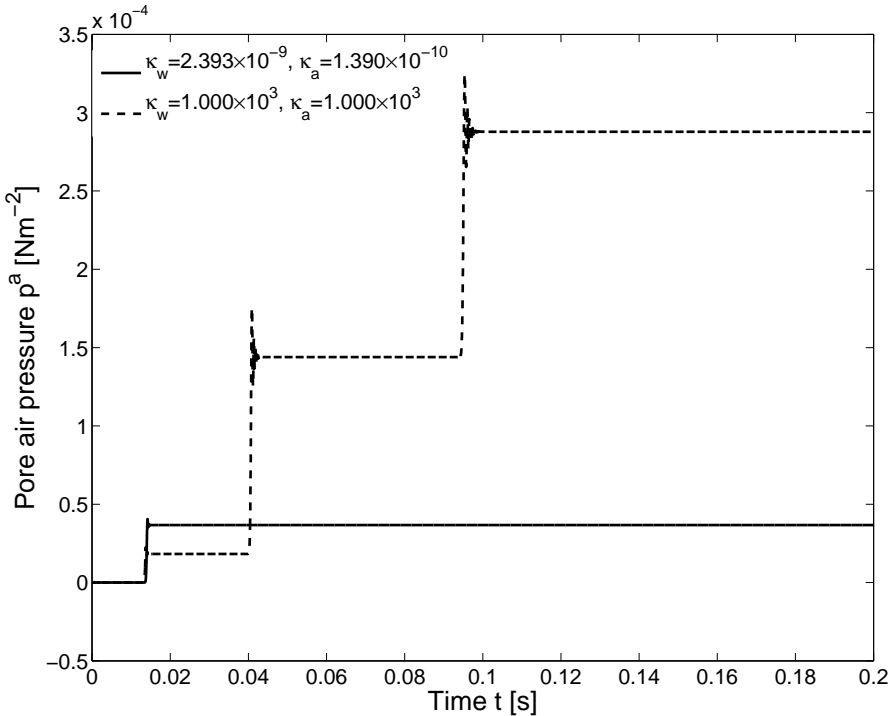
Figure 3.12: Pore air pressure $p^a(t, y = 970)$ versus time with varying κ_a

The difference is that the second slow wave is of positive amplitude and enlarges the fast wave. The third slow wave arriving at a later time is also of positive amplitude and keeps enlarging the overlapped waves.

As mentioned above, when calculating with the real permeability, for both the pore water and the pore air pressure the slow waves are rapidly dissipated such that they have no effect when they arrive at the observation point. Therefore, only the arrival of the fast wave can be observed in experiments. Besides, the amplitude of the pore water pressure is slightly affected by changing the permeability. For the pore air pressure this is true only for the fast compressional wave whereas the amplitudes of the slow waves are strongly increasing with increasing the permeability.

Remark 2.   As already discussed in chapter 2, the governing equations hold only for a spatially constant saturation degree. Hence, also this analytical solution is restricted. This may be conflict with a realistic column under the influence of gravity. However, it may have not too much influence on the travelling waves.

Summarizing, there exist three compressional waves, however, for most natural materials the permeability may never become such large numbers making the slow compressional waves visible.

4 FUNDAMENTAL SOLUTIONS

In order to establish the boundary integral equation related to the set of coupled differential equations, one crucial condition is the knowledge of corresponding fundamental solutions. The fundamental solution is the weighting function that is used in the boundary integral equations. In this chapter, the fundamental solutions are derived following Hörmander's method. Parts of the fundamental solutions are calculated and plotted in both the frequency and time domain. Besides, they are compared with the saturated poroelastic fundamental solutions in a limiting process of the saturation degree S_w.

4.1 Hörmander's method

Fundamental solutions $\hat{\mathbf{U}}$ are derived for partially saturated poroelasticity based on the governing equations (2.39).

Following Hörmander's method [63], the coupled differential equations (2.39) have to be solved with a Dirac distribution as inhomogeneity for every degree of freedom. The fundamental solution $\hat{\mathbf{U}} = \hat{\mathbf{U}}(\mathbf{x}, \mathbf{y})$ of a differential operator $\mathcal{B}$ is a full space solution of the differential equations and are given by

$$\mathcal{B}^* \, \hat{\mathbf{U}} + \mathbf{I}\delta(\mathbf{x}, \mathbf{y}) = \mathbf{0} \quad , \tag{4.1}$$

where $\mathcal{B}^*$ is the ad-joint operator of $\mathcal{B}$ and is given by

$$\mathcal{B}^* = \begin{bmatrix} A_1\delta_{ij} + A_2\partial_i\partial_j & -A_5\partial_i & -A_8\partial_i \\ -A_3\partial_j & A_6 & A_9 \\ -A_4\partial j & A_7 & A_{10} \end{bmatrix} \quad . \tag{4.2}$$

The negative sign in (4.2) comes from the first order partial derivative term. $\mathbf{I}$ denotes the identity matrix and $\delta(\mathbf{x}, \mathbf{y})$ denotes the Dirac distribution. Using the ad-joint operator here is because the fundamental solutions should satisfy the ad-joint operator. However, for partially saturated case, the operator $\mathcal{B}$ is not self–adjoint. The fundamental solution relates the effect of a point source at the load point $\mathbf{y}$ to the field point $\mathbf{x}$.

It is assumed that

$$\hat{\mathbf{U}} = \mathcal{B}^{*co}\varphi \tag{4.3}$$

holds, where $\mathcal{B}^{*co}$ denotes the co–factors of $\mathcal{B}^*$ and φ is some scalar function.

This leads to

$$\mathcal{B}^* \cdot \mathcal{B}^{*co} \varphi + \mathbf{I}\delta(\mathbf{x}, \mathbf{y}) = \mathbf{0} \quad ,$$

where the property

$$\mathcal{B}^* \cdot \mathcal{B}^{*co} = \det(\mathcal{B}^*)\mathbf{I}$$

yields an equation to determine the scalar function φ

$$\det(\mathcal{B}^*)\mathbf{I}\varphi + \mathbf{I}\delta(\mathbf{x}, \mathbf{y}) = \mathbf{0}$$
$$\implies \det(\mathcal{B}^*)\varphi + \delta(\mathbf{x}, \mathbf{y}) = 0$$

(4.4)

From the equation (4.4), it is obvious that the solution of (4.1) requires the matrix of co–factors $\mathcal{B}^{*co}$ as well as the determinant $\det(\mathcal{B}^*)$. Rules known from the matrix calculus can be transformed analogous to matrix differential operator $\mathcal{B}^*$. The matrix of co–factors $\mathcal{B}^{*co}$ can be calculated as

$$\mathcal{B}^{*co} = \det(\mathcal{B}^*) \cdot \mathcal{B}^{*-1}$$

(4.5)

where $\mathcal{B}^{*-1}$ is the inverse matrix of $\mathcal{B}^*$.

After the determination of the scalar function φ, by backward substitution, the fundamental solution $\hat{\mathbf{U}}$ can be determined.

The determinant of the ad-joint operator $\mathcal{B}^*$ is calculated as

$$\det(\mathcal{B}^*) = \frac{a_1^2(a_1 + a_3)a_7a_{11}}{s^2}(\nabla^2 - \frac{a_2}{a_1}s^2)^2(\nabla^6 + D_1\nabla^4 + D_2\nabla^2 + D_3)$$

(4.6)

where the full forms of the symbols in (4.6) are

$$D_1 = -s^2 \left[\frac{a_6}{a_7} + \frac{a_{10}}{a_{11}} + \frac{a_2}{a_1 + a_3} + \frac{a_4^2 a_{11} + a_5^2 a_7}{(a_1 + a_3)a_7a_{11}} \right] \quad ,$$

$$D_2 = s^4 \left[\frac{a_6a_{10} - a_8a_9}{a_7a_{11}} + \frac{a_2(a_6a_{11} + a_7a_{10}) + a_4^2 a_{10} + a_5^2 a_6 + a_4a_5(a_8 + a_9)}{(a_1 + a_3)a_7a_{11}} \right] \quad ,$$

$$D_3 = s^6 \frac{a_2(a_8a_9 - a_6a_{10})}{(a_1 + a_3)a_7a_{11}} \quad ,$$

$$a_1 = G \quad ,$$

$$a_2 = \rho - \beta S_w\rho_w - \gamma S_a\rho_a \quad ,$$

$$a_3 = K + \frac{G}{3} \quad ,$$

$$a_4 = (\alpha - \beta)S_w \quad ,$$

$$a_5 = (\alpha - \gamma)S_a \quad ,$$

$$a_6 = \zeta S_{ww}S_w + \frac{n}{K_w}S_w - S_u \quad ,$$

$$a_7 = \frac{\beta S_w}{\rho_w} \quad ,$$

$$a_8 = \zeta S_{aa} S_w + S_u \quad ,$$

$$a_9 = \zeta S_{ww} S_a + S_u \quad ,$$

$$a_{10} = \zeta S_{aa} S_a + \frac{n}{K_a} S_a - S_u \quad ,$$

$$a_{11} = \frac{\gamma S_a}{\rho_a} \quad .$$

From the equation (4.6), the determinant can be expressed as

$$\det(\mathcal{B}^*) = \frac{a_1^2(a_1 + a_3)a_7 a_{11}}{s^2}(\nabla^2 - \lambda_1^2)(\nabla^2 - \lambda_2^2)(\nabla^2 - \lambda_3^2)(\nabla^2 - \lambda_4^2)^2 \quad , \tag{4.7}$$

where there are obvious four roots resulting from the determinant equation including three different roots λ_i^2 $(i = 1, 2, 3)$ corresponding to the fast and slow compressional waves, and one double root λ_4^2 corresponding to the shear wave.

Solving the determinant equation $\det(\mathcal{B}^*) = 0$, the four roots are obtained and given by

$$\lambda_1^2 = -\frac{1}{3}\left(D_1 + \sqrt[3]{\frac{m + \sqrt{n}}{2}} + \sqrt[3]{\frac{m - \sqrt{n}}{2}}\right) \tag{4.8a}$$

$$\lambda_2^2 = -\frac{1}{3}\left(D_1 + k_2\sqrt[3]{\frac{m + \sqrt{n}}{2}} + k_1\sqrt[3]{\frac{m - \sqrt{n}}{2}}\right) \tag{4.8b}$$

$$\lambda_3^2 = -\frac{1}{3}\left(D_1 + k_1\sqrt[3]{\frac{m + \sqrt{n}}{2}} + k_2\sqrt[3]{\frac{m - \sqrt{n}}{2}}\right) \tag{4.8c}$$

$$\lambda_4^2 = \frac{a_2}{a_1}s^2 = \frac{\rho - \beta S_w \rho_w - \gamma S_a \rho_a}{G}s^2 \quad , \tag{4.8d}$$

with

$$m = 2D_1^3 - 9D_1 D_2 + 27D_3 \quad ,$$

$$n = m^2 - 4(D_1^2 - 3D_2)^3 \quad ,$$

$$k_1 = \frac{-1 + i\sqrt{3}}{2} \quad ,$$

$$k_2 = \frac{-1 - i\sqrt{3}}{2} \quad .$$

Finally, the determinant is

$$\det(\mathcal{B}^*) = (K + \frac{4}{3}G)\frac{G^2 \beta \gamma S_w S_a}{\rho_w \rho_a s^2}(\nabla^2 - \lambda_1^2)(\nabla^2 - \lambda_2^2)(\nabla^2 - \lambda_3^2)(\nabla^2 - \lambda_4^2)^2 \quad , \tag{4.9}$$

by replacing the abbreviations a_i.

Substituting in equation (4.4), it follows

$$(K + \frac{4}{3}G)\frac{G^2\beta\gamma S_w S_a}{\rho_w \rho_a s^2}(\nabla^2 - \lambda_1^2)(\nabla^2 - \lambda_2^2)(\nabla^2 - \lambda_3^2)(\nabla^2 - \lambda_4^2)^2 \varphi = 0 \quad , \tag{4.10}$$

where the scalar function φ has to be found [32, 34]. It turns out to be a Helmholtz equation of higher order.

4.2 Solution to high order Helmholtz equations

The generalized form of the high order Helmholtz equation is given by

$$\Psi_n(\nabla^2 + \lambda_1^2)(\nabla^2 + \lambda_2^2)...(\nabla^2 + \lambda_n^2) = \delta(\mathbf{x}, \mathbf{y}) \tag{4.11}$$

where the constants λ_i, $i = 1, ..., n$, are the eigenvalues of the decoupled partial differential equation system.

Varying the value of the order factor n, the equation (4.11) can be expressed as

$$\Psi_n(\nabla^2 + \lambda_n^2) = \Psi_{n-1}$$
$$\Psi_{n-1}(\nabla^2 + \lambda_{n-1}{}^2) = \Psi_{n-2}$$
$$\vdots$$
$$\Psi_2(\nabla^2 + \lambda_2^2) = \Psi_1$$
$$\Psi_1(\nabla^2 + \lambda_1^2) = \delta(\mathbf{x}, \mathbf{y}) \quad .$$

The solution Ψ_1 is well know as

$$\Psi_1 = -\frac{1}{2}\frac{ie^{i\lambda_1 r}}{\lambda_1} \tag{4.13a}$$

$$\Psi_1 = -\frac{1}{4}iH_0^{(1)}(\lambda_1 r) \tag{4.13b}$$

$$\Psi_1 = -\frac{1}{4\pi r}e^{i\lambda_1 r} \tag{4.13c}$$

for the one dimensional, two dimensional and three dimensional solutions, respectively. $i = \sqrt{-1}$, $r = |\mathbf{x} - \mathbf{y}|$, and $H_0^{(1)}$ is the Hankel function of the first kind of order zero [1]. In the following, only the three dimensional solution is discussed.

Replacing Ψ_1 in the equation $\Psi_2(\nabla^2 + \lambda_2^2) = \Psi_1$ gives

$$\Psi_2(\nabla^2 + \lambda_2^2) = -\frac{1}{4\pi r}e^{i\lambda_1 r} \quad . \tag{4.14}$$

With inspection, the solution of the equation (4.14) can be found as

$$\Psi_2 = -\frac{1}{4\pi r}\left(\frac{e^{i\lambda_1 r}}{\lambda_2^2 - \lambda_1^2} + \frac{e^{i\lambda_2 r}}{\lambda_1^2 - \lambda_2^2}\right) \quad . \tag{4.15}$$

Following this way, the solution Ψ_3 of a three order Helmholtz equation can be found as

$$\Psi_3 = -\frac{1}{4\pi r}\left[\frac{e^{i\lambda_1 r}}{(\lambda_2^2 - \lambda_1^2)(\lambda_3^2 - \lambda_1^2)} + \frac{e^{i\lambda_2 r}}{(\lambda_1^2 - \lambda_2^2)(\lambda_3^2 - \lambda_2^2)} + \frac{e^{i\lambda_3 r}}{(\lambda_1^2 - \lambda_3^2)(\lambda_2^2 - \lambda_3^2)}\right] \quad , \tag{4.16}$$

which is used for the saturated poroelasticity fundamental solutions.

The solution Ψ_4 of a four order Helmholtz equation can be found as

$$\Psi_4 = -\frac{1}{4\pi r}\left[\frac{e^{i\lambda_1 r}}{(\lambda_2^2 - \lambda_1^2)(\lambda_3^2 - \lambda_1^2)(\lambda_4^2 - \lambda_1^2)} + \frac{e^{i\lambda_2 r}}{(\lambda_1^2 - \lambda_2^2)(\lambda_3^2 - \lambda_2^2)(\lambda_4^2 - \lambda_2^2)}\right.$$
$$\left. + \frac{e^{i\lambda_3 r}}{(\lambda_1^2 - \lambda_3^2)(\lambda_2^2 - \lambda_3^2)(\lambda_4^2 - \lambda_3^2)} + \frac{e^{i\lambda_4 r}}{(\lambda_1^2 - \lambda_4^2)(\lambda_2^2 - \lambda_4^2)(\lambda_3^2 - \lambda_4^2)}\right] \quad , \tag{4.17}$$

which is used for the partially saturated poroelasticity fundamental solutions.

A general solution for any order of the Helmholtz equation is given by

$$\Psi_n = -\frac{1}{4\pi r}\sum_{i=1}^{n}\frac{e^{i\lambda_i r}}{\prod_{j=1, j\neq i}^{4}(\lambda_j^2 - \lambda_i^2)} \quad . \tag{4.18}$$

The derivation of the solution Ψ_n is purely for the sake of solving the scalar function φ in (4.4).

4.3 Partially saturated poroelastodynamic fundamental solutions

Substituting

$$\Psi = (K + \frac{4}{3}G)\frac{G^2\beta\gamma S_w S_a}{\rho_w\rho_a s^2}(\nabla^2 - \lambda_4^2)\varphi \tag{4.19}$$

in equation (4.10) leads to

$$\Psi(\nabla^2 - \lambda_1^2)(\nabla^2 - \lambda_2^2)(\nabla^2 - \lambda_3^2)(\nabla^2 - \lambda_4^2) + \delta(\mathbf{x}, \mathbf{y}) = 0 \quad , \tag{4.20}$$

which is just a fourth order Helmholtz equation and the solution is given in (4.17).

Solving the equation $\mathcal{B}^{*co} = \det(\mathcal{B}^*)\mathcal{B}^{*-1}$, the matrix of the co–factors $\mathcal{B}^{*co}$ is given by

$$\mathcal{B}^{*co} = A_1 \begin{bmatrix} (X_1 - X_2\nabla^2)\delta_{ij} + X_2\partial_{ij} & X_3\partial_i & X_4\partial_i \\ X_5\partial_j & X_7 & X_8 \\ X_6\partial_j & X_9 & X_{10} \end{bmatrix} \quad , \tag{4.21}$$

where the explicit forms of the symbols are

$$A_1 = G\nabla^2 - (\rho - \beta S_w\rho_w - \gamma S_a\rho_a)s^2 \quad ,$$
$$X_1 = r_1\nabla^6 + r_2\nabla^4 + r_3\nabla^2 + r_4 \quad ,$$
$$X_2 = r_5\nabla^4 + r_6\nabla^2 + r_7 \quad ,$$
$$X_3 = r_8\nabla^4 + r_9\nabla^2 + r_{10} \quad ,$$
$$X_4 = r_{11}\nabla^4 + r_{12}\nabla^2 + r_{13} \quad ,$$
$$X_5 = r_{14}\nabla^4 + r_{15}\nabla^2 + r_{16} \quad ,$$
$$X_6 = r_{17}\nabla^4 + r_{18}\nabla^2 + r_{19} \quad ,$$
$$X_7 = r_{20}\nabla^6 + r_{21}\nabla^4 + r_{22}\nabla^2 + r_{23} \quad ,$$
$$X_8 = r_{24}\nabla^4 + r_{25}\nabla^2 + r_{26} \quad ,$$
$$X_9 = r_{27}\nabla^4 + r_{28}\nabla^2 + r_{29} \quad ,$$
$$X_{10} = r_{30}\nabla^6 + r_{31}\nabla^4 + r_{32}\nabla^2 + r_{33} \quad .$$

The explicit forms of the variables r_i $(i = 1, 2, ..., 33)$ can be found in appendix A.1.2.

Applying the matrix of the co–factors $\mathcal{B}^{*co}$ on φ results in the fundamental solutions for partially saturated poroelasitcity

$$\hat{\mathbf{U}} = \begin{bmatrix} \hat{U}^{ss}_{ij} & \hat{U}^{ws}_i & \hat{U}^{as}_i \\ \hat{P}^{sw}_j & \hat{P}^{ww} & \hat{P}^{aw} \\ \hat{P}^{sa}_j & \hat{P}^{wa} & \hat{P}^{aa} \end{bmatrix}$$

$$= \frac{\rho_w\rho_a s^2}{G\beta\gamma S_w S_a(K + 4G/3)} \begin{bmatrix} (X_1 - X_2\nabla^2)\delta_{ij} + X_2\partial_{ij} & X_3\partial_i & X_4\partial_i \\ X_5\partial_j & X_7 & X_8 \\ X_6\partial_j & X_9 & X_{10} \end{bmatrix} \Psi \quad , \tag{4.22}$$

where the fundamental solutions consist of nine parts as the displacement and the pore pressure fundamental solutions $\hat{U}^{ss}_{ij}$, $\hat{P}^{ww}$, $\hat{P}^{aa}$, and the six coupling entries.

Inserting the explicit expressions of X_i $(i = 1, ..., 10)$ into (4.22), the nine parts of the fundamental solutions are

$$\hat{U}^{ss}_{ij} = w_0\{[(r_1 - r_5)\nabla^6 + (r_2 - r_6)\nabla^4 + (r_3 - r_7)\nabla^2 + r_4]\delta_{ij} + (r_5\nabla^4 + r_6\nabla^2 + r_7)\partial_{ij}\}\Psi$$
$$\hat{P}^{sw}_j = w_0(r_{14}\nabla^4 + r_{15}\nabla^2 + r_{16})\partial_j\Psi$$

$$\hat{P}_j^{sa} = w_0(r_{17}\nabla^4 + r_{18}\nabla^2 + r_{19})\partial_j\Psi$$

$$\hat{U}_i^{ws} = w_0(r_8\nabla^4 + r_9\nabla^2 + r_{10})\partial_i\Psi$$

$$\hat{P}^{ww} = w_0(r_{20}\nabla^6 + r_{21}\nabla^4 + r_{22}\nabla^2 + r_{23})\Psi$$

$$\hat{P}^{wa} = w_0(r_{27}\nabla^4 + r_{28}\nabla^2 + r_{29})\Psi$$

$$\hat{U}_i^{as} = w_0(r_{11}\nabla^4 + r_{12}\nabla^2 + r_{13})\partial_i\Psi$$

$$\hat{P}^{aw} = w_0(r_{24}\nabla^4 + r_{25}\nabla^2 + r_{26})\Psi$$

$$\hat{P}^{aa} = w_0(r_{30}\nabla^6 + r_{31}\nabla^4 + r_{32}\nabla^2 + r_{33})\Psi \quad ,$$

where $w_0 = \dfrac{\rho_w\rho_a s^2}{G\beta\gamma S_w S_a(K+4G/3)}$.

Applying the operators ∇^2, ∇^4, ∇^6 to the solution of the fourth order Helmholtz equation, respectively, results in

$$\nabla^2\Psi = \frac{1}{4\pi r}\left[\frac{\lambda_1^2 e^{i\lambda_1 r}}{(\lambda_2^2-\lambda_1^2)(\lambda_3^2-\lambda_1^2)(\lambda_4^2-\lambda_1^2)} + \frac{\lambda_2^2 e^{i\lambda_2 r}}{(\lambda_1^2-\lambda_2^2)(\lambda_3^2-\lambda_2^2)(\lambda_4^2-\lambda_2^2)}\right.$$
$$\left. + \frac{\lambda_3^2 e^{i\lambda_3 r}}{(\lambda_1^2-\lambda_3^2)(\lambda_2^2-\lambda_3^2)(\lambda_4^2-\lambda_3^2)} + \frac{\lambda_4^4 e^{i\lambda_4 r}}{(\lambda_1^2-\lambda_4^2)(\lambda_2^2-\lambda_4^2)(\lambda_3^2-\lambda_4^2)}\right] \tag{4.24a}$$

$$\nabla^4\Psi = \frac{1}{4\pi r}\left[\frac{\lambda_1^4 e^{i\lambda_1 r}}{(\lambda_2^2-\lambda_1^2)(\lambda_3^2-\lambda_1^2)(\lambda_4^2-\lambda_1^2)} + \frac{\lambda_2^4 e^{i\lambda_2 r}}{(\lambda_1^2-\lambda_2^2)(\lambda_3^2-\lambda_2^2)(\lambda_4^2-\lambda_2^2)}\right.$$
$$\left. + \frac{\lambda_3^4 e^{i\lambda_3 r}}{(\lambda_1^2-\lambda_3^2)(\lambda_2^2-\lambda_3^2)(\lambda_4^2-\lambda_3^2)} + \frac{\lambda_4^4 e^{i\lambda_4 r}}{(\lambda_1^2-\lambda_4^2)(\lambda_2^2-\lambda_4^2)(\lambda_3^2-\lambda_4^2)}\right] \tag{4.24b}$$

$$\nabla^6\Psi = \frac{1}{4\pi r}\left[\frac{\lambda_1^6 e^{i\lambda_1 r}}{(\lambda_2^2-\lambda_1^2)(\lambda_3^2-\lambda_1^2)(\lambda_4^2-\lambda_1^2)} + \frac{\lambda_2^6 e^{i\lambda_2 r}}{(\lambda_1^2-\lambda_2^2)(\lambda_3^2-\lambda_2^2)(\lambda_4^2-\lambda_2^2)}\right.$$
$$\left. + \frac{\lambda_3^6 e^{i\lambda_3 r}}{(\lambda_1^2-\lambda_3^2)(\lambda_2^2-\lambda_3^2)(\lambda_4^2-\lambda_3^2)} + \frac{\lambda_4^6 e^{i\lambda_4 r}}{(\lambda_1^2-\lambda_4^2)(\lambda_2^2-\lambda_4^2)(\lambda_3^2-\lambda_4^2)}\right] \quad . \tag{4.24c}$$

The displacement fundamental solution $\hat{U}_{ij}^{ss}$ is finally expressed as

$$\hat{U}_{ij}^{ss} = \frac{w_0}{4\pi r^3}\sum_{m=1}^{4} w_m\left[r_{,i}r_{,j}R_m(\lambda_m^2 r^2 + 3\lambda_m r + 3) + \delta_{ij}(S_m r^2 - R_m\lambda_m r - R_m)\right] \quad , \tag{4.25}$$

where

$$w_m = \frac{e^{-\lambda_m r}}{\prod_{j=1,j\neq m}^{4}(\lambda_m^2 - \lambda_j^2)} \quad ,$$

$$R_m = \lambda_m^4 r_5 + \lambda_m^2 r_6 + r_7 \ (m = 1,2,3,4) \quad ,$$

$$S_m = \lambda_m^6 (r_1 - r_5) + \lambda_m^4 (r_2 - r_6) + \lambda_m^2 (r_3 - r_7) + r_4 \ (m = 1,2,3,4) \quad .$$

The pore water pressure fundamental solution $\hat{P}^{ww}$ is expressed as

$$\hat{P}^{ww} = \frac{w_0}{4\pi r} \sum_{m=1}^{4} w_m (\lambda_m^6 r_{20} + \lambda_m^4 r_{21} + \lambda_m^2 r_{22} + r_{23}) \quad , \tag{4.26}$$

and the pore air pressure fundamental solution $\hat{P}^{aa}$

$$\hat{P}^{aa} = \frac{w_0}{4\pi r} \sum_{m=1}^{4} w_m (\lambda_m^6 r_{30} + \lambda_m^4 r_{31} + \lambda_m^2 r_{32} + r_{33}) \quad . \tag{4.27}$$

The explicit expressions of this three dimensional dynamic partially saturated poroelastic fundamental solutions can be found in appendix A.4.

Remark. The derived fundamental solutions for partially saturated poroelasticity are comparable with the solutions by Gatmiri and Jabbari [52]. However, one obvious difference is that the latter ignores the inertial terms of the relative velocities between the fluids and the solid. Besides, the procedure of the derivation is more or less the same as that in Ashayeri et al. [9].

4.4 Visualization of some fundamental solutions

Finally, some exemplary fundamental solutions are calculated to visualize the principle behavior and the difference between the saturated and partially saturated poroelastic model. Both, the frequency domain and time domain results for the proposed fundamental solutions are presented. The displacement due to a point force $\hat{U}_{ij}^{ss}$, and the pressure due to a source $\hat{P}^{ww}$, $\hat{P}^{aa}$ in the three dimensional case are calculated. Massilon Sandstone [86] is chosen for the calculation by using the parameters given in table 3.1. The pore size distribution index ϑ is set to 1.5, the residual water saturation S_{rw} is set to 0, and the air entry saturation S_{ra} is set to 1.

To plot the fundamental solutions, the frequency is used instead of the complex Laplace variable s, by setting the real part of s to zero, i.e., $s = i\omega$. Further, to fix the calculating point $\mathbf{x}$ and loading point $\mathbf{y}$ two sets of parameters are chosen: for $r = 0.5$ with $\mathbf{x} = [0.5,0,0]$ and $\mathbf{y} = [0,0,0]$; for $r = 1.0$ with $\mathbf{x} = [1.0,0,0]$ and $\mathbf{y} = [0,0,0]$. For both cases $r_{,1} = 1$ is set.

In figure 4.1, the absolute displacement fundamental solution abs($\hat{U}_{11}^{ss}$) is plotted versus frequency with varying water saturation for the given observation points at $r = 0.5$ m and
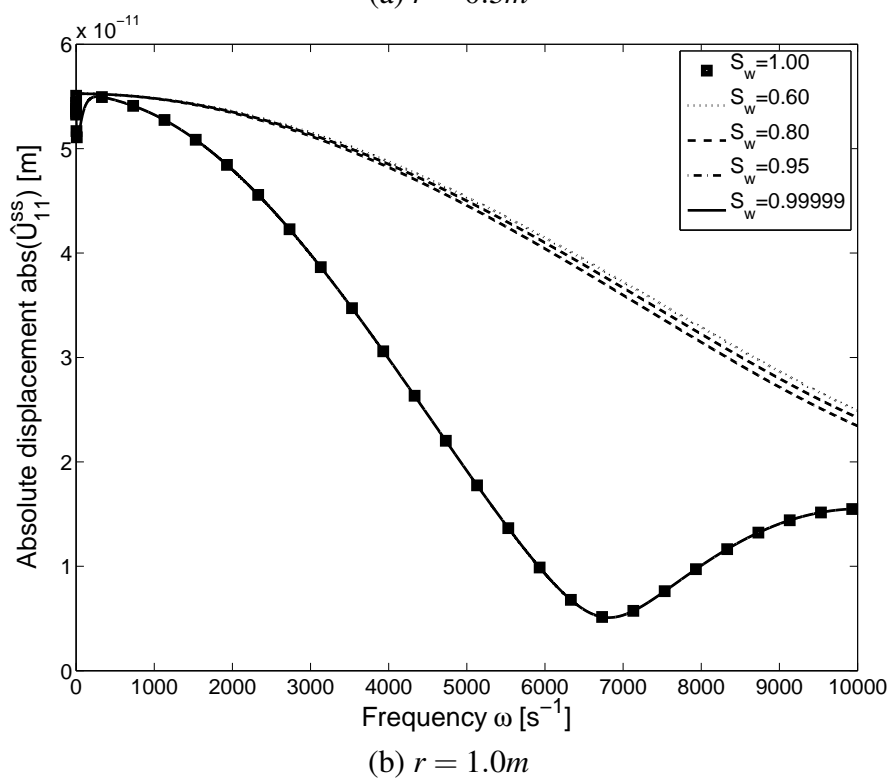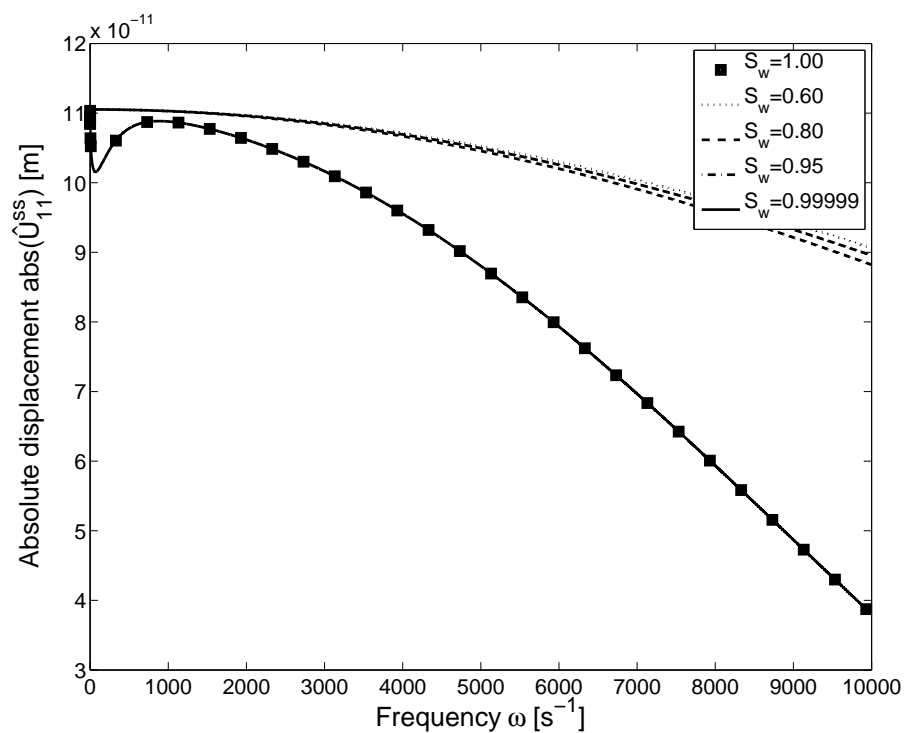
(a) $r = 0.5m$

(b) $r = 1.0m$

Figure 4.1: Absolute displacement fundamental solutions abs($\hat{U}_{11}^{ss}$) versus frequency ω with varying water saturation
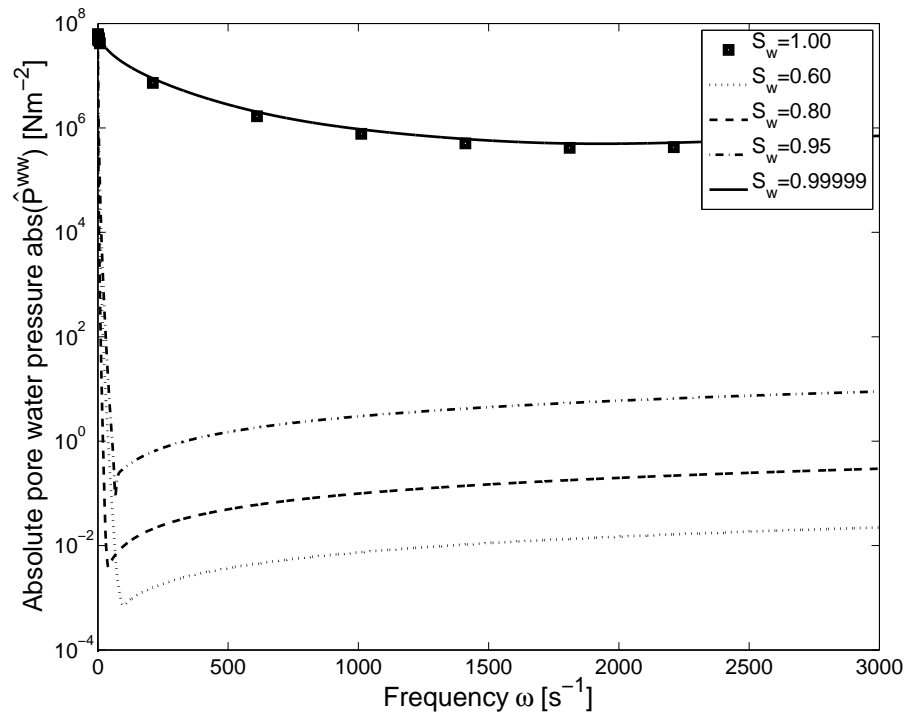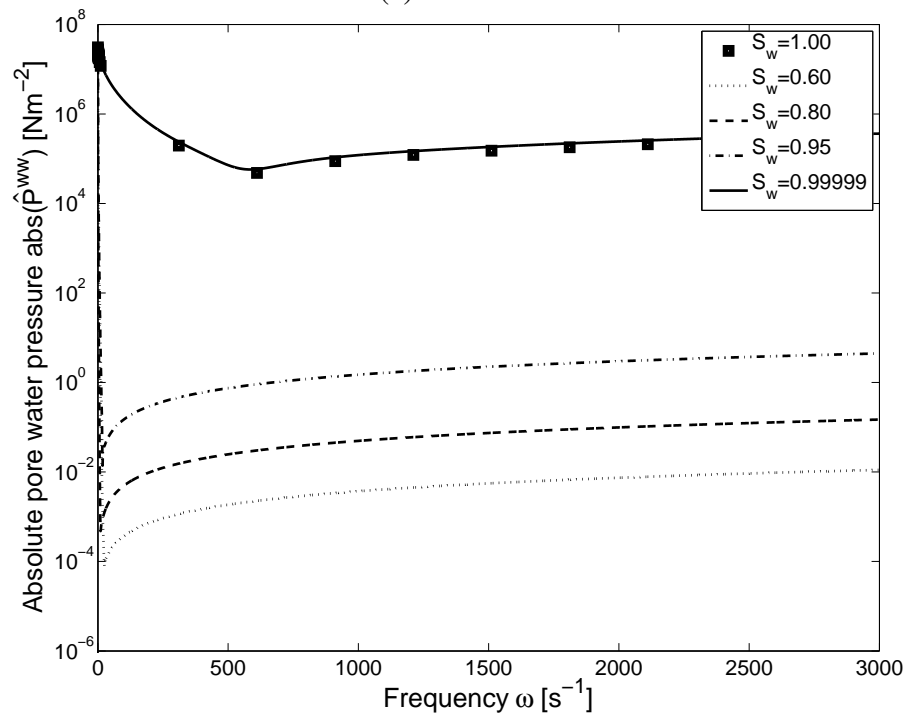
(a) $r = 0.5m$

(b) $r = 1.0m$

Figure 4.2: Absolute pore water pressure fundamental solutions abs($\hat{P}^{ww}$) versus frequency ω with varying water saturation
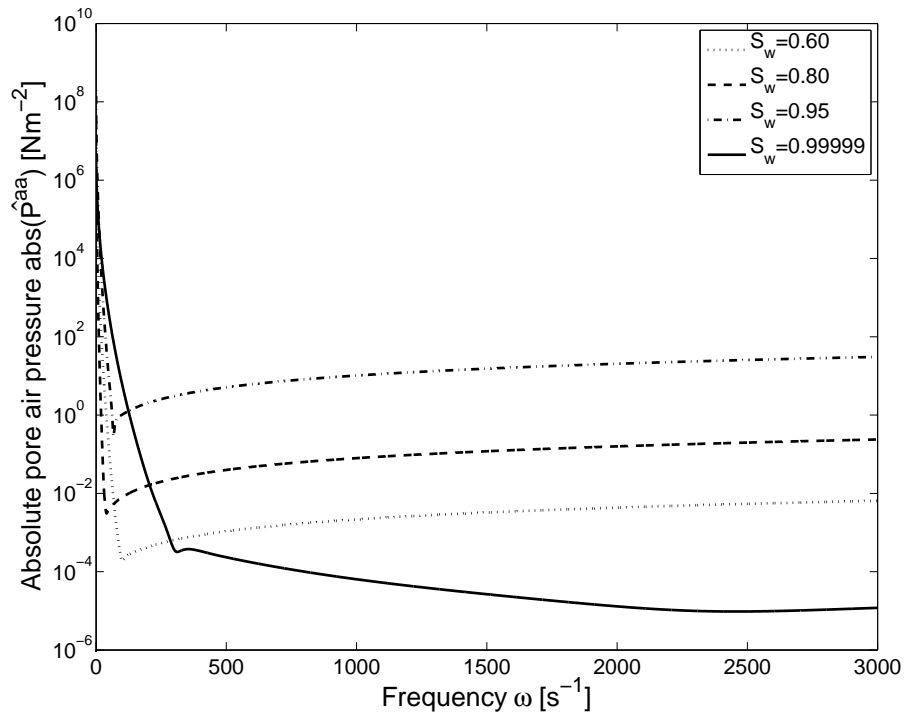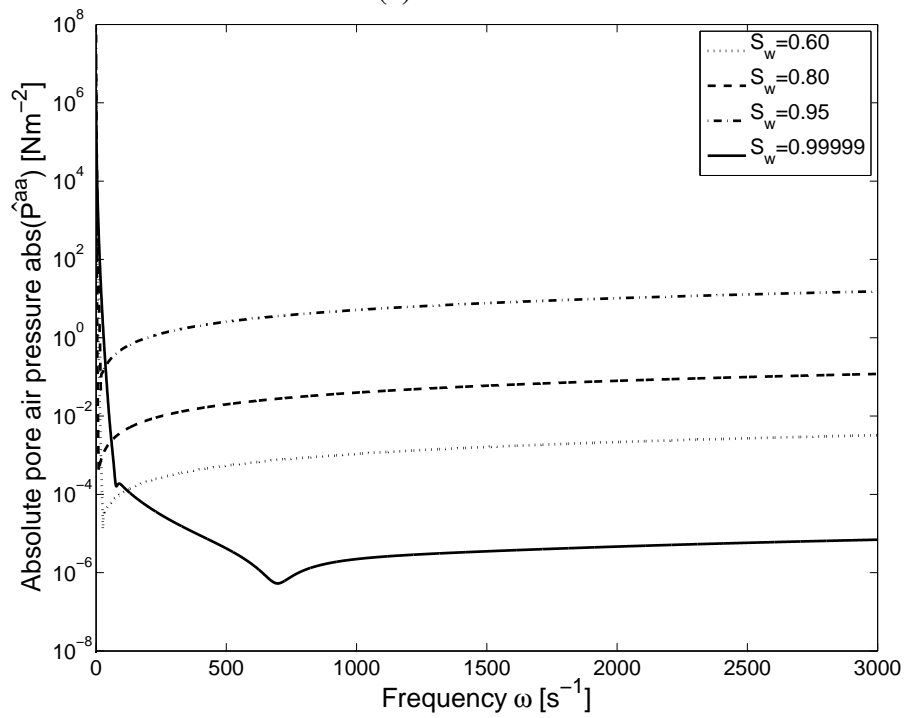
(a) $r = 0.5m$

(b) $r = 1.0m$

Figure 4.3: Absolute pore air pressure fundamental solutions abs($\hat{P}^{aa}$) versus frequency ω with varying water saturation

$r = 1.0$ m. Obviously, the displacement increases with decreasing the water saturation S_w. However, for the whole frequency range calculated, the values of the displacement differ not obviously when the water saturation S_w varies from 0.60 to 0.95. However, when it is nearly saturated, the solution coincides with that of the saturated case [100]. Besides, in the low frequency area there is a jump of the displacement solutions for saturated and nearly saturated cases while this jump can not be observed in partially saturated cases. The displacement difference between the unsaturated case and the saturated / nearly saturated case is somehow small. Oppositely, in the higher frequency area, the displacement difference between the unsaturated case and the saturated / nearly saturated case is quite large.

Next, in figure 4.2 and 4.3, the absolute pore water and pore air pressure due to a source in the fluids are calculated versus frequency with varying water saturation. For the pore water pressure, similar results compared with the displacement solution can be observed. The pore water pressure increases with increasing the water saturation S_w, and for the saturated and nearly saturated cases, the pore water pressure coincide well with each other. For both the pore water and pore air pressure, the values of the partially saturated cases in most of the frequency range are quite small compared with the values of the saturated and nearly saturated cases. However, at very small frequency values which may represent the behavior after a long time period, all the values of the pore pressure tend to the same value. One interesting phenomenon is, for the nearly saturated case, by increasing the water saturation S_w, the pore air pressure of the nearly saturated case becomes much smaller compared to the pressure of the partially saturated cases.

Additionally to the frequency domain results, the time domain results are calculated using the CQM. However, not the impulse response functions are presented but the response due to a Heaviside time history of the load. This is realized by the convolution between the fundamental solution and the Heaviside function.

In figure 4.4 and 4.5, the time dependent displacement and pore pressure responses due to a Heaviside load are depicted versus time for different water saturation S_w at the distance $r = 0.5$ m. For a nearly saturated case such as $S_w = 0.99999$, there are some numerical problems due to this extreme condition, therefore, only the water saturation $S_w = 0.60$, $S_w = 0.80$ and $S_w = 0.95$ are calculated.

For the displacement result in time domain, the jump in the figure 4.4(b) around $t = 0.00043$ s corresponds to the fast compressional wave, however, the assumed jump due to the arrived shear wave is not very obvious. This might be caused by the set of values for $\mathbf{r}$ and r_i. The value of the displacement decreases with increasing the water saturation S_w, and the displacement differences of the three unsaturated cases in time domain are even less obvious compared with those in frequency domain as shown in figure 4.4(a).

Both the pore water and pore air pressure in the time domain are shown in figure 4.5(a) and 4.5(b). Both the pore pressure are mostly zero in the given time period besides the arrival
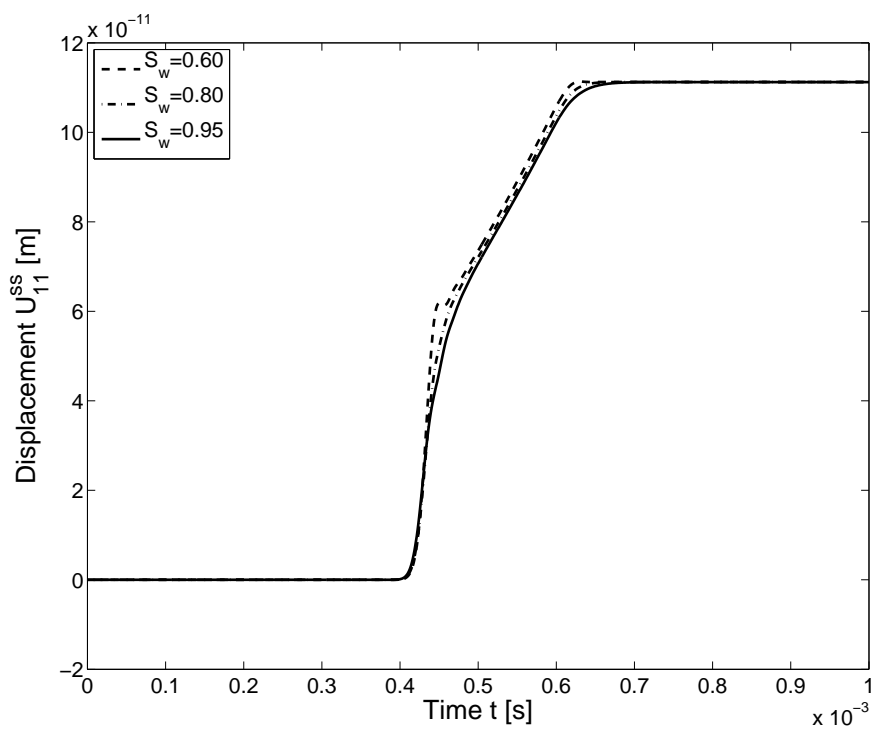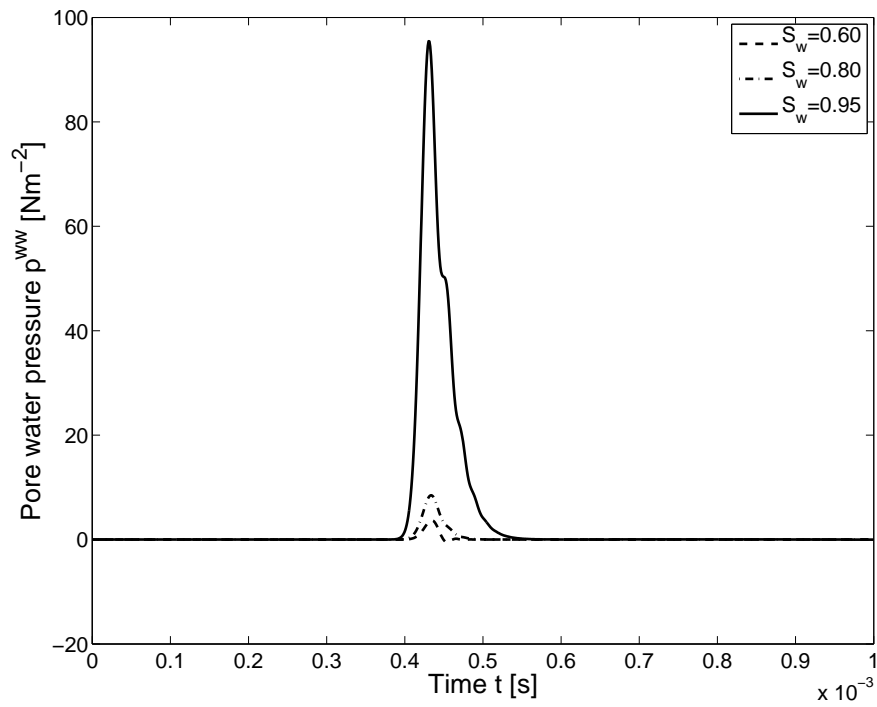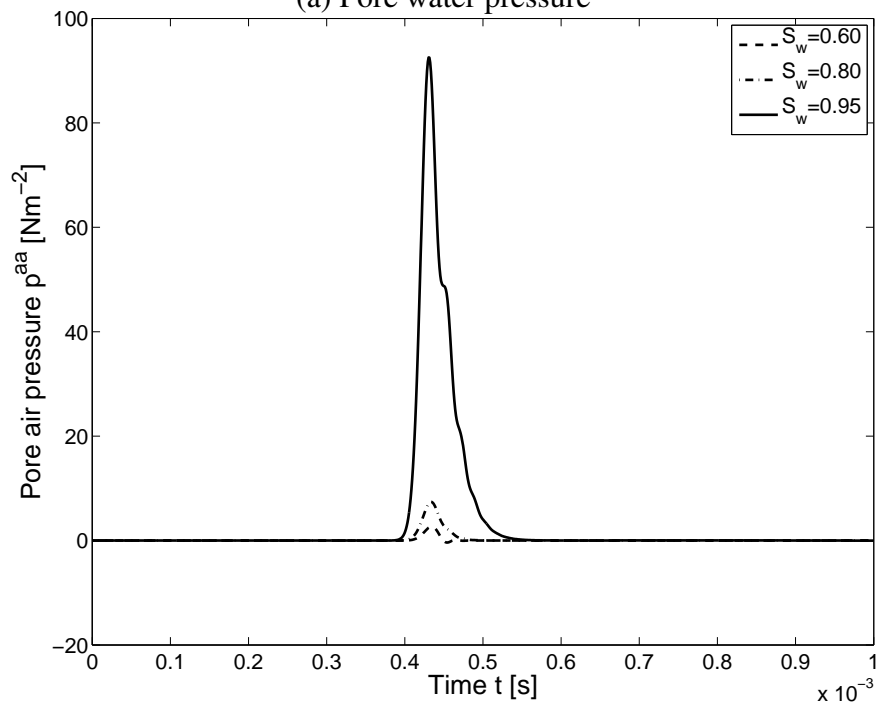
(a) Full scale
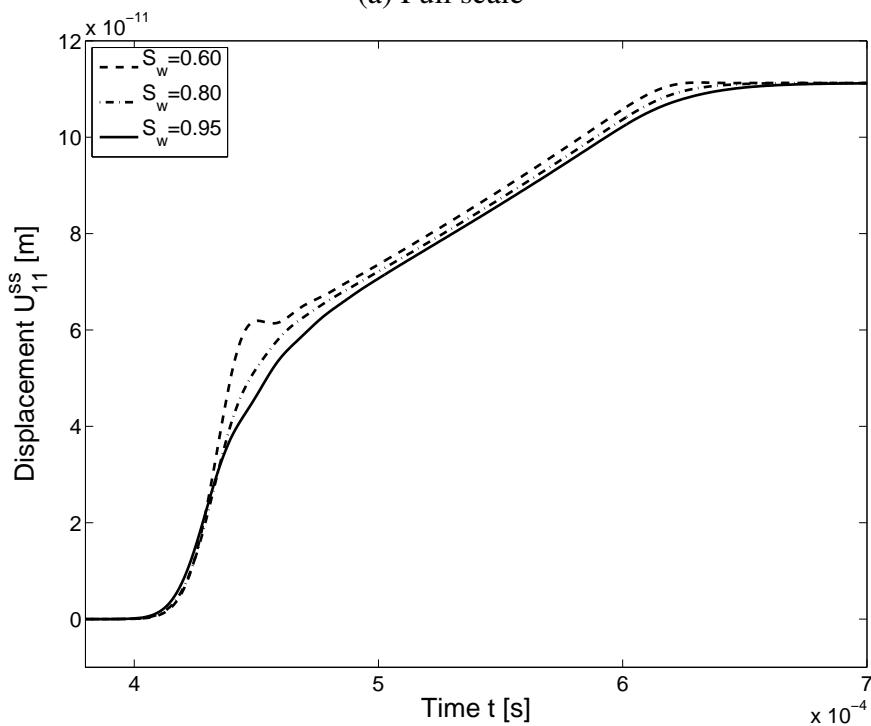
(b) Zoom

Figure 4.4: Displacement U_{11}^{ss} versus time with varying saturation degree at $r = 0.5\,\text{m}$

(a) Pore water pressure

(b) Pore air pressure

Figure 4.5: Pore pressure versus time with varying saturation degree at $r = 0.5\,\mathrm{m}$

of the fast compressional wave. The value of both the pore water and pore air pressure increases with increasing the water saturation S_w.

5 BOUNDARY INTEGRAL EQUATIONS AND BOUNDARY ELEMENT FORMULATION

In this chapter, the boundary integral equations are introduced. For the saturated case, the boundary integral equation can be obtained using either the corresponding reciprocal work theorem [33] or the weighted residuals formulation [44] based on the weighted residuals method [7, 37, 39]. Naturally both methods result, finally, in the same integral equation. Here, the approach with weighted residuals will be used and presented.

The singular integrals in the boundary integral equation require a suitable computing techniques for a precise integral evaluation. For the first integral equation, there exist weakly singular kernels as well as strong singular kernels. For the second boundary integral equation, in addition the evaluation of hyper singular kernel functions is needed. In this work, with a collocation scheme, only the weak and the strong singularities will be faced. A regularization process is done for the strong singularities based on integrating by parts.

For the partially saturated case, in order to achieve stable numerical solutions, dimensionless variables are introduced at last.

5.1 Weighted residuals method

For the case of partially saturated poroelasticity, the differential equations in (2.40) consist of a linear differential operator $\mathcal{B}$ acting on the exact solution $\hat{\mathbf{u}}$, and the corresponding external force and source terms $\hat{\mathbf{f}}$, which is given by

$$\mathcal{B}\,\hat{\mathbf{u}} + \hat{\mathbf{f}} = \mathbf{0} \quad . \tag{5.1}$$

To seek an approximation solution $\tilde{\hat{\mathbf{u}}}$ to the exact solution $\hat{\mathbf{u}}$, an error or so called residual $\mathbf{R}$ will come out. In this case, by inserting the approximation solution $\tilde{\hat{\mathbf{u}}}$ into the differential equations, the residual $\mathbf{R}$ is given by

$$\mathcal{B}\,\tilde{\hat{\mathbf{u}}} + \hat{\mathbf{f}} = \mathbf{R} \quad . \tag{5.2}$$

The residual $\mathbf{R}$ can be minimized by using the method of weighted residuals, i.e., $\mathbf{R}$ is multiplied with a weighting function $\mathbf{W}$. By integrating over the domain, and requiring that the integral vanishes, the weighted average of the residual comes to zero. Following this

method, the differential equations for partially saturated poroelasticity can be transformed to the integral equations

$$\int_\Omega \mathbf{W}^\top (\mathcal{B}\,\tilde{\mathbf{u}} + \hat{\mathbf{f}})\, d\Omega = \mathbf{0} \quad . \tag{5.3}$$

In the following equations of this chapter, $\hat{\mathbf{u}}$ instead of $\tilde{\hat{\mathbf{u}}}$ will be used for the approximated functions for convenience, but one should keep in mind that they are approximate solutions.

Substituting the weighting function $\mathbf{W}$ with the fundamental solutions $\hat{\mathbf{U}}$ (4.22), an integral equation of dynamic partially saturated poroelasticity in the Laplace domain is established and given by

$$\int_\Omega \hat{\mathbf{U}}^\top \mathcal{B}\,\hat{\mathbf{u}}\, d\Omega = \mathbf{0} \quad , \tag{5.4}$$

where the integration is performed over a domain Ω with boundary Γ, and the body force term $\hat{F}_i$, the source terms $\hat{I}^w$ and $\hat{I}^a$ are neglected.

Introducing the explicit expressions of the fundamental solutions $\hat{\mathbf{U}}$ in (4.22), and applying the partial differential operator $\mathcal{B}$ in (2.40), the integral equation (5.4) is expanded in the following forms

$$\int_\Omega (\hat{U}_{ij}^{ss} I_1 + \hat{P}_j^{sw} I_2 + \hat{P}_j^{sa} I_3)\, d\Omega = 0 \tag{5.5a}$$

$$\int_\Omega (\hat{U}_i^{ws} I_1 + \hat{P}^{ww} I_2 + \hat{P}^{wa} I_3)\, d\Omega = 0 \tag{5.5b}$$

$$\int_\Omega (\hat{U}_i^{as} I_1 + \hat{P}^{aw} I_2 + \hat{P}^{aa} I_3)\, d\Omega = 0 \quad , \tag{5.5c}$$

where the explicit expressions of the I_1, I_2 and I_3 are

$$I_1 = G\hat{u}_{i,kk} - (\rho - \beta S_w \rho_w - \gamma S_a \rho_a)s^2 \hat{u}_i + (K + \frac{G}{3})\hat{u}_{k,ik} - (\alpha - \beta)S_w \hat{P}_{,i}^w - (\alpha - \gamma)S_a \hat{P}_{,i}^a \quad ,$$

$$I_2 = -(\alpha - \beta)S_w s \hat{u}_{k,k} - (\zeta S_{ww}S_w + \frac{n}{K_w}S_w - S_u)s\hat{P}^w + \frac{\beta S_w}{\rho_w s}\hat{P}_{,kk}^w - (\zeta S_{aa}S_w + S_u)s\hat{P}^a \quad ,$$

$$I_3 = -(\alpha - \gamma)S_a s \hat{u}_{k,k} - (\zeta S_{ww}S_a + S_u)s\hat{P}^w - (\zeta S_{aa}S_a + \frac{n}{K_a}S_a - S_u)s\hat{P}^a + \frac{\gamma S_a}{\rho_a s}\hat{P}_{,kk}^a \quad .$$

For the integral equations (5.5), either one or two differentiations have to be transformed by either one or two partial integrations. As an example, two exemplary parts of the proposed integral equations (5.5) are presented in detail to show the principal procedure. All

other partial integrations for the other parts in the integral equations can be performed analogously.

First, an integral with one differentiation in the integral equation (5.5b) is transformed by one partial integration

$$
\int_\Omega (\alpha - \beta) S_w s \hat{u}_{k,k} \hat{P}^{ww} d\Omega = \int_\Omega (\alpha - \beta) S_w s (\hat{u}_k \hat{P}^{ww})_{,k} d\Omega - \int_\Omega (\alpha - \beta) S_w s \hat{u}_k \hat{P}^{ww}_{,k} d\Omega
$$

$$
= \int_\Gamma (\alpha - \beta) S_w s \hat{u}_k n_k \hat{P}^{ww} d\Gamma - \int_\Omega (\alpha - \beta) S_w s \hat{u}_k \hat{P}^{ww}_{,k} d\Omega
$$

where n_k is the outward normal vector.

Second, an integral with two differentiation in the integral equation (5.5a) is transformed by two partial integrations

$$
\int_\Omega G \hat{u}_{i,kk} \hat{U}^{ss}_{ij} = \int_\Omega G (\hat{u}_{i,k} \hat{U}^{ss}_{ij})_{,k} d\Omega - \int_\Omega G \hat{u}_{i,k} \hat{U}^{ss}_{ij,k} d\Omega
$$

$$
= \int_\Gamma G \hat{u}_{i,k} n_k \hat{U}^{ss}_{ij} d\Gamma - \int_\Omega G \hat{u}_{i,k} \hat{U}^{ss}_{ij,k} d\Omega
$$

$$
= \int_\Gamma G \hat{u}_{i,k} n_k \hat{U}^{ss}_{ij} d\Gamma - \int_\Omega G (\hat{u}_i \hat{U}^{ss}_{ij,k})_{,k} d\Omega + \int_\Omega G \hat{u}_i \hat{U}^{ss}_{ij,kk} d\Omega
$$

$$
= \int_\Gamma G \hat{u}_{i,k} n_k \hat{U}^{ss}_{ij} d\Gamma - \int_\Gamma G \hat{u}_i \hat{U}^{ss}_{ij,k} n_k d\Gamma + \int_\Omega G \hat{u}_i \hat{U}^{ss}_{ij,kk} d\Omega \quad .
$$

The transformation from the domain to the boundary integral is performed with the divergence theorem. Obviously, one integration by parts changes the sign of the resulting domain integral, while it remains unchanged in the case of two integration by parts, i.e., the differential operator $\mathcal{B}$ is transformed into its ad-joint operator $\mathcal{B}^*$.

This yields the following integral equations given in matrix notation

$$
\int_\Gamma \begin{bmatrix} \hat{U}^{ss}_{ij} & -\hat{P}^{sw}_j & -\hat{P}^{sa}_j \\ \hat{U}^{ws}_i & -\hat{P}^{ww} & -\hat{P}^{wa} \\ \hat{U}^{as}_i & -\hat{P}^{aw} & -\hat{P}^{aa} \end{bmatrix} \begin{bmatrix} \hat{t}_i \\ \hat{q}^w \\ \hat{q}^a \end{bmatrix} d\Gamma - \int_\Gamma \begin{bmatrix} \hat{T}^{ss}_{ij} & \hat{Q}^{sw}_j & \hat{Q}^{sa}_j \\ \hat{T}^{ws}_i & \hat{Q}^{ww} & \hat{Q}^{wa} \\ \hat{T}^{as}_i & \hat{Q}^{aw} & \hat{Q}^{aa} \end{bmatrix} \begin{bmatrix} \hat{u}_i \\ \hat{p}^w \\ \hat{p}^a \end{bmatrix} d\Gamma
$$

$$
= - \int_\Omega (\mathcal{B}^* \hat{U}_{ij}) \begin{bmatrix} \hat{u}_i \\ \hat{p}^w \\ \hat{p}^a \end{bmatrix} d\Omega \quad ,
$$

(5.6)

and based on the equation $\mathcal{B}^* \hat{U}_{ij} + \delta(\mathbf{x}, \mathbf{y}) = 0$, it follows

$$
\int_\Gamma \begin{bmatrix} \hat{U}_{ij}^{ss} & -\hat{P}_j^{sw} & -\hat{P}_j^{sa} \\ \hat{U}_i^{ws} & -\hat{P}^{ww} & -\hat{P}^{wa} \\ \hat{U}_i^{as} & -\hat{P}^{aw} & -\hat{P}^{aa} \end{bmatrix} \begin{bmatrix} \hat{t}_i \\ \hat{q}^w \\ \hat{q}^a \end{bmatrix} d\Gamma - \int_\Gamma \begin{bmatrix} \hat{T}_{ij}^{ss} & \hat{Q}_j^{sw} & \hat{Q}_j^{sa} \\ \hat{T}_i^{ws} & \hat{Q}^{ww} & \hat{Q}^{wa} \\ \hat{T}_i^{as} & \hat{Q}^{aw} & \hat{Q}^{aa} \end{bmatrix} \begin{bmatrix} \hat{u}_i \\ \hat{p}^w \\ \hat{p}^a \end{bmatrix} d\Gamma = \begin{bmatrix} \hat{u}_j \\ \hat{p}^w \\ \hat{p}^a \end{bmatrix}
$$
(5.7)

which is the so called representation formula.

The representation formula (5.7) can be used to calculate the unknown values of the displacement $\hat{u}_j$, the pore water pressure $\hat{p}^w$, and the pore air pressure $\hat{p}^a$ inside the domain when the boundary solution of a given problem is known.

Additionally, the traction vector and the flux

$$
\hat{t}_i = \hat{\sigma}_{ij} n_j
$$
(5.8a)

$$
\hat{q}^w = -\frac{\beta}{\rho_w s} (\hat{p}_{,i}^w + \rho_w s^2 \hat{u}_i) n_i
$$
(5.8b)

$$
\hat{q}^a = -\frac{\gamma}{\rho_a s} (\hat{p}_{,i}^a + \rho_a s^2 \hat{u}_i) n_i
$$
(5.8c)

are introduced.

The abbreviations of the traction and flux fundamental solutions are

$$
\hat{T}_{ij}^{ss} = \left\{ [(K - \frac{2}{3}G)\hat{U}_{kj,k}^{ss} + \alpha s(S_w \hat{P}_j^{sw} + S_a \hat{P}_j^{sa})]\delta_{il} + G(\hat{U}_{ij,l}^{ss} + \hat{U}_{lj,i}^{ss}) \right\} n_l
$$
(5.9a)

$$
\hat{T}_i^{ws} = \left\{ [(K - \frac{2}{3}G)\hat{U}_{k,k}^{ws} + \alpha s(S_w \hat{P}^{ww} + S_a \hat{P}^{wa})]\delta_{il} + G(\hat{U}_{i,l}^{ws} + \hat{U}_{l,i}^{ws}) \right\} n_l
$$
(5.9b)

$$
\hat{T}_i^{as} = \left\{ [(K - \frac{2}{3}G)\hat{U}_{k,k}^{as} + \alpha s(S_w \hat{P}^{aw} + S_a \hat{P}^{aa})]\delta_{il} + G(\hat{U}_{i,l}^{as} + \hat{U}_{l,i}^{as}) \right\} n_l
$$
(5.9c)

$$
\hat{Q}_j^{sw} = \frac{\beta S_w}{\rho_w s} (\hat{P}_{j,i}^{sw} - \rho_w s \hat{U}_{ji}^{ss}) n_i
$$
(5.9d)

$$
\hat{Q}^{ww} = \frac{\beta S_w}{\rho_w s} (\hat{P}_{,j}^{ww} - \rho_w s \hat{U}_j^{ws}) n_j
$$
(5.9e)

$$
\hat{Q}^{aw} = \frac{\beta S_w}{\rho_w s} (\hat{P}_{,j}^{aw} - \rho_w s \hat{U}_j^{as}) n_j
$$
(5.9f)

$$
\hat{Q}_j^{sa} = \frac{\gamma S_a}{\rho_a s} (\hat{P}_{j,i}^{sa} - \rho_a s \hat{U}_{ji}^{ss}) n_i
$$
(5.9g)

$$
\hat{Q}^{wa} = \frac{\gamma S_a}{\rho_a s} (\hat{P}_{,j}^{wa} - \rho_a s \hat{U}_j^{ws}) n_j
$$
(5.9h)

$$
\hat{Q}^{aa} = \frac{\gamma S_a}{\rho_a s} (\hat{P}_{,j}^{aa} - \rho_a s \hat{U}_j^{as}) n_j \quad ,
$$
(5.9i)

and their explicit expressions can be found in appendix A.4.

As presented in (5.7), the values of the unknowns inside the domain can be caluclated when the boundary solution is known. However, to determine the unknown boundary data, the load point **y** has to be moved to the boundary, and the resulting equation is named as the boundary integral equation which forms the basis of the subsequent boundary element method.

5.2 Boundary integral equations

Moving the negative sign in the single layer operator to the flux in the representation formula (5.7) results in

$$\hat{\mathbf{u}}(\mathbf{y}) = (\hat{\mathcal{V}}\hat{\mathbf{t}})(\mathbf{y}) - (\hat{\mathcal{K}}\hat{\mathbf{u}})(\mathbf{y}) \quad (\mathbf{y} \in \Omega) \tag{5.10}$$

with $\hat{\mathbf{u}}(\mathbf{x}) = [\hat{u}_i, \hat{p}^w, \hat{p}^a]$, and $\hat{\mathbf{t}}(\mathbf{x}) = [\hat{t}_i, -\hat{q}^w, -\hat{q}^a]^\top$.

The definitions of the single layer operator $\hat{\mathcal{V}}$ and the double layer operator $\hat{\mathcal{K}}$ are given by

$$(\hat{\mathcal{V}}\hat{\mathbf{t}})(\mathbf{y}) = \int_\Gamma \hat{\mathbf{U}}^\top(\mathbf{y},\mathbf{x})\hat{\mathbf{t}}(\mathbf{x})ds_{\mathbf{x}} \tag{5.11a}$$

$$(\hat{\mathcal{K}}\hat{\mathbf{u}})(\mathbf{y}) = \int_\Gamma \hat{\mathbf{T}}^\top(\mathbf{y},\mathbf{x})\hat{\mathbf{u}}(\mathbf{x})ds_{\mathbf{x}} \quad, \tag{5.11b}$$

where

$$\hat{\mathbf{U}}^\top = \begin{bmatrix} \hat{U}_{ij}^{ss} & \hat{P}_j^{sw} & \hat{P}_j^{sa} \\ \hat{U}_i^{ws} & \hat{P}^{ww} & \hat{P}^{wa} \\ \hat{U}_i^{as} & \hat{P}^{aw} & \hat{P}^{aa} \end{bmatrix} \quad, \quad \hat{\mathbf{T}}^\top = \begin{bmatrix} \hat{T}_{ij}^{ss} & \hat{Q}_j^{sw} & \hat{Q}_j^{sa} \\ \hat{T}_i^{ws} & \hat{Q}^{ww} & \hat{Q}^{wa} \\ \hat{T}_i^{as} & \hat{Q}^{aw} & \hat{Q}^{aa} \end{bmatrix} \quad.$$

To move the load point **y** to the boundary, the original boundary Γ is modified to be $\tilde{\Gamma}$ by extending it with a small circular region of radius r_c around the load point $\tilde{\mathbf{y}} \in \Omega$ as shown in figure 5.1.
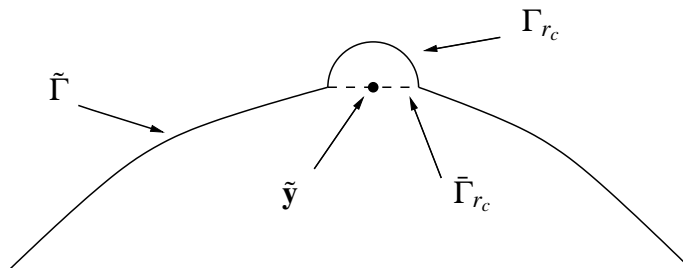
Figure 5.1: Boundary extension around the load point $\tilde{\mathbf{y}}$

The extended boundary $\tilde{\Gamma}$ is then given by

$$\tilde{\Gamma} = \Gamma - \bar{\Gamma}_{r_c} + \Gamma_{r_c} \quad, \tag{5.12}$$

where $\Gamma = \lim\limits_{r_c \to 0} \tilde{\Gamma}$.

After this process, the load point $\tilde{\mathbf{y}}$ is inside the domain again, and the representation formula (5.7) remains valid,

$$\hat{\mathbf{u}}(\tilde{\mathbf{y}}) = (\hat{\mathcal{V}}\hat{\mathbf{t}})(\tilde{\mathbf{y}}) - (\hat{\mathcal{K}}\hat{\mathbf{u}})(\tilde{\mathbf{y}}) \quad (\tilde{\mathbf{y}} \in \Omega) \quad. \tag{5.13}$$

Now applying the limiting process $r_c \to 0$, the representation formula turns to the boundary integral equation, which is expressed as

$$(\hat{\mathcal{V}}\hat{\mathbf{t}})(\mathbf{y}) - (\hat{\mathcal{K}}\hat{\mathbf{u}})(\mathbf{y}) = \mathcal{C}(\mathbf{y})\hat{\mathbf{u}}(\mathbf{y}) \tag{5.14}$$

where

$$\lim_{r_c \to 0} \int_{\tilde{\Gamma}} \hat{\mathbf{U}}^\top(\mathbf{y},\mathbf{x})\hat{\mathbf{t}}(\mathbf{x})d\Gamma = \lim_{r_c \to 0} \int_{\Gamma - \bar{\Gamma}_{r_c}} \hat{\mathbf{U}}^\top(\mathbf{y},\mathbf{x})\hat{\mathbf{t}}(\mathbf{x})d\Gamma + \lim_{r_c \to 0} \int_{\Gamma_{r_c}} \hat{\mathbf{U}}^\top(\mathbf{y},\mathbf{x})\hat{\mathbf{t}}(\mathbf{x})d\Gamma$$

$$= \lim_{r_c \to 0} \int_{\Gamma - \bar{\Gamma}_{r_c}} \hat{\mathbf{U}}^\top(\mathbf{y},\mathbf{x})\hat{\mathbf{t}}(\mathbf{x})d\Gamma \tag{5.15a}$$

$$= (\hat{\mathcal{V}}\hat{\mathbf{t}})(\mathbf{y}) \quad,$$

$$\lim_{r_c \to 0} \int_{\tilde{\Gamma}} \hat{\mathbf{T}}^\top(\mathbf{y},\mathbf{x})\hat{\mathbf{u}}(\mathbf{x})d\Gamma = \lim_{r_c \to 0} \int_{\Gamma - \bar{\Gamma}_{r_c}} \hat{\mathbf{T}}^\top(\mathbf{y},\mathbf{x})\hat{\mathbf{u}}(\mathbf{x})d\Gamma + \lim_{r_c \to 0} \int_{\Gamma_{r_c}} \hat{\mathbf{T}}^\top(\mathbf{y},\mathbf{x})\hat{\mathbf{u}}(\mathbf{x})d\Gamma \tag{5.15b}$$

$$= (\hat{\mathcal{K}}\hat{\mathbf{u}})(\mathbf{y}) + [\mathcal{C}(\mathbf{y}) - \mathbf{I}]\hat{\mathbf{u}}(\mathbf{y})] \quad.$$

The factor matrix $\mathcal{C}(\mathbf{y})$ is the free term coefficient and can be interpreted as the fraction of $\hat{\mathbf{u}}(\mathbf{y})$ that lies inside the domain Ω, and is given by

$$\mathcal{C}(\mathbf{y}) = \begin{cases} \lim\limits_{r_c \to 0} \int_{\Gamma_{r_c}} \hat{\mathbf{T}}^\top(\mathbf{y},\mathbf{x})\hat{\mathbf{u}}(\mathbf{x})d\Gamma + \mathbf{I} & (\mathbf{y} \in \Gamma) \\[2mm] \mathbf{I} & (\mathbf{y} \in \Omega) \\[1mm] \mathbf{0} & (\mathbf{y} \notin \Gamma, \, \mathbf{y} \notin \Omega) \end{cases} \quad. \tag{5.16}$$

Finally, the explicit expressions of the boundary integral equations are given by

$$\int_{\Gamma} \begin{bmatrix} \hat{U}_{ij}^{ss} & \hat{P}_j^{sw} & \hat{P}_j^{sa} \\ \hat{U}_i^{ws} & \hat{P}^{ww} & \hat{P}^{wa} \\ \hat{U}_i^{as} & \hat{P}^{aw} & \hat{P}^{aa} \end{bmatrix} \begin{bmatrix} \hat{t}_i \\ -\hat{q}^w \\ -\hat{q}^a \end{bmatrix} d\Gamma - \oint_{\Gamma} \begin{bmatrix} \hat{T}_{ij}^{ss} & \hat{Q}_j^{sw} & \hat{Q}_j^{sa} \\ \hat{T}_i^{ws} & \hat{Q}^{ww} & \hat{Q}^{wa} \\ \hat{T}_i^{as} & \hat{Q}^{aw} & \hat{Q}^{aa} \end{bmatrix} \begin{bmatrix} \hat{u}_i \\ \hat{p}^w \\ \hat{p}^a \end{bmatrix} d\Gamma$$

$$= \begin{bmatrix} c_{ij} & 0 & 0 \\ 0 & c & 0 \\ 0 & 0 & c \end{bmatrix} \begin{bmatrix} \hat{u}_i \\ \hat{p}^w \\ \hat{p}^a \end{bmatrix} \quad, \tag{5.17}$$

where the strong singular integral exists in the sense of a Cauchy Principal Value in the entry $\hat{T}_{ij}^{ss}$ (the singular behavior will be discussed in the next section). For this, the symbol $\oint$ is used.

Next, the time dependent boundary integral equations are obtained by a formal inverse Laplace transformation

$$\int\limits_0^t \int\limits_\Gamma \begin{bmatrix} U_{ij}^{ss}(t-\tau,\mathbf{y},\mathbf{x}) & P_j^{sw}(t-\tau,\mathbf{y},\mathbf{x}) & P_j^{sa}(t-\tau,\mathbf{y},\mathbf{x}) \\ U_i^{ws}(t-\tau,\mathbf{y},\mathbf{x}) & P^{ww}(t-\tau,\mathbf{y},\mathbf{x}) & P^{wa}(t-\tau,\mathbf{y},\mathbf{x}) \\ U_i^{as}(t-\tau,\mathbf{y},\mathbf{x}) & P^{aw}(t-\tau,\mathbf{y},\mathbf{x}) & P^{aa}(t-\tau,\mathbf{y},\mathbf{x}) \end{bmatrix} \begin{bmatrix} t_i(\tau,\mathbf{x}) \\ -q^w(\tau,\mathbf{x}) \\ -q^a(\tau,\mathbf{x}) \end{bmatrix} d\Gamma d\tau$$

$$-\int\limits_0^t \oint\limits_\Gamma \begin{bmatrix} T_{ij}^{ss}(t-\tau,\mathbf{y},\mathbf{x}) & Q_j^{sw}(t-\tau,\mathbf{y},\mathbf{x}) & Q_j^{sa}(t-\tau,\mathbf{y},\mathbf{x}) \\ T_i^{ws}(t-\tau,\mathbf{y},\mathbf{x}) & Q^{ww}(t-\tau,\mathbf{y},\mathbf{x}) & Q^{wa}(t-\tau,\mathbf{y},\mathbf{x}) \\ T_i^{as}(t-\tau,\mathbf{y},\mathbf{x}) & Q^{aw}(t-\tau,\mathbf{y},\mathbf{x}) & Q^{aa}(t-\tau,\mathbf{y},\mathbf{x}) \end{bmatrix} \begin{bmatrix} u_i(\tau,\mathbf{x}) \\ p^w(\tau,\mathbf{x}) \\ p^a(\tau,\mathbf{x}) \end{bmatrix} d\Gamma d\tau \quad (5.18)$$

$$= \begin{bmatrix} c_{ij}(\mathbf{y}) & 0 & 0 \\ 0 & c(\mathbf{y}) & 0 \\ 0 & 0 & c(\mathbf{y}) \end{bmatrix} \begin{bmatrix} u_i(t,\mathbf{y}) \\ p^w(t,\mathbf{y}) \\ p^a(t,\mathbf{y}) \end{bmatrix} .$$

In equation (5.18), the strong singularity exists in the double layer operator and the corresponding regularization process is discussed in the following section.

5.3 Regularization of the double layer operator

In the direct boundary element method, two types of singularities, a weak and a strong singularity are usually encountered. For the weak singularity, it is not sufficient to just use the standard Gaussian quadrature. In the presented approach, a Duffy transformation [108] is performed. In this section, only the regularization of the strong singularity is to be discussed. First of all, the singular behavior of the fundamental solutions has to be investigated.

5.3.1 Singular behavior of the fundamental solutions

The definition of the weak and strong singularities in the direct boundary element method is shown in table 5.1. When moving the load point $\mathbf{y}$ to the boundary Γ to determine the unknown boundary data, it is necessary to know the behavior of the fundamental solutions when $r = |\mathbf{y} - \mathbf{x}|$ tends to zero, i.e., when an integration point $\mathbf{x}$ approaches a collocation point $\mathbf{y}$.

The order of the singularity of the fundamental solutions can be determined by a series expansion with respect to the variable r. This variable is found in these solutions in the exponential function in the three dimensional solutions. Else, only powers of r appear.

Table 5.1: Definition of the singularities in the direct boundary element method

Type	Property	2–D	3–D
weak singularity	inproper integral	$\ln r$	$\dfrac{1}{r}$
strong singularity	Cauchy Principal Value	$\dfrac{1}{r}$	$\dfrac{1}{r^2}$

Therefore, it is sufficient to insert in the fundamental solutions the following series expansion

$$e^{-\lambda_i r} = \sum_{k=0}^{\infty} \frac{(-\lambda_i r)^k}{k!} = 1 - \lambda_i r + \frac{\lambda_i^2 r^2}{2} + \cdots \tag{5.19}$$

to investigate the singular behavior of both the single layer and the double layer operators.

For the single layer operator, by inserting the series expansion, it follows

$$\hat{U}_i^{ws} = \mathcal{O}(r)$$
$$\hat{U}_i^{as} = \mathcal{O}(r)$$
$$\hat{P}_j^{sw} = \mathcal{O}(r)$$
$$\hat{P}_j^{sa} = \mathcal{O}(r)$$
$$\hat{P}^{wa} = \mathcal{O}(r)$$
$$\hat{P}^{aw} = \mathcal{O}(r)$$
$$\hat{U}_{ij}^{ss} = \frac{G+3K}{8\pi G(3K+4G)} \left(r_{,i} r_{,j} + \frac{7G+3K}{G+3K} \delta_{ij} \right) \frac{1}{r} + \mathcal{O}(r)$$
$$= \underbrace{\frac{1+\nu}{8\pi E(1-\nu)} \left[r_{,i} r_{,j} + (3-4\nu)\delta_{ij} \right] \frac{1}{r}}_{\text{elastostatic fundamental solution } \hat{U}_{\text{static}}^{ss}} + \mathcal{O}(r)$$
$$\hat{P}^{ww} = \underbrace{\frac{\rho_w s}{4\pi\beta} \frac{1}{S_w} \frac{1}{r}}_{\hat{p}_{sing}^{ww}} + \mathcal{O}(r)$$
$$\hat{P}^{aa} = \underbrace{\frac{\rho_a s}{4\pi\gamma} \frac{1}{S_a} \frac{1}{r}}_{\hat{p}_{sing}^{aa}} + \mathcal{O}(r) \quad,$$

where E is Young's modulus, and ν is Poisson's ratio.

For the double layer operator, by inserting the series expansion, it follows

$$\hat{Q}^{wa} = \mathcal{O}(r)$$

$$\hat{Q}^{aw} = \mathcal{O}(r)$$

$$\hat{T}_i^{ws} = \frac{[3\beta K + G(3\alpha + \beta)]\rho_w s^2}{12\pi\beta(K + 4G/3)}\frac{n_i}{r} + \frac{G(\alpha - \beta)\rho_w s^2}{4\pi\beta(K + 4G/3)}\frac{r_{,i}r_{,n}}{r} + \mathcal{O}(r)$$

$$= \frac{\rho_w s^2}{8\pi\beta(1 - \nu)r}\{[\alpha(1 - 2\nu) + \beta]n_i + (\alpha - \beta)(1 - 2\nu)r_{,i}r_{,n}\} + \mathcal{O}(r)$$

$$\hat{T}_i^{as} = \frac{[3\gamma K + G(3\alpha + \gamma)]\rho_a s^2}{12\pi\gamma(K + 4G/3)}\frac{n_i}{r} + \frac{G(\alpha - \gamma)\rho_a s^2}{4\pi\gamma(K + 4G/3)}\frac{r_{,i}r_{,n}}{r} + \mathcal{O}(r)$$

$$= \frac{\rho_a s^2}{8\pi\gamma(1 - \nu)r}\{[\alpha(1 - 2\nu) + \gamma]n_i + (\alpha - \gamma)(1 - 2\nu)r_{,i}r_{,n}\} + \mathcal{O}(r)$$

$$\hat{Q}_j^{sw} = \frac{S_w}{8\pi G(4G + 3K)r}\{[3\alpha G - \beta(4G + 3K)]r_{,j}r_{,n} - [3\alpha G + \beta(4G + 3K)]n_{,j}\} + \mathcal{O}(r)$$

$$= \frac{S_w(1 + \nu)}{8\pi E(1 - \nu)r}[\alpha(1 - 2\nu)(r_{,j}r_{,n} - n_j) - 2\beta(1 - \nu)(r_{,j}r_{,n} + n_j)] + \mathcal{O}(r)$$

$$\hat{Q}_j^{sa} = \frac{S_a}{8\pi G(4G + 3K)r}\{[3\alpha G - \gamma(4G + 3K)]r_{,j}r_{,n} - [3\alpha G + \gamma(4G + 3K)]n_{,j}\} + \mathcal{O}(r)$$

$$= \frac{S_a(1 + \nu)}{8\pi E(1 - \nu)r}[\alpha(1 - 2\nu)(r_{,j}r_{,n} - n_j) - 2\gamma(1 - \nu)(r_{,j}r_{,n} + n_j)] + \mathcal{O}(r)$$

$$\hat{T}_{ij}^{ss} = \frac{1}{4\pi(K + 4G/3)r^2}\left[G(r_{,j}n_i - r_{,i}n_j - \delta_{ij}r_{,n}) - (G + 3K)r_{,i}r_{,j}r_{,n}\right] + \mathcal{O}(r)$$

$$= \underbrace{\frac{1}{8\pi(1 - \nu)r^2}\{(1 - 2\nu)(r_{,j}n_i - r_{,i}n_j) - [(1 - 2\nu)\delta_{ij} + 3r_{,i}r_{,j}]r_{,n}\}}_{\text{elastostatic fundamental solution } \hat{T}} + \mathcal{O}(r)$$

$$\hat{Q}^{ww} = \underbrace{-\frac{r_{,n}}{4\pi r^2}}_{\text{acoustic fundamental solution } \hat{Q}} + \mathcal{O}(r)$$

$$\hat{Q}^{aa} = \underbrace{-\frac{r_{,n}}{4\pi r^2}}_{\text{acoustic fundamental solution } \hat{Q}} + \mathcal{O}(r) \quad .$$

It is obvious that weak and strong singularities exist in both the single layer and the double layer operators. For the single layer operator, the entries $\hat{U}_{ij}^{ss}$, $\hat{P}^{ww}$, and $\hat{P}^{aa}$ show a weak singularity while the other entries are all regular. For the double layer operator, the entry $\hat{T}_{ij}^{ss}$ shows a strong singularity while the other entries all show a weak singularity. Contrary to $\hat{T}_{ij}^{ss}$, note that the application of the normal derivative onto $\hat{P}^{ww}$ and $\hat{P}^{aa}$, does not lead to a strong singularity for smooth enough surfaces. Besides, the strong singular parts in the kernel functions are known from the elastostatics.

For the regular integrals, they can be calculated by using Gaussian quadrature by taking the product of one dimensional quadrature formulae. For the weak singular integrals, no special treatment is needed for the case of an analytical evaluation, while for a numerical integration over a weakly singular integral, Duffy transformation is employed for which the Jacobian determinant vanishes at the point of singularity. For the strong singular integrals, a number of methods have been developed. In this work, the technique used to regularize the strong singular integrals is as same as used in [65], which itself is based on [60]. The method is to integrate the double layer operator by parts, which leads to a kernel function with higher regularity before the limiting process of moving the load point **y** to the boundary is performed.

5.3.2 Regularization of Cauchy Principal Value integral

Introducing the elastostatic stress operator $\hat{\mathcal{T}}^e$ [69], the double layer operator can be expressed as

$$
\hat{\mathcal{K}} = \begin{bmatrix} \hat{T}^{ss}_{ij} & \hat{Q}^{sw}_j & \hat{Q}^{sa}_j \\ \hat{T}^{ws}_i & \hat{Q}^{ww} & \hat{Q}^{wa} \\ \hat{T}^{as}_i & \hat{Q}^{aw} & \hat{Q}^{aa} \end{bmatrix}
$$

$$
= \begin{bmatrix} \hat{\mathcal{T}}^e & s\alpha S_w n_i & s\alpha S_a n_i \\ -\beta S_w n_j & \dfrac{\beta S_w}{\rho_w s}\nabla n_j & 0 \\ -\gamma S_a n_j & 0 & \dfrac{\gamma S_a}{\rho_a s}\nabla n_j \end{bmatrix} \begin{bmatrix} \hat{U}^{ss}_{ij} & \hat{U}^{ws}_i & \hat{U}^{as}_i \\ \hat{P}^{sw}_j & \hat{P}^{ww} & \hat{P}^{aw} \\ \hat{P}^{sa}_j & \hat{P}^{wa} & \hat{P}^{aa} \end{bmatrix} , \tag{5.22}
$$

where

$$
\mathcal{T}^e() = (\lambda + 2\mu)(\nabla \cdot ())\mathbf{n} - \mu(\mathbf{n} \times (\nabla \times ())) + 2\mu\mathcal{M} \cdot () \quad . \tag{5.23}
$$

Here, $\mathcal{M}$ denotes the Günter derivative [59], and is given by

$$
\mathcal{M}_{ij} = \sum_j \varepsilon_{jik} S_k = \begin{bmatrix} 0 & -S_3 & S_2 \\ S_3 & 0 & -S_1 \\ -S_2 & S_1 & 0 \end{bmatrix} = n_j\frac{\partial}{\partial x_i} - n_i\frac{\partial}{\partial x_j} \quad , \tag{5.24}
$$

where ε_{jik} denotes the permutation symbol, and S_k $(k = 1, 2, 3)$ is the surface curl lying in the tangential plane of the boundary Γ, see [65].

It is obvious that the strong singular behavior of the traction fundamental solutions comes from the the application of the stress operator $\mathcal{T}^e$ onto the displacement fundamental solution

$$
\hat{\mathbf{T}}^{ss} = \hat{\mathcal{T}}^e\hat{\mathbf{U}}^{ss} + s\alpha(S_w\hat{\mathbf{P}}^{sw\top} + S_a\hat{\mathbf{P}}^{sa}\mathbf{n}^\top) \quad . \tag{5.25}
$$

The first step is to decompose the displacement fundamental solution $\hat{\mathbf{U}}^{ss}$ into a singular part $\hat{\mathbf{U}}_{sing}$ and a regular part $\hat{\mathbf{U}}_{reg}$:

$$\hat{\mathbf{U}}^{ss} = \hat{\mathbf{U}}_{sin} + \hat{\mathbf{U}}_{reg} \quad , \tag{5.26}$$

where

$$\hat{\mathbf{U}}_{sin} = \frac{1}{G}\left(\nabla^2\mathbf{I} - \frac{3K+G}{3K+4G}\nabla\nabla^\top\right)\nabla^4\Psi \tag{5.27a}$$

$$\begin{aligned}\hat{\mathbf{U}}_{reg} = &-\frac{1}{G}\left[(\lambda_1^2+\lambda_2^2+\lambda_3^2)\nabla^4 - (\lambda_1^2\lambda_2^2+\lambda_1^2\lambda_3^2+\lambda_2^2\lambda_3^2)\nabla^2 + \lambda_1^2\lambda_2^2\lambda_3^2\right]\mathbf{I}\Psi \\ &+ w_0(r_6\nabla^2 + r_7)\nabla\nabla^\top\Psi\end{aligned} \tag{5.27b}$$

where Ψ is the solution of the fourth order Helmholtz equation. w_0, r_6 and r_7 can be found in appendix A.4.

Next, writing $\hat{\mathbf{T}}^{ss}$ out in more detail together with the before introduced decomposition (5.27), results in the following representation of the solid related double layer kernel

$$\begin{aligned}\hat{\mathbf{T}}^{ss} &= \hat{\mathcal{T}}^e(\hat{\mathbf{U}}_{sin} + \hat{\mathbf{U}}_{reg}) + \alpha s(S_w\hat{\mathbf{P}}^{sw} + S_a\hat{\mathbf{P}}^{sa})\mathbf{n}^\top \\ &= \hat{\mathcal{T}}^e\hat{\mathbf{U}}_{sin} + \mathcal{O}(r^0) \quad .\end{aligned} \tag{5.28}$$

Applying the operator $\hat{\mathcal{T}}^e$ (5.23) in (5.28) gives,

$$\hat{\mathbf{T}}^{ss} = (\lambda+2\mu)(\nabla\cdot\hat{\mathbf{U}}_{sin})\mathbf{n} - \mu(\mathbf{n}\times(\nabla\times\hat{\mathbf{U}}_{sin})) + 2\mu(\mathcal{M}\cdot\hat{\mathbf{U}}_{sin}) + \mathcal{O}(r^0) \tag{5.29}$$

which can be rearranged to

$$\hat{\mathbf{T}}^{ss} = \mathcal{M}\nabla^4\Psi + \mathbf{I}(\mathbf{n}^\top\nabla)\nabla^4\Psi + 2\mu(\mathcal{M}\cdot\hat{\mathbf{U}}_{sin})^\top + \mathcal{O}(r^0) \tag{5.30}$$

using (5.27a).

This is already the desired form of the kernel function, which is suitable for integration by parts. For the double layer operator

$$(\hat{\mathcal{K}}\hat{\mathbf{u}})(\tilde{\mathbf{y}}) = \int_\Gamma \left[(\mathcal{M}\nabla^4\Psi)\hat{\mathbf{u}} + (\mathbf{I}(\mathbf{n}^\top\nabla)\nabla^4\Psi)\hat{\mathbf{u}} + 2\mu(\mathcal{M}\cdot\hat{\mathbf{U}}_{sin})^\top\hat{\mathbf{u}} + \mathcal{O}(r^0)\hat{\mathbf{u}}\right]d\Gamma \quad , \tag{5.31}$$

the regularization can be performed by applying

$$\int_\Gamma (\mathcal{M}\mathbf{v})\hat{\mathbf{u}}d\Gamma = -\int_\Gamma \mathbf{v}(\mathcal{M}\hat{\mathbf{u}})d\Gamma \tag{5.32a}$$

$$\int_\Gamma (\mathcal{M}\mathbf{v})^\top\hat{\mathbf{u}}d\Gamma = \int_\Gamma \mathbf{v}^\top(\mathcal{M}\hat{\mathbf{u}})d\Gamma \tag{5.32b}$$

to the first and the third terms on the right side in (5.31), respectively.

Because $\hat{\mathbf{U}}_{sin}$ is symmetry, this yields

$$(\hat{\mathcal{K}}\hat{\mathbf{u}})(\tilde{\mathbf{y}}) = \int_{\Gamma} \left[-\nabla^4\Psi(\mathcal{M}\hat{\mathbf{u}}) + (\mathbf{I}(\mathbf{n}^\top\nabla)\nabla^4\Psi)\hat{\mathbf{u}} + 2\mu\hat{\mathbf{U}}_{sin}(\mathcal{M}\hat{\mathbf{u}}) + \mathcal{O}(r^0)\hat{\mathbf{u}} \right] d\Gamma \quad , \quad (5.33)$$

which is an equivalent form of the double layer integral operator under the assumption of a closed boundary.

The next step is the limit $\Omega \ni \tilde{\mathbf{y}} \to \mathbf{y} \in \Gamma$, which due to the before performed regularization is straightforward. For the last integral part on the right hand side of (5.33) this limit has no problem. Moreover, since the first and the third integrals on the right hand side of (5.33) have weakly singular kernel functions, they can continuously be extended to the boundary as well. The only part, which needs to be investigated, is the second term containing the normal derivative of $\nabla^4\Psi$. According to [78, 81], the jump term $c(\mathbf{y})$ becomes a constant only depending on the geometry, i.e., does neither depend on the material nor on the Laplace parameter s.

Finally, the double layer integral equation turns to

$$\lim_{r_c \to 0}(\hat{\mathcal{K}}\hat{\mathbf{u}})(\tilde{\mathbf{y}},\mathbf{x}) = (\mathbf{I}c(\mathbf{y}) - \mathbf{I})\hat{\mathbf{u}}(\mathbf{y}) + (\hat{\mathcal{K}}\hat{\mathbf{u}})(\mathbf{y},\mathbf{x}) \tag{5.34}$$

with a regularized double layer integral equation.

5.4 Boundary element formulation

To approximate the geometry, the boundary $\Gamma = \partial\Omega$ is divided into E triangle boundary elements Γ_e via a standard triangulation

$$\Gamma \approx \sum_{e=1}^{E}\Gamma_e \quad . \tag{5.35}$$

A combination of F continuous or piecewise discontinuous polynomial shape functions $N_e^f(\mathbf{x})$ is defined for the unknown Dirichlet ($f \geq 1$) and Neumann ($f \geq 0$) datum, respectively.

Hence, the following ansatz functions are used with the time–dependent nodal values $u_i^{ef}(t)$, $t_i^{ef}(t)$, $p^{w^{ef}}(t)$, $q^{w^{ef}}(t)$, $p^{a^{ef}}(t)$, and $q^{a^{ef}}(t)$

$$u_i(\mathbf{x},t) = \sum_{e=1}^{E}\sum_{f=1}^{F} N_e^f(\mathbf{x})u_i^{ef}(t) \tag{5.36a}$$

$$t_i(\mathbf{x},t) = \sum_{e=1}^{E} \sum_{f=1}^{F} N_e^f(\mathbf{x}) t_i^{ef}(t) \tag{5.36b}$$

$$p^w(\mathbf{x},t) = \sum_{e=1}^{E} \sum_{f=1}^{F} N_e^f(\mathbf{x}) p^{wef}(t) \tag{5.36c}$$

$$q^w(\mathbf{x},t) = \sum_{e=1}^{E} \sum_{f=1}^{F} N_e^f(\mathbf{x}) q^{wef}(t) \tag{5.36d}$$

$$p^a(\mathbf{x},t) = \sum_{e=1}^{E} \sum_{f=1}^{F} N_e^f(\mathbf{x}) p^{aef}(t) \tag{5.36e}$$

$$q^a(\mathbf{x},t) = \sum_{e=1}^{E} \sum_{f=1}^{F} N_e^f(\mathbf{x}) q^{aef}(t) \quad . \tag{5.36f}$$

For calculations in the next chapter, the shape functions of the unknown Dirichlet datum are linear while those of the unknown Neumann datum are constant. Inserting these ansatz functions (5.36) into the time dependent integral equation (5.18) yields

$$
\begin{aligned}
&\sum_{e=1}^{E} \sum_{f=1}^{F} \int_0^t \int_\Gamma
\begin{bmatrix}
U_{ij}^{ss}(r,\tau) & P_j^{sw}(r,\tau) & P_j^{sa}(r,\tau) \\
U_i^{ws}(r,\tau) & P^{ww}(r,\tau) & P^{wa}(r,\tau) \\
U_i^{as}(r,\tau) & P^{aw}(r,\tau) & P^{aa}(r,\tau)
\end{bmatrix}
N_e^f(\mathbf{x})
\begin{bmatrix}
t_i^{ef}(\tau) \\
-q^{wef}(\tau) \\
-q^{aef}(\tau)
\end{bmatrix}
d\Gamma d\tau \\[2mm]
&-\sum_{e=1}^{E} \sum_{f=1}^{F} \int_0^t \int_\Gamma
\begin{bmatrix}
T_{ij}^{ss}(r,\tau) & Q_j^{sw}(r,\tau) & Q_j^{sa}(r,\tau) \\
T_i^{ws}(r,\tau) & Q^{ww}(r,\tau) & Q^{wa}(r,\tau) \\
T_i^{as}(r,\tau) & Q^{aw}(r,\tau) & Q^{aa}(r,\tau)
\end{bmatrix}
N_e^f(\mathbf{x})
\begin{bmatrix}
u_i^{ef}(\tau) \\
p^{wef}(\tau) \\
p^{aef}(\tau)
\end{bmatrix}
d\Gamma d\tau \\[2mm]
&=
\begin{bmatrix}
c_{ij}(\mathbf{y}) & 0 & 0 \\
0 & c(\mathbf{y}) & 0 \\
0 & 0 & c(\mathbf{y})
\end{bmatrix}
\begin{bmatrix}
u_i(\mathbf{y},t) \\
p^w(\mathbf{y},t) \\
p^a(\mathbf{y},t)
\end{bmatrix} ,
\end{aligned}
\tag{5.37}
$$

where $c_{ij}(\mathbf{y}) = \delta_{ij} c(\mathbf{y})$, and the double layer operator is already regularized with regard to section 5.3.2.

Next, a time discretization has to be introduced. Since no time–dependent fundamental solutions are known, the convolution quadrature method is the most effective method compared to the possibility inverting the Laplace domain fundamental solutions at every collocation point in every time step using a series expansion [31].

By dividing the time period t in N intervals of equal duration Δt, i.e., $t = N\Delta t$, the convolution integrals between the fundamental solutions and the nodal values in (5.37) are approximated by the Convolution Quadrature Method. This results in the following boundary

element time stepping formulation for $n = 0, 1, 2, ..., N$

$$
\sum_{e=1}^{E}\sum_{f=1}^{F}\sum_{k=0}^{n}
\begin{bmatrix}
\omega_{n-k}^{ef}(\hat{U}_{ij}^{ss}, \mathbf{y}, \Delta t) & \omega_{n-k}^{ef}(\hat{P}_{j}^{sw}, \mathbf{y}, \Delta t) & \omega_{n-k}^{ef}(\hat{P}_{j}^{sa}, \mathbf{y}, \Delta t) \\
\omega_{n-k}^{ef}(\hat{U}_{i}^{ws}, \mathbf{y}, \Delta t) & \omega_{n-k}^{ef}(\hat{P}^{ww}, \mathbf{y}, \Delta t) & \omega_{n-k}^{ef}(\hat{P}^{wa}, \mathbf{y}, \Delta t) \\
\omega_{n-k}^{ef}(\hat{U}_{i}^{as}, \mathbf{y}, \Delta t) & \omega_{n-k}^{ef}(\hat{P}^{aw}, \mathbf{y}, \Delta t) & \omega_{n-k}^{ef}(\hat{P}^{aa}, \mathbf{y}, \Delta t)
\end{bmatrix}
\begin{bmatrix}
t_{i}^{ef}(k\Delta t) \\
-q^{wef}(k\Delta t) \\
-q^{aef}(k\Delta t)
\end{bmatrix}
$$

$$
-\sum_{e=1}^{E}\sum_{f=1}^{F}\sum_{k=0}^{n}\int_{\Gamma}
\begin{bmatrix}
\omega_{n-k}^{ef}(\hat{T}_{ij}^{ss}, \mathbf{y}, \Delta t) & \omega_{n-k}^{ef}(\hat{Q}_{j}^{sw}, \mathbf{y}, \Delta t) & \omega_{n-k}^{ef}(\hat{Q}_{j}^{sa}, \mathbf{y}, \Delta t) \\
\omega_{n-k}^{ef}(\hat{T}_{i}^{ws}, \mathbf{y}, \Delta t) & \omega_{n-k}^{ef}(\hat{Q}^{ww}, \mathbf{y}, \Delta t) & \omega_{n-k}^{ef}(\hat{Q}^{wa}, \mathbf{y}, \Delta t) \\
\omega_{n-k}^{ef}(\hat{T}_{i}^{as}, \mathbf{y}, \Delta t) & \omega_{n-k}^{ef}(\hat{Q}^{aw}, \mathbf{y}, \Delta t) & \omega_{n-k}^{ef}(\hat{Q}^{aa}, \mathbf{y}, \Delta t)
\end{bmatrix}
\begin{bmatrix}
u_{i}^{ef}(k\Delta t) \\
p^{wef}(k\Delta t) \\
p^{aef}(k\Delta t)
\end{bmatrix}
$$

$$
=
\begin{bmatrix}
c_{ij}(\mathbf{y}) & 0 & 0 \\
0 & c(\mathbf{y}) & 0 \\
0 & 0 & c(\mathbf{y})
\end{bmatrix}
\begin{bmatrix}
u_{i}(\mathbf{y}, n\Delta t) \\
p^{w}(\mathbf{y}, n\Delta t) \\
p^{a}(\mathbf{y}, n\Delta t)
\end{bmatrix} \quad ,
$$

$$(5.38)$$

with the integration weights, e.g.,

$$
\omega_{n}^{ef}(\hat{U}_{ij}^{ss}, \mathbf{y}, \Delta t) = \frac{\mathcal{R}^{-n}}{L}\sum_{\ell=0}^{L-1}\int_{\Gamma}\hat{U}_{ij}^{ss}\left(\mathbf{x}, \mathbf{y}, \frac{\gamma(\mathcal{R}e^{i\ell\frac{2\pi}{L}})}{\Delta t}\right)N_{e}^{f}(\mathbf{x})d\Gamma e^{-in\ell\frac{2\pi}{L}} \quad .
$$

$$(5.39)$$

See appendix A.3 for the details on the CQM.

Note that the calculation of the integration weights is only based on the Laplace transformed fundamental solutions (see appdendix A.4) which are available. Therefore, with the time stepping procedure (5.38) a boundary element formulation for partially saturated poroelastodynamics is given without time–dependent fundamental solutions. The numerical implementation is accomplished by using the open source C++ BEM library HyENA [82].

5.5 Domain solution evaluation

For the proposed boundary element method, the values of the field variables inside the domain can be calculated by using the representation formulae. This requires that the values of the boundary variables are known.

Equation (5.38) can be used to calculated the unknown displacement $\hat{u}_{i}(\mathbf{y}, t)$, pore water pressure $\hat{p}^{w}(\mathbf{y}, t)$, and pore air pressure $\hat{p}^{a}(\mathbf{y}, t)$ at a point $\mathbf{y} \in \Omega$, when the value of the

jump term $c(\mathbf{y})$ is set to 1, which is expressed as

$$
\sum_{e=1}^{E}\sum_{f=1}^{F}\sum_{k=0}^{n}
\begin{bmatrix}
\omega_{n-k}^{ef}(\hat{U}_{ij}^{ss},\mathbf{y},\Delta t) & \omega_{n-k}^{ef}(\hat{p}_{j}^{sw},\mathbf{y},\Delta t) & \omega_{n-k}^{ef}(\hat{p}_{j}^{sa},\mathbf{y},\Delta t) \\
\omega_{n-k}^{ef}(\hat{U}_{i}^{ws},\mathbf{y},\Delta t) & \omega_{n-k}^{ef}(\hat{p}^{ww},\mathbf{y},\Delta t) & \omega_{n-k}^{ef}(\hat{p}^{wa},\mathbf{y},\Delta t) \\
\omega_{n-k}^{ef}(\hat{U}_{i}^{as},\mathbf{y},\Delta t) & \omega_{n-k}^{ef}(\hat{p}^{aw},\mathbf{y},\Delta t) & \omega_{n-k}^{ef}(\hat{p}^{aa},\mathbf{y},\Delta t)
\end{bmatrix}
\begin{bmatrix}
t_{i}^{ef}(k\Delta t) \\
-q^{wef}(k\Delta t) \\
-q^{aef}(k\Delta t)
\end{bmatrix}
$$

$$
-\sum_{e=1}^{E}\sum_{f=1}^{F}\sum_{k=0}^{n}\int_{\Gamma}
\begin{bmatrix}
\omega_{n-k}^{ef}(\hat{T}_{ij}^{ss},\mathbf{y},\Delta t) & \omega_{n-k}^{ef}(\hat{Q}_{j}^{sw},\mathbf{y},\Delta t) & \omega_{n-k}^{ef}(\hat{Q}_{j}^{sa},\mathbf{y},\Delta t) \\
\omega_{n-k}^{ef}(\hat{T}_{i}^{ws},\mathbf{y},\Delta t) & \omega_{n-k}^{ef}(\hat{Q}^{ww},\mathbf{y},\Delta t) & \omega_{n-k}^{ef}(\hat{Q}^{wa},\mathbf{y},\Delta t) \\
\omega_{n-k}^{ef}(\hat{T}_{i}^{as},\mathbf{y},\Delta t) & \omega_{n-k}^{ef}(\hat{Q}^{aw},\mathbf{y},\Delta t) & \omega_{n-k}^{ef}(\hat{Q}^{aa},\mathbf{y},\Delta t)
\end{bmatrix}
\begin{bmatrix}
u_{i}^{ef}(k\Delta t) \\
p^{wef}(k\Delta t) \\
p^{aef}(k\Delta t)
\end{bmatrix}
$$

$$
=
\begin{bmatrix}
u_{i}(\mathbf{y},n\Delta t) \\
p^{w}(\mathbf{y},n\Delta t) \\
p^{a}(\mathbf{y},n\Delta t)
\end{bmatrix}
,
\tag{5.40}
$$

while for the evaluation of the inner point value, there is no singularity involved in the integral equation.

5.6 Variable transformation

In order to achieve stable numerical solutions, dimensionless variables are introduced in this chapter as in the work of Chen and Dargush [31] and Schanz and Kielhorn [103]. In order not to alter the governing equations, the linear transformations

$$
\bar{x}_i = \frac{x_i}{A} \tag{5.41a}
$$

$$
\bar{t}_i = \frac{t_i}{B} \tag{5.41b}
$$

$$
\bar{K} = \frac{K}{C} \tag{5.41c}
$$

$$
\bar{G} = \frac{G}{C} \tag{5.41d}
$$

$$
\bar{K}_s = \frac{K_s}{C} \tag{5.41e}
$$

$$
\bar{K}_w = \frac{K_w}{C} \tag{5.41f}
$$

$$
\bar{K}_a = \frac{K_a}{C} \tag{5.41g}
$$

of spatial coordinates, time coordinates, and material data, respectively, are performed by using three different constant values A, B, $C \in \mathbb{R}^+$. Thus, taking into account the transformations, the spatial, the first and second time derivative yield

$$
\frac{\partial u_i}{\partial x_j} = \frac{A\partial \bar{u}_i}{A\partial \bar{x}_j} = \bar{u}_{i,\bar{j}} \tag{5.42a}
$$

$$\frac{\partial u_i}{\partial t} = \frac{A \partial \bar{u}_i}{B \partial \bar{t}} = \frac{A}{B} \frac{\partial \bar{u}_i}{\partial t} \tag{5.42b}$$

$$\frac{\partial^2 u_i}{\partial t^2} = \left(\frac{\partial}{\partial t}\right) \left(\frac{\partial u_i}{\partial t}\right) = \left(\frac{\partial}{B \partial \bar{t}}\right) \left(\frac{A \partial \bar{u}_i}{B \partial \bar{t}}\right) = \frac{A}{B^2} \frac{\partial^2 \bar{u}_i}{\partial \bar{t}^2} \quad . \tag{5.42c}$$

The divergence of the stress tensor is related to the transformation by

$$\sigma_{ij,j} = \frac{\partial \sigma_{ij}}{\partial x_j} = \frac{C \partial \bar{\sigma}_{ij}}{A \partial \bar{x}_j} = \frac{C}{A} \bar{\sigma}_{ij,\bar{j}} \quad , \tag{5.43}$$

and the densities are related to the transformation by

$$\bar{\rho}_s = \frac{A^2}{B^2 C} \rho_s \tag{5.44a}$$

$$\bar{\rho}_w = \frac{A^2}{B^2 C} \rho_w \tag{5.44b}$$

$$\bar{\rho}_a = \frac{A^2}{B^2 C} \rho_a \quad . \tag{5.44c}$$

The remaining dimensionless variables for the permeabilities are

$$\bar{\kappa}_w = \frac{BC}{A^2} \kappa_w \tag{5.45a}$$

$$\bar{\kappa}_a = \frac{BC}{A^2} \kappa_a \quad . \tag{5.45b}$$

Due to the large scale variation of the material data, especially when noticing the differences between the compressibility modulus and the permeability, bad conditioned equation systems will occur in numerical solution schemes. Therefore, the variable is transformed in the following way:

$$\bar{K} = \bar{\kappa}_w = \bar{\rho}_w = 1 \quad ,$$

and this will lead to the following equations

$$\frac{1}{C} K = 1 \tag{5.46a}$$

$$\frac{BC}{A^2} \kappa_w = 1 \tag{5.46b}$$

$$\frac{A^2}{B^2 C} \rho_w = 1 \quad . \tag{5.46c}$$

Solving the upper equations for the unknown parameters yield

$$A = \kappa_w \sqrt{K \rho_w} \tag{5.47a}$$

$$B = \rho_w \kappa_w \tag{5.47b}$$

$$C = K \quad . \tag{5.47c}$$

The benefits gained by using dimensionless variables is obvious when considering the condition number of resulting system matrices.

6 NUMERICAL EXAMPLES

In this chapter, the previously introduced collocation boundary element method is applied on some numerical examples. At the very beginning, a three dimensional partially saturated poroelastic column is calculated in both frequency and time domain. The numerical results are compared with the one dimensional analytical solutions given in chapter 3. Additionally, the numerical calculation parameters such as mesh size and time step size are investigated. Second, a partially saturated poroelastic halfspace is calculated and discussed. By comparing with the theoretic arriving time of the fast compressional wave, the shear wave and the Rayleigh wave, the numerical results are analyzed and controlled according to specific numerical calculation parameters. Finally, a partially saturated poroelastic halfspace is assumed, and an application of an open trench for vibration isolation is performed and studied by using different geometry data.

For all the numerical examples, the surface is discretized with linear triangle elements. For the material data, the Massilon Sandstone as shown in Table 3.1 is chosen. The initial water saturation is set to $S_w = 0.9$, the pore size distribution index ϑ is set to 1.5, the residual water saturation S_{rw} is set to 0, and the air entry saturation S_{ra} is set to 1. For the CQM based time domain results, the underlying multistep method $\gamma(z)$ is chosen to be a BDF 2 ($\gamma(z) = 1.5 - 2z + 0.5z^2$) and $\mathcal{R}^N = 10^{-5}$ is applied.

6.1 A three dimensional partially saturated poroelastic column

In this section, a three dimensional partially saturated poroelastic column is calculated with the proposed collocation boundary element method.

The column has a length of $3\,\mathrm{m}$, a cross section of width and height of $1\,\mathrm{m}$. In order to compare with the one dimensional solution, the boundary conditions are the same as in the one dimensional case in chapter 3, where no fluid flux at the bottom and around the column is allowed. The normal displacement at the bottom and the four sides is also set to zero as shown in figure 6.1. The top of the column is excited by a stress jump according to a unit step function (Heaviside load). Furthermore, the Poisson's ratio artificially is set to zero. The displacement u_z at the top center of the column, the pore water pressure p^w and the pore air pressure p^a at the bottom center of the column will be calculated.

In order to obtain good numerical results and to reduce as much as possible numerical damping, an optimal time step size Δt corresponding to every mesh should be chosen.

$$u_y = 0 \quad q^w = 0 \quad q^a = 0$$

$$u_z = 0$$
$$q^w = 0$$
$$q^a = 0$$

$$u_x = 0 \quad q^w = 0$$
$$q^a = 0$$

$$\sigma_z = 1\,\mathrm{Nm}^{-2}H(t)$$
$$p^w = 0$$
$$p^a = 0$$
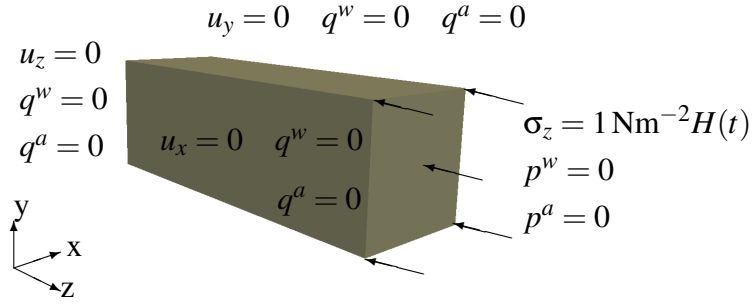
Figure 6.1: Geometry and boundary conditions of a three dimensional partially saturated poroelastic column

This optimal choice depends basically on the wave velocities and the spatial discretization. Therefore, the dimensionless Courant–Friedrichs–Levy number

$$\beta_{CFL} = \frac{v_{p_1}\Delta t}{r_e} \tag{6.1}$$

is introduced, where v_{p_1} is calculated according to Gassman's equation representing the fast compressional wave velocity and r_e is a characteristic element length. This characteristic element length r_e, in the two dimensional case, is simply the mean value of all element lengths. However, for the three dimensional case, each element of the surface mesh has two dimensions, so it is not clear which length should be chosen. In this paper, the max value of the cathetus of the triangles is chosen. In most boundary element formulations in time domain, the value β is restricted to a very small range where stable and satisfactory results are achieved. According to related works [100], good results could be obtained with a value of $\beta = 0.3$.

Three different surface meshes as shown in Figure 6.2 with 224, 896 and 2016 linear triangle elements will be used to calculate, where the corresponding characteristic element length r_e is $1/2$ m, $1/4$ m, and $1/6$ m, respectively.

Influence of the spatial discretization   First, the influence on the spatial discretization of the results in the Laplace domain is studied. In figure 6.3, the displacement at the top center of the column is compared with the corresponding one dimensional analytical result. Obviously, the numerical result of $r_e = 1/2$ m is not acceptable because of the large shift of the value of the eigenfrequency. The numerical result of $r_e = 1/4$ m is better while the value of the eigenfrequency is closer to the analytical solution, however, the amplitude at the eigenfrequency is still not acceptable, here, the mesh is still too coarse. For $r_e = 1/6$ m, the numerical result is good, both the eigenfrequency and the amplitude coincide well with the one dimensional analytical solution. For the pore water and pore air pressure as shown

(a) $r_e = 1/2\,\mathrm{m}$ (b) $r_e = 1/4\,\mathrm{m}$ (c) $r_e = 1/6\,\mathrm{m}$
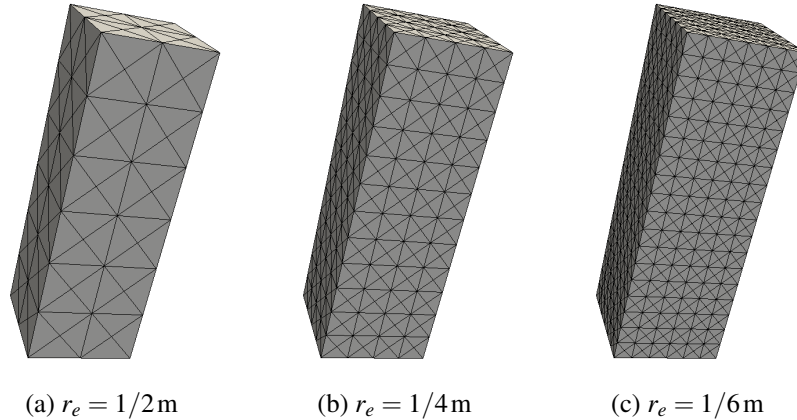
Figure 6.2: Different surface meshes

in figure 6.4 and 6.5, the numerical results of different mesh sizes compared with the analytical solutions show a similar behavior as the displacement results.

Next, the time domain results of the displacement and pore pressure are given in figure 6.6(a), 6.7(a), and 6.8(a). For all the time domain calculations the mesh size is varied, whereas, the CFL number is fixed and set to $\beta_{CFL} = 0.3$. According to the displacement results, when the mesh size is set to $r_e = 1/6\,\mathrm{m}$, the three dimensional numerical result coincides best with the one dimensional analytical solution in time domain. For a coarser mesh as $r_e = 1/2\,\mathrm{m}$ or $r_e = 1/4\,\mathrm{m}$, a somehow stronger numerical damping can be observed towards larger time period. However, the numerical results of different mesh sizes are acceptable no matter calculating with a coarse mesh or a fine mesh. It holds that the numerical results can be improved with a finer mesh but more calculation time is needed.

On the other hand, the three dimensional numerical results of the pore pressure show more sensitivity with regard to the mesh size. The best results for both the pore water and pore air pressure compared with the one dimensional analytical solutions are obtained according to the calculation when the mesh size is set to $r_e = 1/6\,\mathrm{m}$. However, for a coarser mesh as $r_e = 1/2\,\mathrm{m}$ or $r_e = 1/4\,\mathrm{m}$, the numerical results are not good because the amplitudes of both the pore water and pore air pressure are slightly smaller than the analytical solutions. What's more, the numerical results can hardly be trusted towards larger time period, i.e., after $t = 0.025s$.
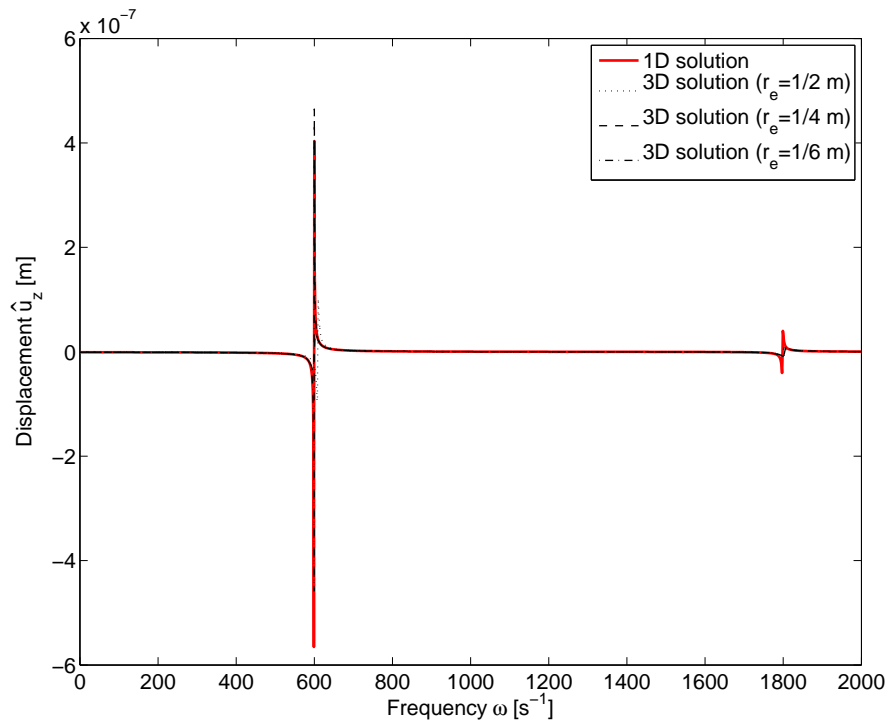
(a) Full scale
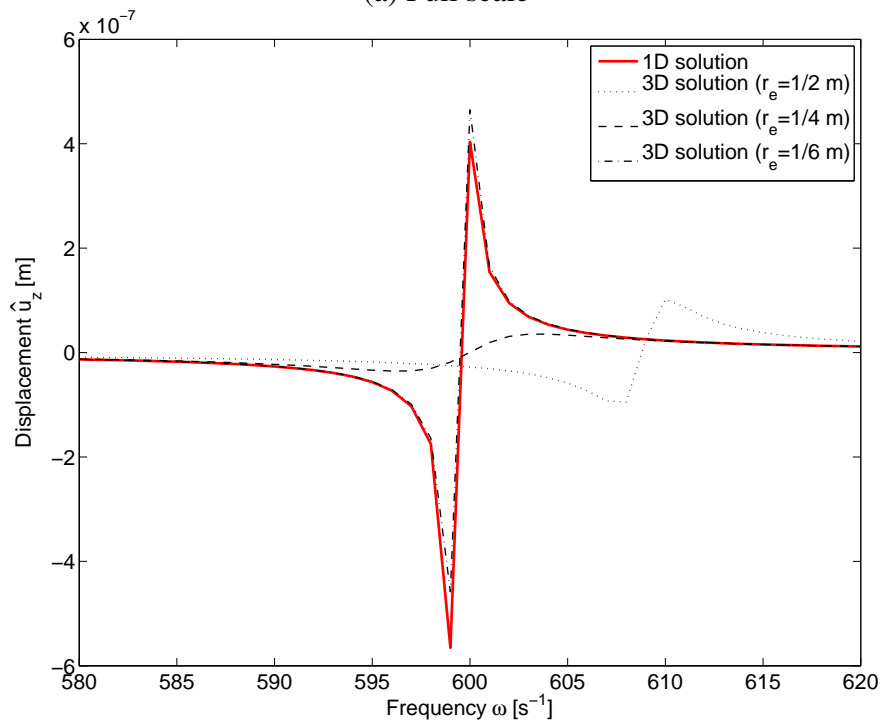
(b) Zoom

Figure 6.3: Displacement $\hat{u}_z$ versus frequency at the top center of the column
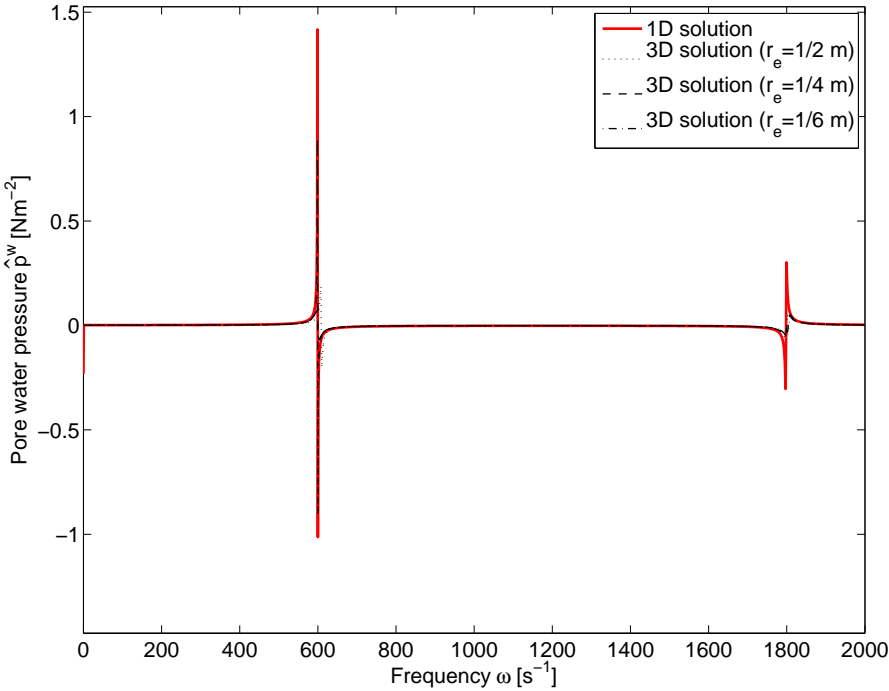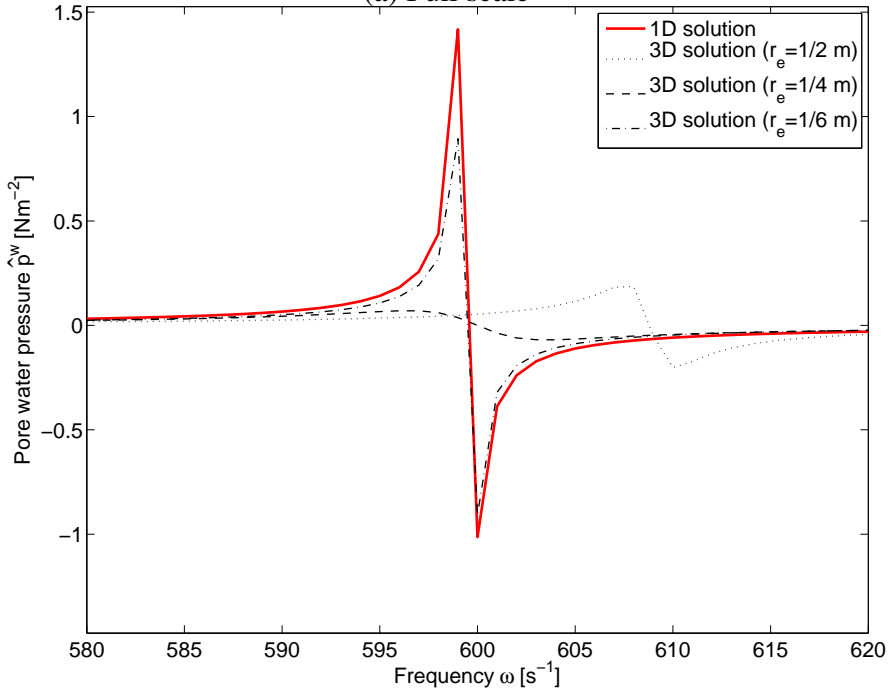
(a) Full scale

(b) Zoom

Figure 6.4: Pore water pressure $\hat{p}^w$ versus frequency at the bottom center of the column
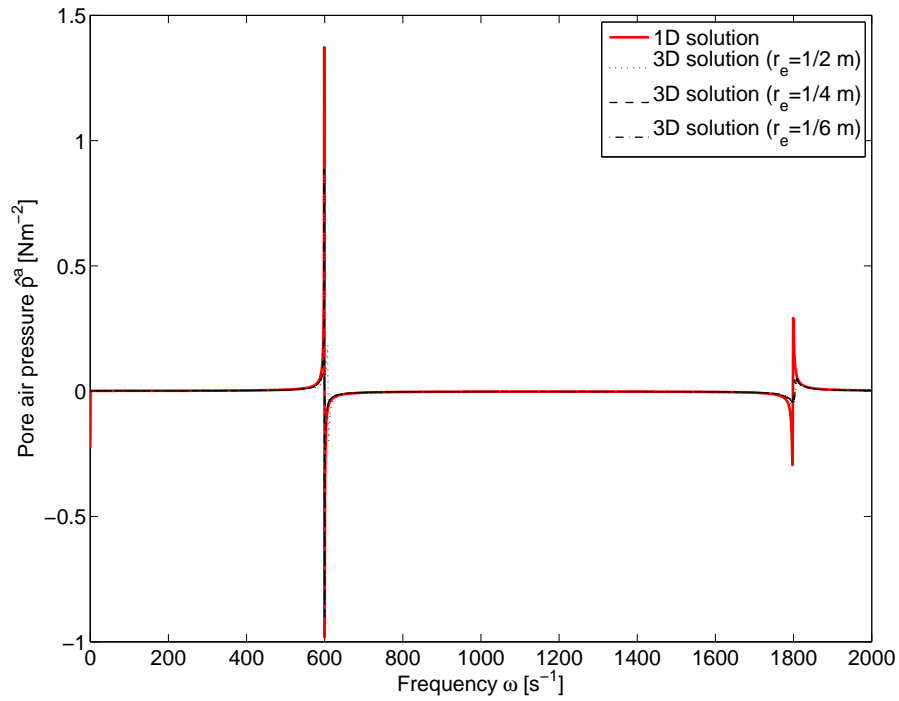
(a) Full scale
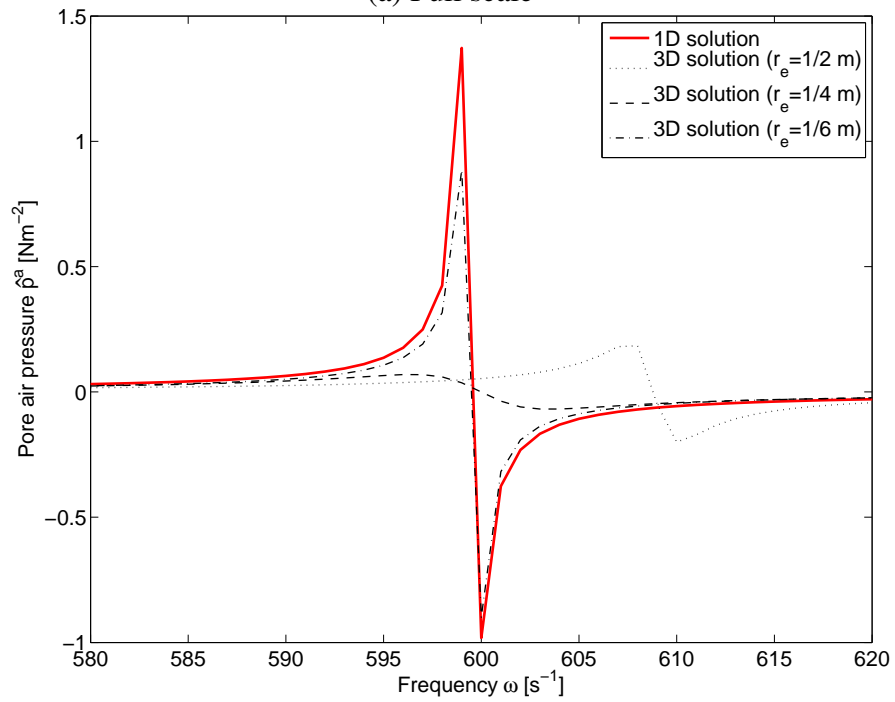
(b) Zoom

Figure 6.5: Pore air pressure $\hat{p}^a$ versus frequency at the bottom center of the column

Influence of the time discretization   Time step is of much importance in dynamic calculation since it affects the result accuracy and the efficiency. The choice of the time step should follow the rule to be small enough for the result accuracy and as large as possible for the calculation efficiency. As concluded before, a fine mesh size as $r_e = 1/6$ m can result in satisfying numerical results for both the displacement and the pore pressure. The following calculations are performed with the same mesh size of $r_e = 1/6$ m but the CFL number is varied from $\beta_{CFL} = 0.1$ to $\beta_{CFL} = 1.0$.

In figure 6.6(b), the three dimensional numerical displacement results are given together with the one dimensional analytical solution. No matter calculating with a large time step ($\beta_{CFL} = 1.0$, $\Delta t = 0.0001456$ s) or with a very small time step ($\beta_{CFL} = 0.1$, $\Delta t = 0.00001456$ s), all the numerical displacement results are acceptable and will become better and better with decreasing the value of the CFL number β_{CFL}. Besides, the numerical results of the displacement are stable with regard to different time steps within the prescribed time period.

For the numerical results of the pore pressure as shown in figure 6.7(b) and 6.8(b), both the pore water and pore air pressure results are acceptable and nearly independent on the time step size with $\beta_{CFL} \leq 0.5$ while for a large time step as $\beta_{CFL} = 1.0$, the result turns worse towards larger time period, i.e., after $t = 0.015$ s.

Besides, with a very small time step size as $\beta = 0.1$ and $\Delta t = 0.00001456$ s, a slight instability can be observed for both the traction and the pore pressure results as shown in figure 6.9 and 6.10. In figure 6.9, obvious fluctuation can be observed after the arrival of the fast compressional wave at $t = 0.0026$ s. After a long time period, it can be anticipated that the traction starts to blow up. In figure 6.10, obvious fluctuation can be observed after $t = 0.008$ s, and it can also be anticipated that the pore pressure will blow up for a longer time period.

Finally, comparing the study concerning spatial and temporal discretization for the partially saturated poroelasticity, it can be confirmed that the partially saturated poroelasticity formulation needs very fine mesh and small time step size to achieve a better result. However, compared with calculating the pore pressure, the calculation of the displacement can be satisfying with a somehow coarser mesh and larger time step size. Therefore, two different time step sizes or mesh sizes, one for the solid displacement, and one for the fluid pore pressure would be preferable, i.e., the spatial or the temporal discretization can not be optimal for both the displacement and the pore pressure.
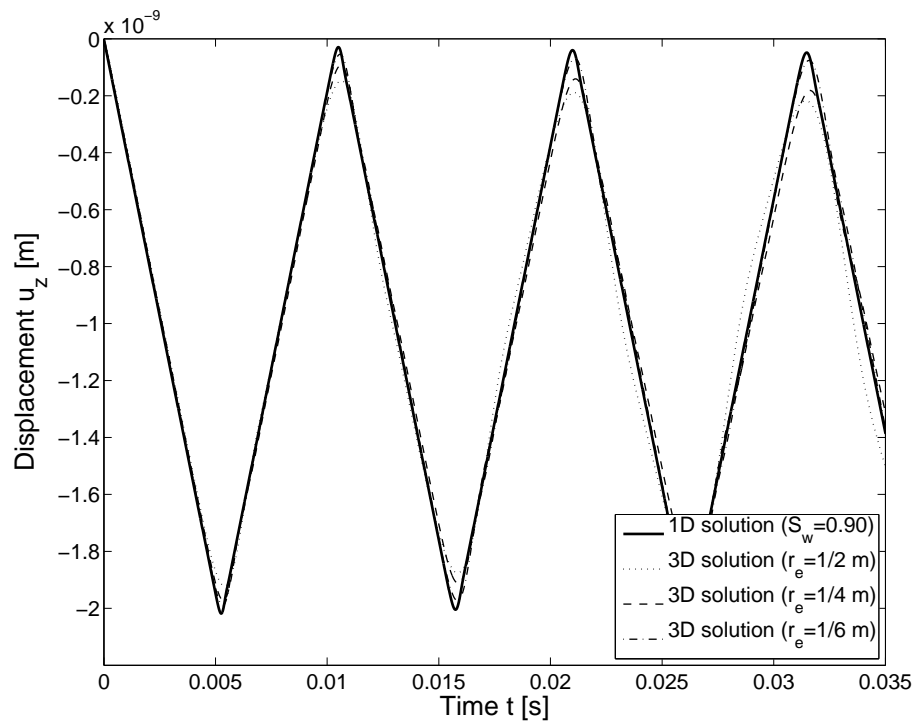
(a) With varying mesh size
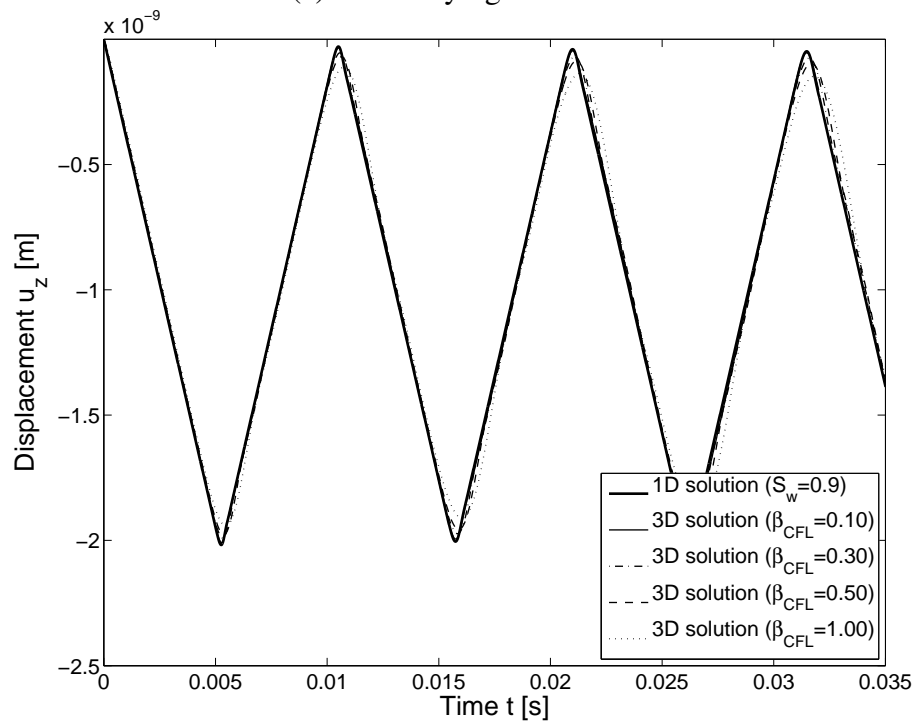
(b) With varying CFL number

Figure 6.6: Displacement u_z versus time at the top center of the column
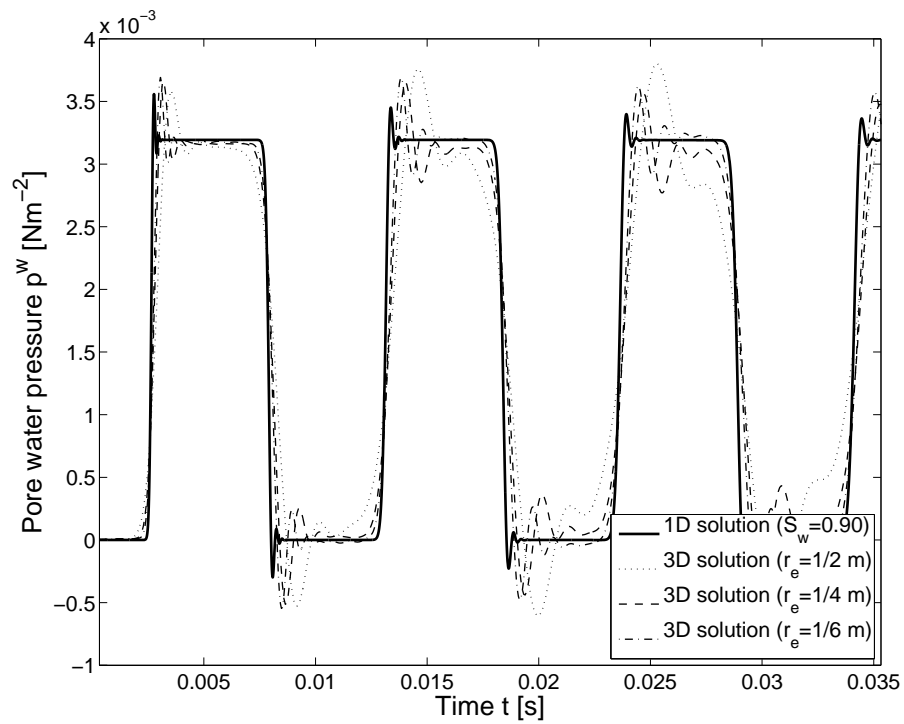
(a) With varying mesh size
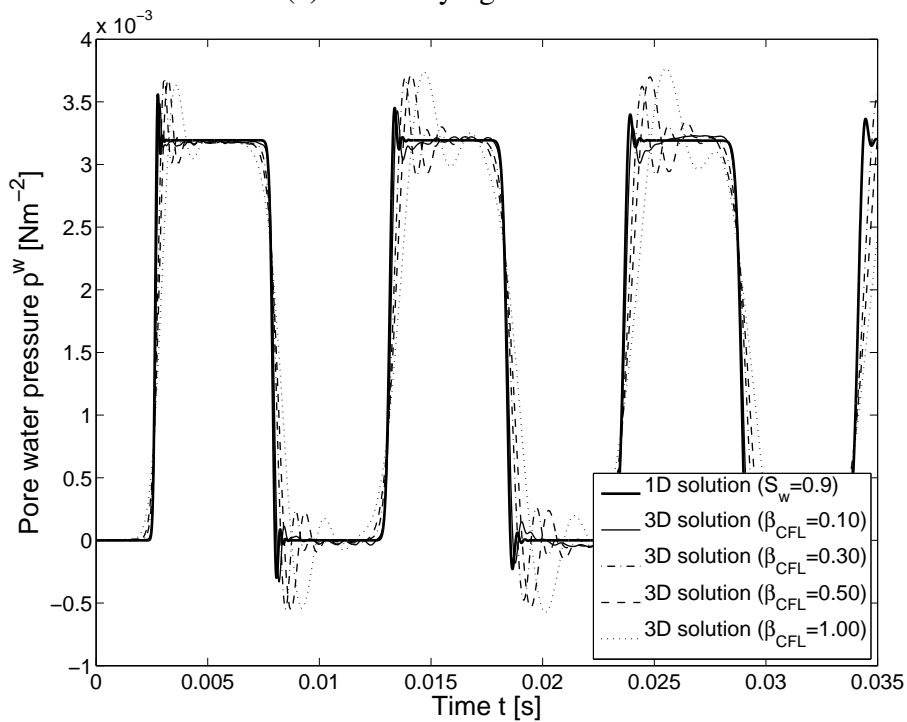
(b) With varying CFL number

Figure 6.7: Pore water pressure p^w versus time at the bottom center of the column
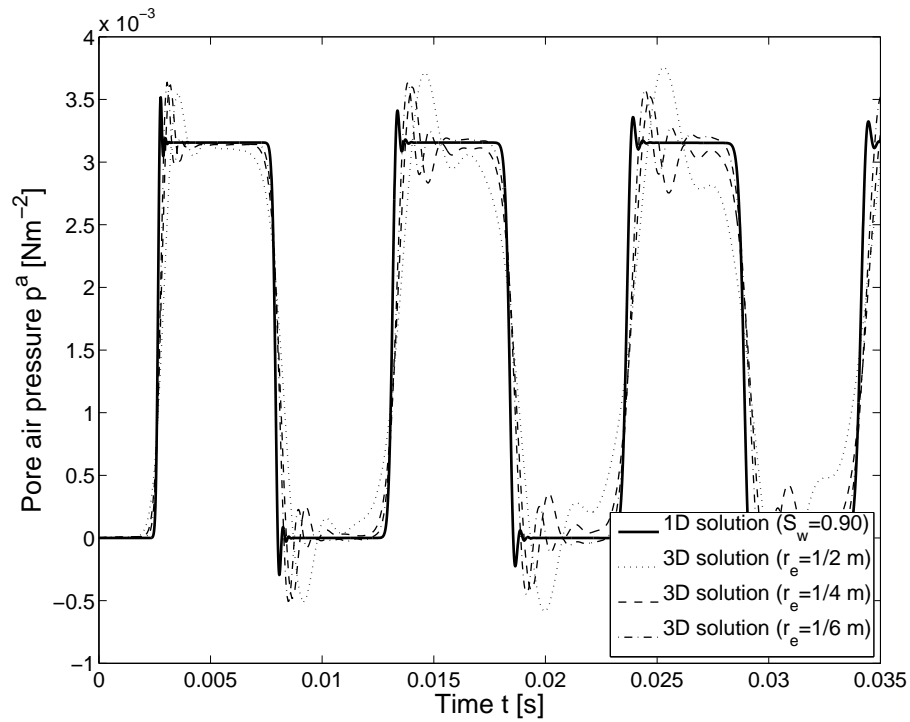
(a) With varying mesh size
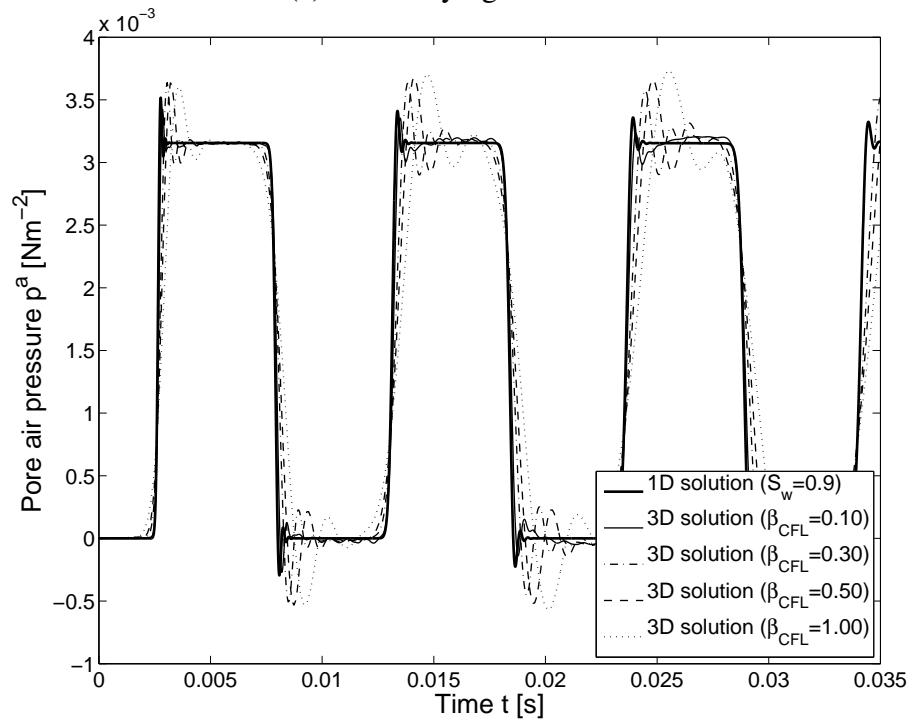
(b) With varying CFL number

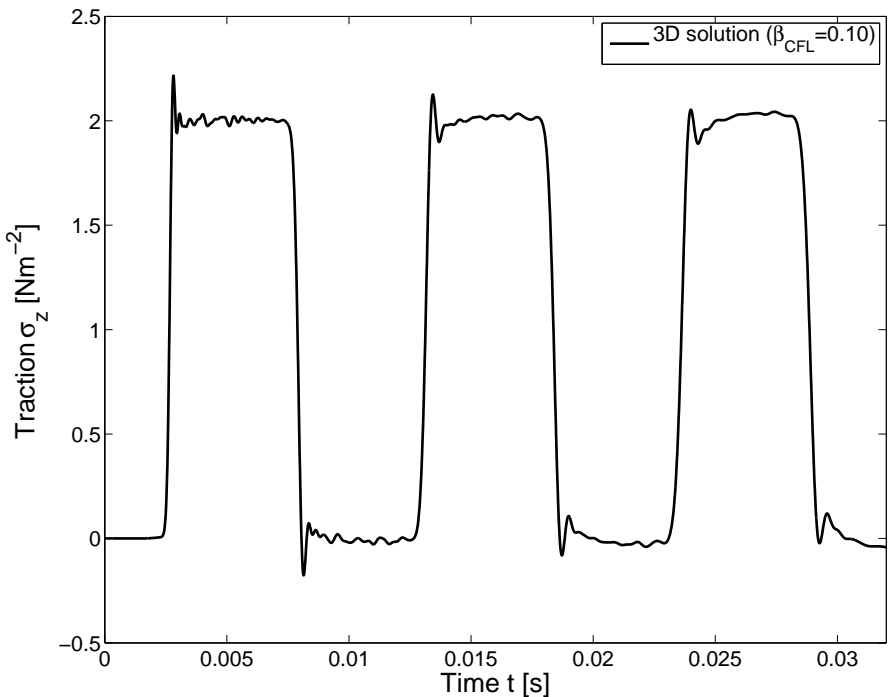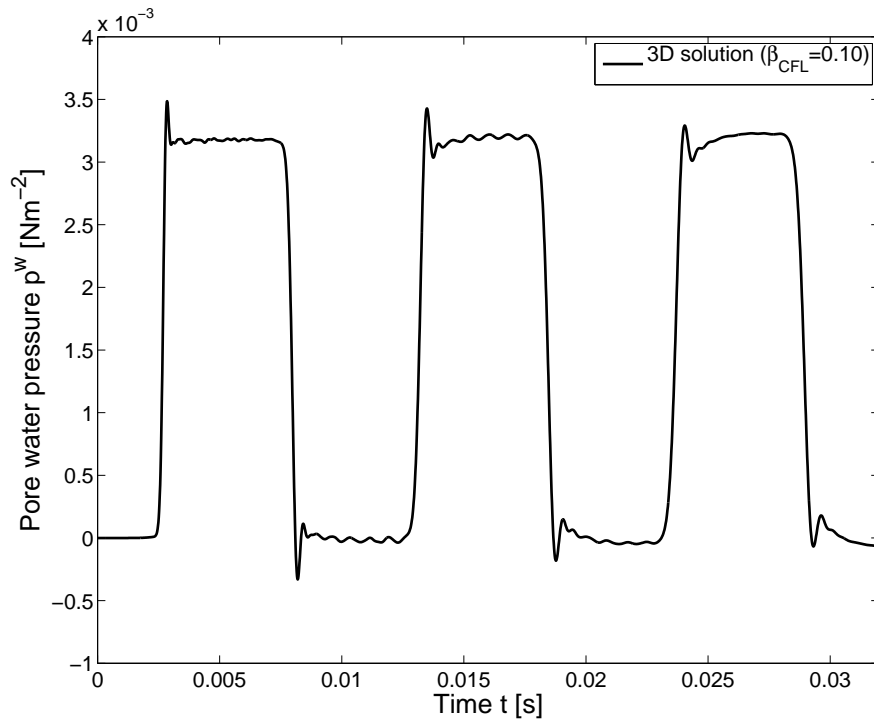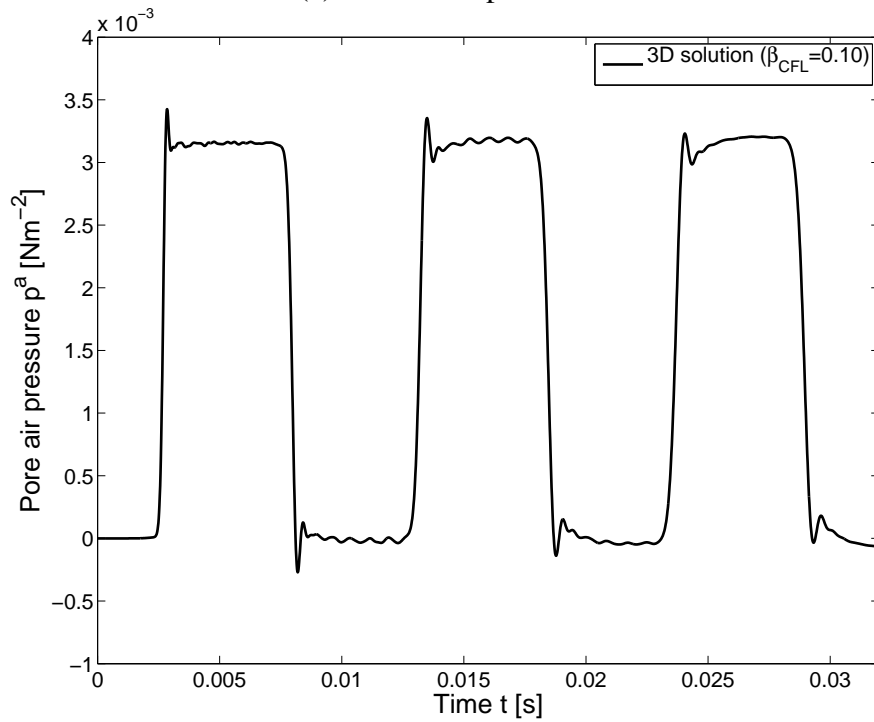Figure 6.8: Pore air pressure p^a versus time at the bottom center of the column

Figure 6.9: Traction σ_z versus time at the bottom center of the column with $\beta_{CFL} = 0.10$

(a) Pore water pressure

(b) Pore air pressure

Figure 6.10: Pore pressure p versus time at the bottom center of the column with $\beta_{CFL} = 0.10$

6.2 A partially saturated poroelastic halfspace

Various dynamic problems turn out to be a halfspace problem as pile driving, dynamic compaction, vibratory compaction, vibrations induced by wind turbines, blast induced vibrations, traffic induced vibrations, vibration isolation, etc. Dealing with wave propagation in a halfspace, surface waves are one of the most interesting effects. Especially, the Rayleigh wave is of interest due to the disastrous consequence in earthquakes. This surface wave caused by wave reflections at the free surface was first investigated by Lord Rayleigh [93], who has shown that its effect decreases rapidly with depth and its velocity of propagation is smaller than that of a body wave. For the elasticity, this wave velocity v_r can be approximated by the formula [55]

$$v_r = \frac{0.87 + 1.12\nu}{1 + \nu} v_{p1} \quad .$$

(6.2)

Analytically, the Rayleigh wave is found in the solution presented by Pekeris [90]. He assumed a point Heaviside load on the traction free surface of an elastic halfspace. However, the elastic material parameters can not be chosen arbitrarily in the solution, Poisson's ratio is fixed on $\nu = 0.25$, whereas the Young's modulus is free. According to the results by Pekeris [90], the arrival of the fast compression wave is identified as the first deviation from the zero value, and the arrival of the shear wave is not visible due to the strong increase of the displacement value up to infinity. This pole, sometimes called Rayleigh pole, indicates the arrival of the Rayleigh wave.

To capture this pole for a partially saturated poroelastic halfspace, the proposed boundary element formulation will be used. Because in the boundary element formulation applied here a full space fundamental solution is used, the free surface has to be discretized. A square surface ($5\,\text{m} \times 5\,\text{m}$) is discretized with two different meshes ($r_e = 1/2\,\text{m}$ and $r_e = 1/4\,\text{m}$, see Figure 6.11). The modeled halfspace is loaded on the area as shown in Figure 6.11 by a vertical total stress vector $\sigma_z = 1\,\text{Nm}^{-2} H(t)$ and the remaining surface is traction free. Both of the pore water and pore air pressure are assumed to be zero all over the surface. The observation points A and B for the vertical and radial displacement u_z and u_y are located in the center at $1\,\text{m}$ and $2\,\text{m}$ from the loading area. The theoretical arriving time at the points A and B of the fast compressional wave, the shear wave and the Rayleigh wave, is computed by the equations (3.18a), (4.8d) and (6.2) for a fixed frequency value, respectively (see Table 6.1). Note, the fast compressional wave, the shear wave, and the Rayleigh wave velocities are frequency independent.

In the engineering community, this is a classical problem to be studied with boundary elements. When dealing with such a domain, two obvious error sources are introduced: First, the discretization error due to the necessary truncation of the infinite boundary at some finite extent as depicted in Figure 6.11, and second, the implication this truncation has on the double layer operator. This results in a violation of its definition as a Cauchy
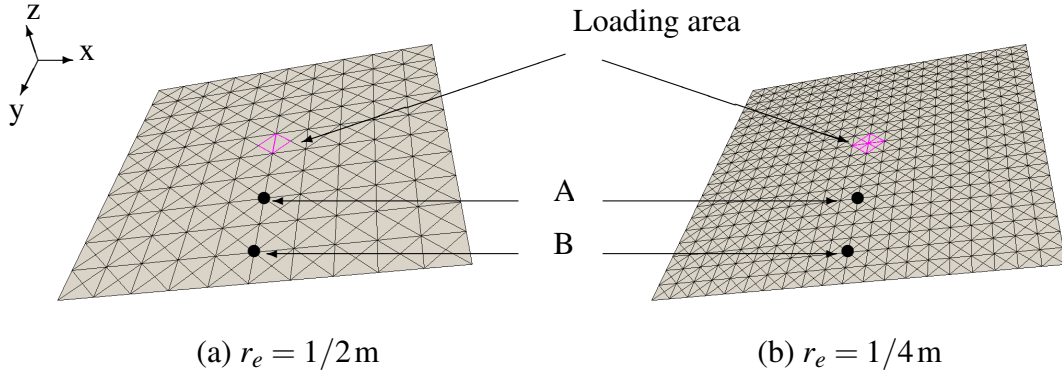
(a) $r_e = 1/2\,\mathrm{m}$ (b) $r_e = 1/4\,\mathrm{m}$

Figure 6.11: Different halfspace surface meshes

Table 6.1: Wave velocities and corresponding arriving time (Laplace parameter $s = 100$)

Point	$V_{p_1}\,[\mathrm{ms}^{-1}]$	$V_s\,[\mathrm{ms}^{-1}]$	$V_r\,[\mathrm{ms}^{-1}]$	$t_{p_1}\,[\mathrm{s}]$	$t_s\,[\mathrm{s}]$	$t_r\,[\mathrm{s}]$
A	1144.76	800.55	700.68	0.000874	0.00125	0.00143
B	1144.76	800.55	700.68	0.00175	0.00250	0.00285

Principal Value in the classical formulation, or in a violation of the assumption of a closed boundary within the here presented approach. Note that this error is strictly due to the discretization, on the continuous level, where the regularization was performed, $\partial\Gamma = \{0\}$ still holds for the halfspace.

In Figure 6.12 and Figure 6.13, with coarse mesh $r_e = 1/2\,\mathrm{m}$, the results are independent on the CFL number β_{CFL}, and both of the results are not sufficient according to the theoretical arriving time of the fast compressional wave. While for a finer mesh, with no matter a larger or a smaller CFL number, the numerical results agree well with the theoretical arriving time of the fast compressional wave. One remark is that the two slow compressional waves are not visible for the given material parameters. Due to the similar wave speed of the shear and the Rayleigh wave, a distinction at such a short distance is not possible, which makes the identification of their arrival times nearly impossible. It is obvious that the amplitude becomes larger and the overshooting after the Rayleigh wave is smaller with a smaller β_{CFL}. In this case, to obtain a good result for a partially saturated poroelastic halfspace, a fine mesh is always necessary, and to obtain a closest amplitude according to the analytical solution, a small β_{CFL} should be applied.

Next, the displacement and the pore pressure results below the observation point B are studied as shown in figure 6.14 and 6.15. It is clear to see that the amplitude of the Rayleigh wave peak around about $t = 0.003\,\mathrm{s}$ decreases rapidly as expected for a surface wave. For the pore pressure, the fast compressional wave produces a pressure jump first, and with a subsequent creeping, the pore pressure drop to the final value.
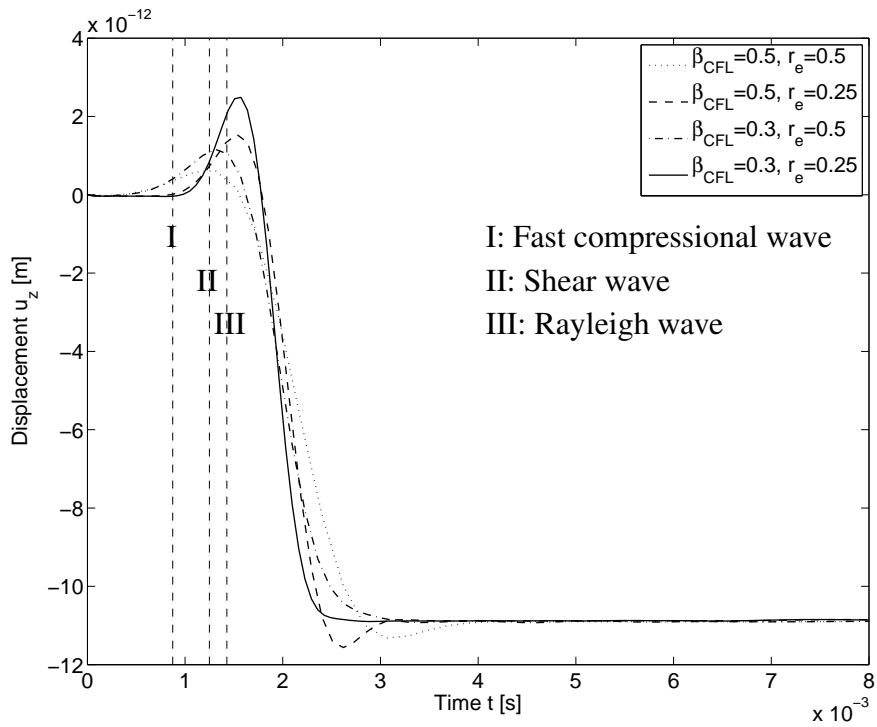
(a) Observation point A
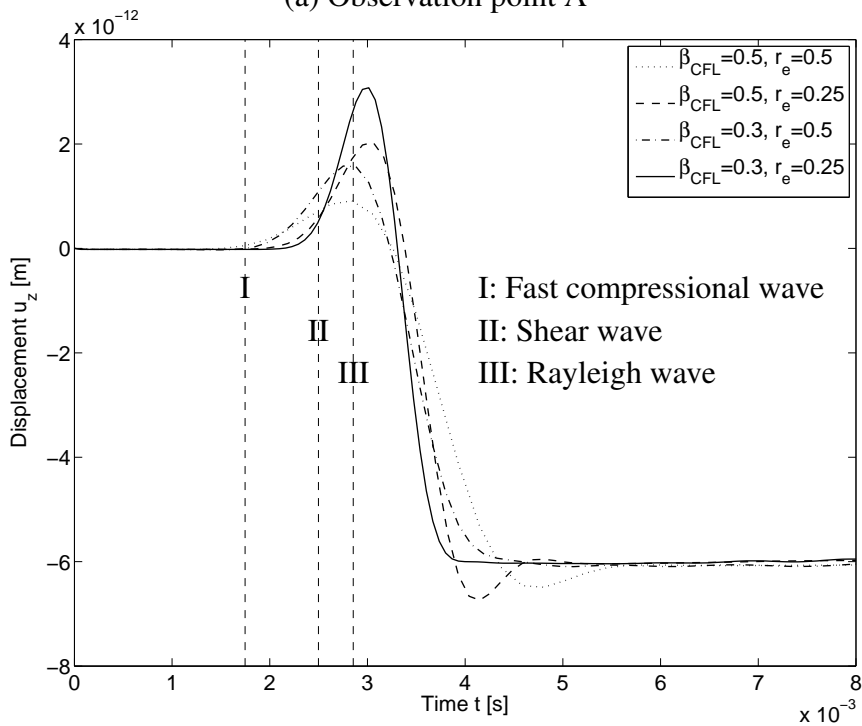
(b) Observation point B

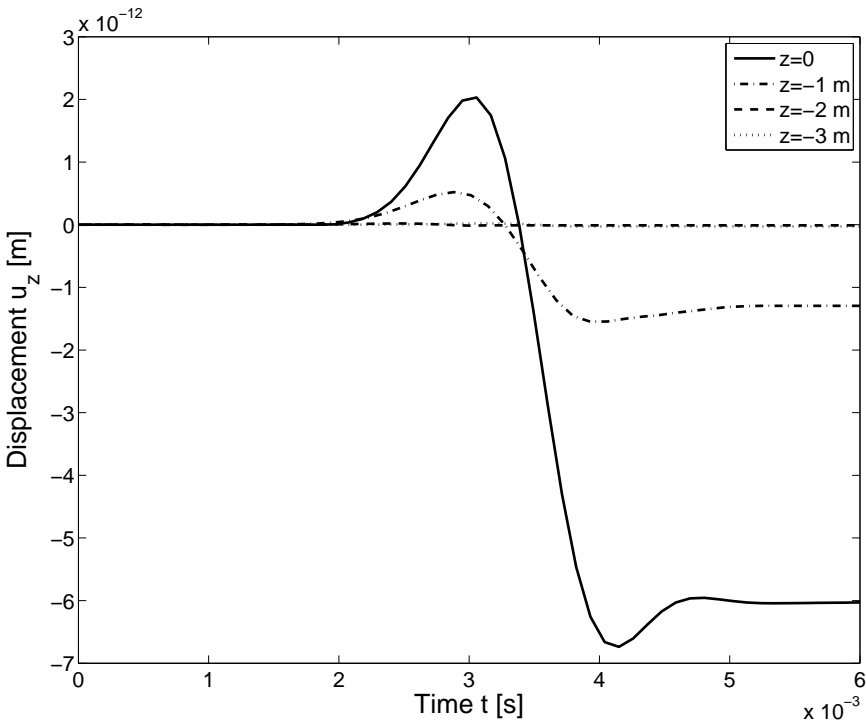Figure 6.12: Vertical displacement u_z versus time
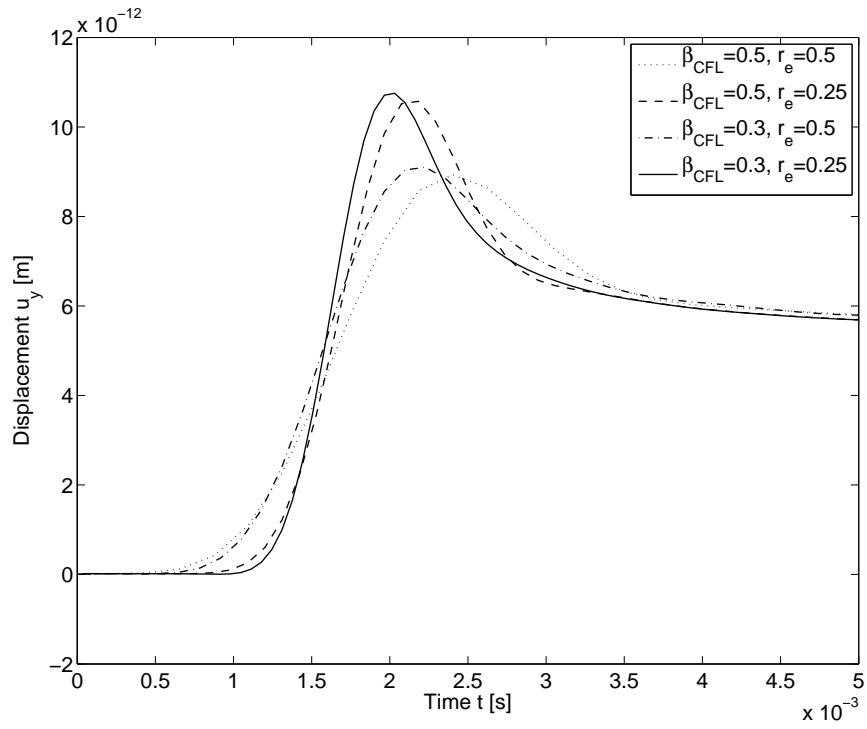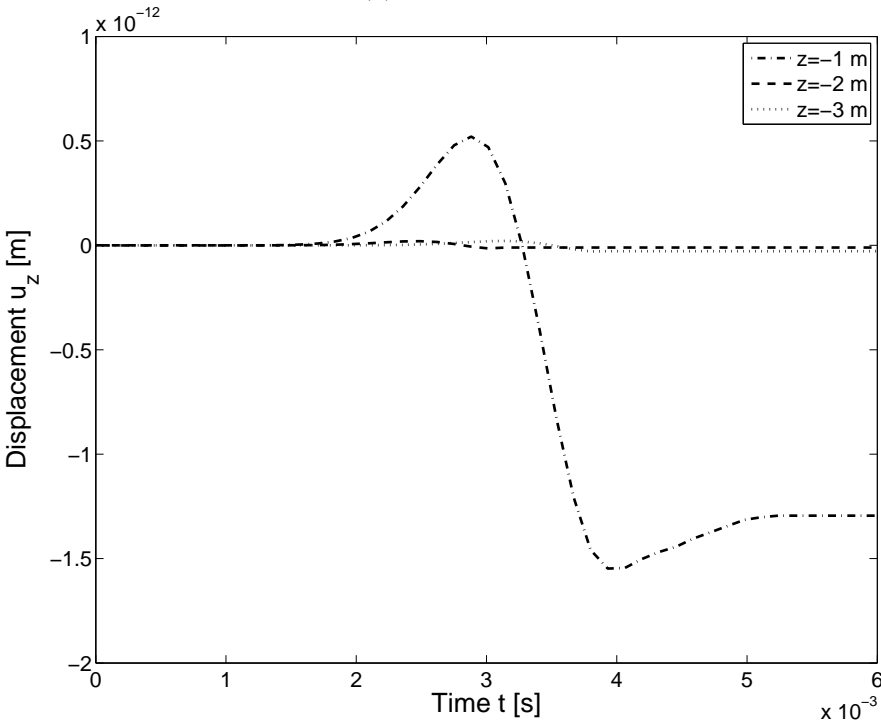
(a) Observation point A
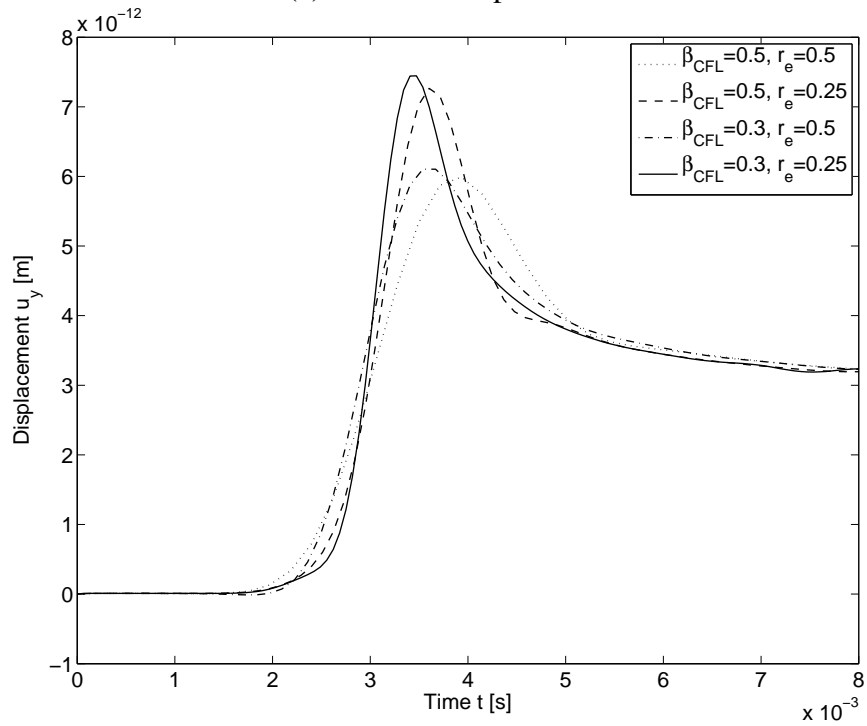
(b) Observation point B

Figure 6.13: Radial displacement u_y versus time

(a) Full scale

(b) Zoom

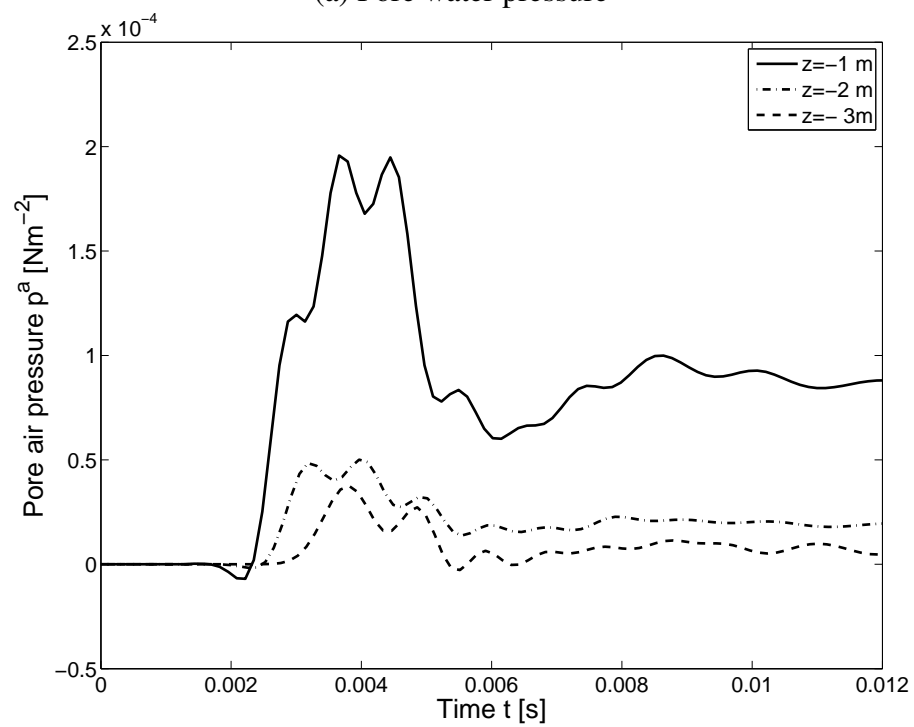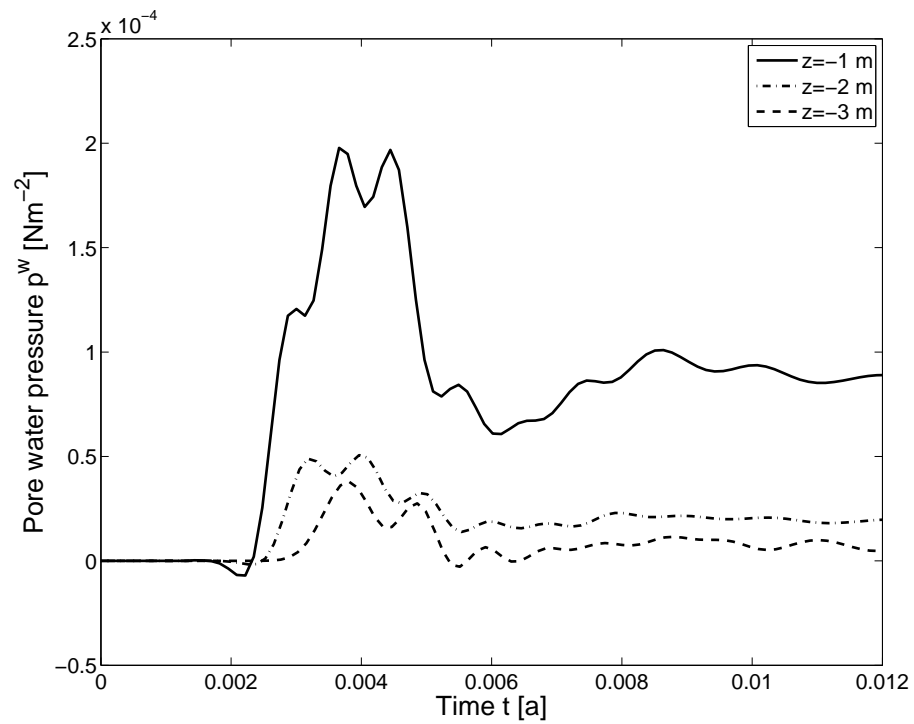Figure 6.14: Vertical displacement u_z versus time below point B with $\beta_{CFL} = 0.5$ and $r_e = 0.25$

(a) Pore water pressure

(b) Pore air pressure

Figure 6.15: Pore pressure p versus time below point B with $\beta_{CFL} = 0.5$ and $r_e = 0.25$

6.3 Vibration isolation via an open trench

The vibrations generated by various sources as rotating machines, traffic loads, etc. may induce nuisances in neighboring buildings. There are generally two methods to solve this problem, which is either to limit the vibrations transmitted to the environment, or to modify the propagation in the soil or the transmission to the structures [105]. Woods [129] and Richart et al. [97] analyzed the efficiency of various trench geometries of circular, rectangular, etc as an isolation system as show in Figure 6.16. A rotating machine is installed at the center of a circular trench and the amplitude s measured along various radii originating from the trench. The amplitude reduction is estimated by comparing the motion amplitude with the trench and the motion amplitude without the trench. The efficiency of the isolation system is assessed by estimating the amplitude reduction factor. The results show that low amplitude areas appear beyond the trench, whereas some areas may experience a significant motion amplification before the trench. The efficiency of the trench is found to be larger for deeper trenches since the maximum reduction is found to be larger than 90%.
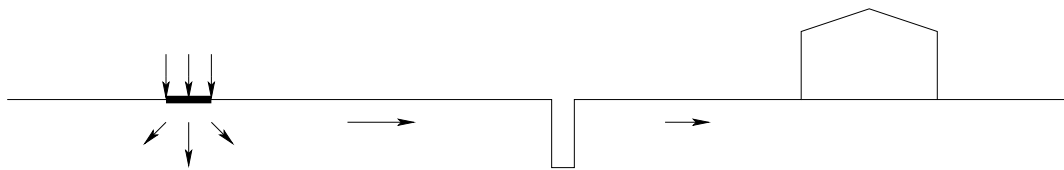
Figure 6.16: Vibratory isolation using an open trench

Recently, more and more researches are focusing on the extensive use of numerical techniques in 2D and 3D with FEM or BEM. Klein et al. [68] investigated several vibration isolation methods by using direct 3D Boundary Element Method. A comparison between numerical results and measured data has been finally presented for the case of vibration isolation by an open trench which was constructed for full–scale testing. The influence of different parameters on the amplitude reduction, due to the presence of a trench was studied. The influence of the track design and properties on the level of ground vibration due to a vehicle moving with subsonic speeds was examined by Andersen and Nielsen [8]. A coupled finite element–boundary element model of the track and subsoil was employed. The analyzes indicate that open trenches are more efficient than infilled trenches or soil stiffening–even at low frequencies. Karlström and Boström [64] studied the efficiency of trenches on the isolation of wave induced vibration propagation into the soil. Three cases were considered as the case without any isolation technique, the case involving two trenches and the case with one trench. The results shows that the mechanical waves seem to be trapped in the trench.

In this section, the vibration isolation of a partially saturated continuum using an open trench will be studied with the proposed BEM code. A Heaviside load is applied on the halfspace. Different geometric parameters of the trench are shown in Table 6.2. A square surface $(10\,\text{m} \times 10\,\text{m})$ is discretized with $r_e = 0.25\,\text{m}$ (see Figure 6.18). The loading area is applied a vertical total stress $\sigma_z = 1\,\text{Nm}^{-2}H(t)$ and the remaining surface is traction free. Both, the pore water and the pore air pressure are assumed to be zero all over the surface. The observation points A, B, and C (see Figure 6.17), are 0.25 m, 1 m and 4 m behind the trench along the center line of the trench, respectively.

Table 6.2: Geometry parameters

		D	L	W	H
Case 1	No trench	-	-	-	-
Case 2	Shallow open trench	1.0 m	1.0 m	0.5 m	1.0 m
Case 3	Deep open trench	1.0 m	1.0 m	0.5 m	3.0 m
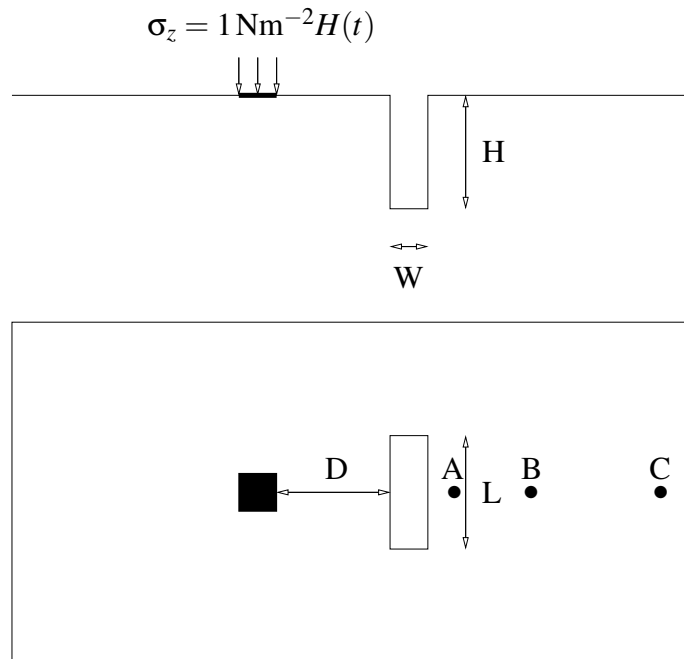
Figure 6.17: Geometry of the source isolation with an open trench

Both the vertical and horizontal responses can be a nuisance to people, sensitive laboratories and structures. For a easy comparison, the absolute values of the displacement

Loading area

(a) $r_e = 1/4\,\text{m}$, without trench

(b) $r_e = 1/4\,\text{m}$, with a trench ($H = 1\,\text{m}/3\,\text{m}$)

(c) $r_e = 1/4\,\text{m}$, with a trench ($H = 1\,\text{m}/3\,\text{m}$)
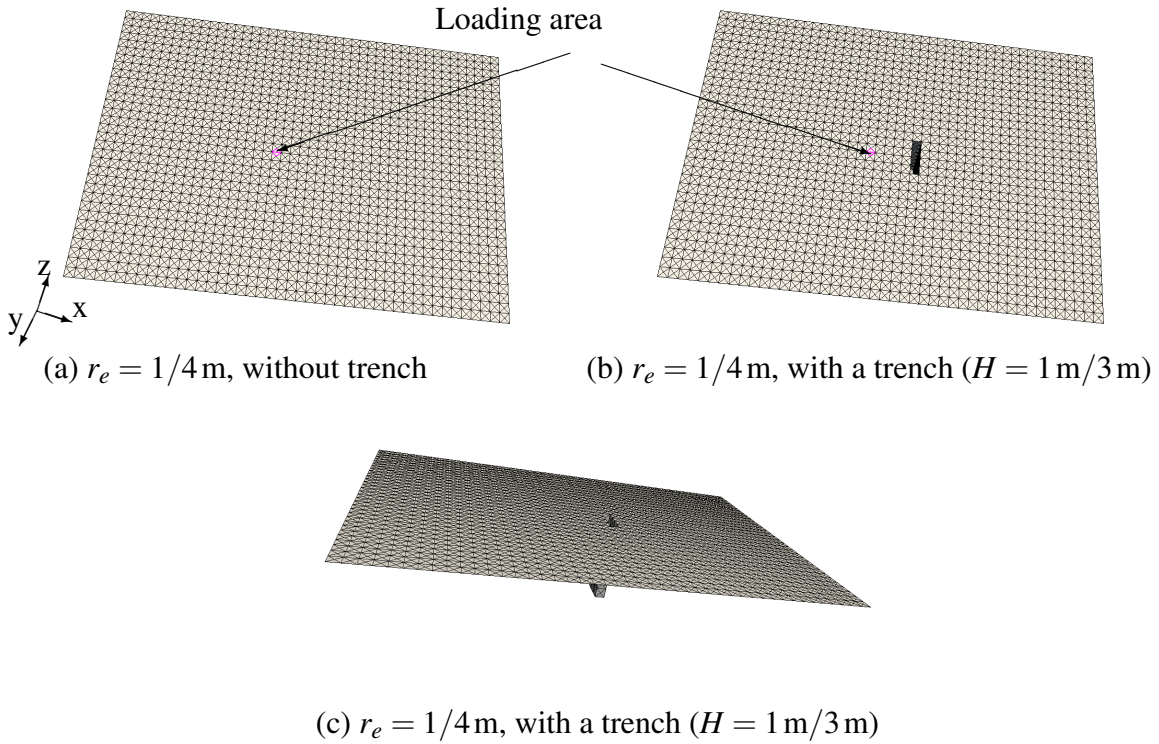
Figure 6.18: Different halfspace surface meshes

amplitude A_a are defined as

$$A_a = \sqrt{(u_{z_{max}} - u_{z_{min}})^2 + (u_{x_{max}} - u_{x_{min}})^2} \tag{6.3}$$

where $u_{z_{max}}$ and $u_{z_{min}}$ denote the maximum and the minimum vertical displacement of the observation point, $u_{x_{max}}$ and $u_{x_{min}}$ represent the maximum and minimum radial displacement of the observation point. Since all the observation points locate in the center line of the trench according to the load, u_y is zero.

In figure 6.19, the color pictures of the vertical and the radial displacement results u_z and u_x at $t \approx 0.0074\,\text{s}$ are given. The reflection surface wave can be observed clearly due to the open trench. It is also observed that the surface wave behind the trench is weaken at the given time.

In figure 6.20 and 6.21, the vertical and radial displacement u_z and u_x versus time are given at the point A, B and C respectively. The vibration isolation effects are obvious the peak amplitude will decrease behind the open trench, while the differences of the final "static" displacement value are not very large. This is caused by this finite depth trench which can be passed by the wave. At the observation point A, which is closest to the open trench, the isolation effect is the best. However, with increasing the distance between the observation
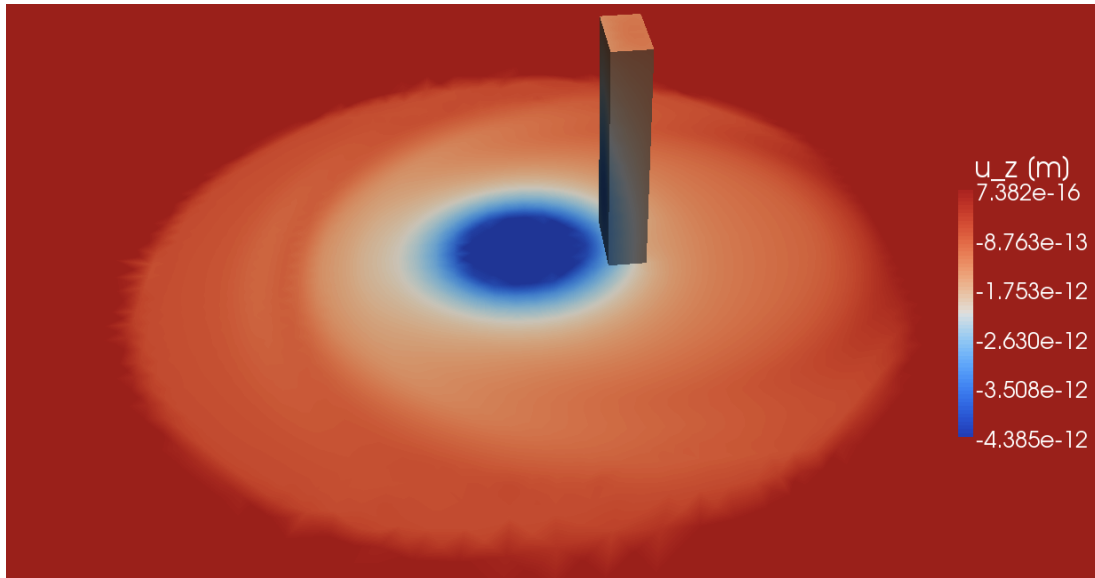
(a) Vertical displacement
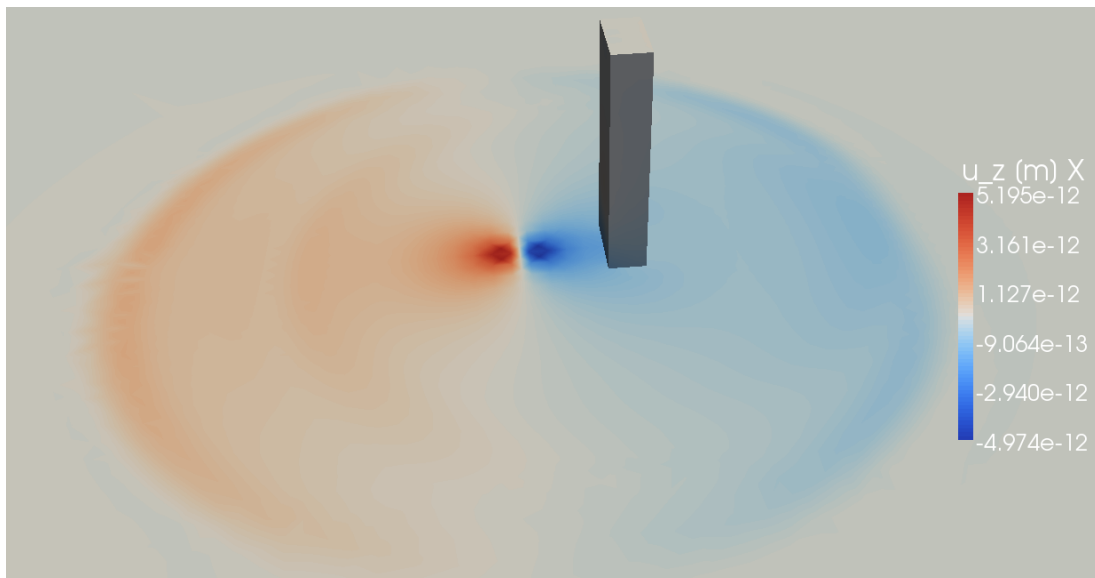
(b) Radial displacement

Figure 6.19: Vertical and radial displacement u_z and u_x distributions at $t \approx 0.0074\,\text{s}$ with the view point from below

point and the open trench, the isolation effect becomes worse, i.e., the amplitude reduction turns to be smaller, and the final static displacement may remain the same (see figure 6.20(c)).

For the vertical displacement, the magnitudes vary very little for both the shallow and the deep open trench, while for the radial displacement, the difference between the magnitudes is somehow larger. The behavior of the radial displacements is nearly the same as the vertical displacement. One can conclude that with a deeper open trench, the isolation effect is better. Physically, the open trench extends the distance between the load point and the observation point, and more energy can be dissipated during a longer traveling distance. This characteristic holds no matter the wave is traveling in a partially saturated medium or just in a simple elastic medium.

Based on the vertical and the radial displacement results at the observation points A, B and C, in Figure 6.22, more detailed comparisons are performed. First, the absolute values of the displacement amplitude A_a are calculated for each node along the center line behind the open trench as shown in figure 6.22(a). The amplitude reduction factor A_{rf} is also calculated with dividing A_a by the corresponding absolute displacement value without a trench in case 1. At the point which is 0.25 m behind the trench, the absolute value of the displacement amplitude A_a can drop from 3.5×10^{-12} m to 2.5×10^{-12} m with the deep open trench, and the amplitude reduction factors of the shallow and deep open trenches are about 1.30 and 1.42, respectively. At the point which is 4.25 m behind the trench, the absolute value of the displacement amplitude can drop from 1.75×10^{-12} m to 1.55×10^{-12} m with the deep open trench, and the amplitude reduction factors of the shallow and deep open trenches are about 1.155 and 1.16, respectively.

As mentioned before, with a finite depth trench, the wave will eventually pass by. In order to observe this process, some inner points below the surface are calculated in time domain. Besides, all the inner points locate in a $x-z$ plane at $y=0$. In figure 6.23, the color pictures of the vertical and the radial displacement at $t \approx 0.0022$ s, $t \approx 0.0031$ s, and $t \approx 0.0041$ s are shown. It is clear to see that before the arrival of the fast compressional wave at the bottom of the open trench, the wave is nearly blocked where behind the trench, the spread of the wave is hardly to see. Afterwards, the wave behind the trench can be observed at $t \approx 0.0031$ s and $t \approx 0.0041$ s.

A short conclusion for the vibration isolation with an open trench is that in order to obtain the best effect, the position of the open trench should be as close as possible to the object to be isolated. A deeper trench will produce a better isolation effect since the traveling distance of the wave will be longer. However, taking the soil as an example, a deeper trench means a more difficult maintaining work of the trench to keep the stability as well as the excavation and later back filling. A shallow trench but close enough to the object may be a viable solution, or by using an array of shallow trenches.
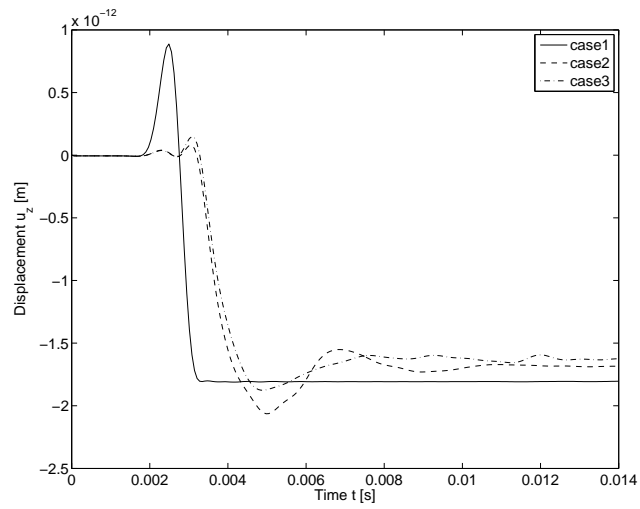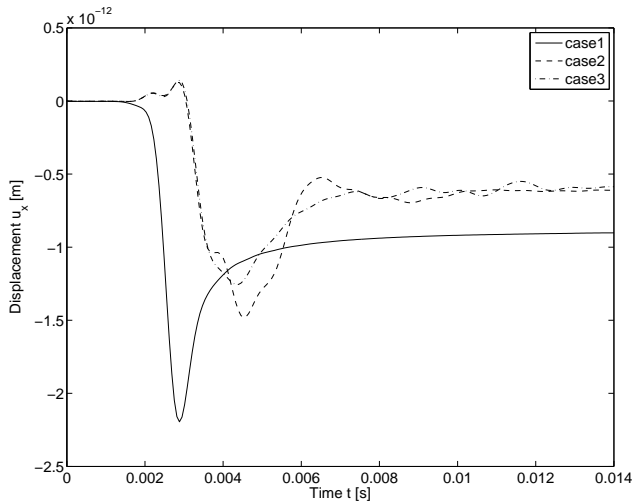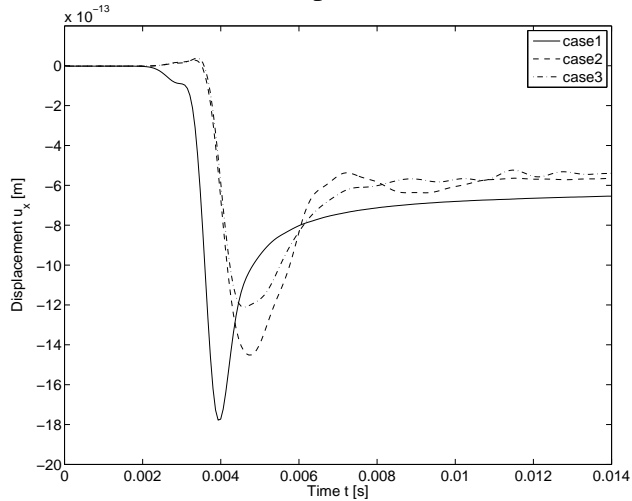
(a) At point A
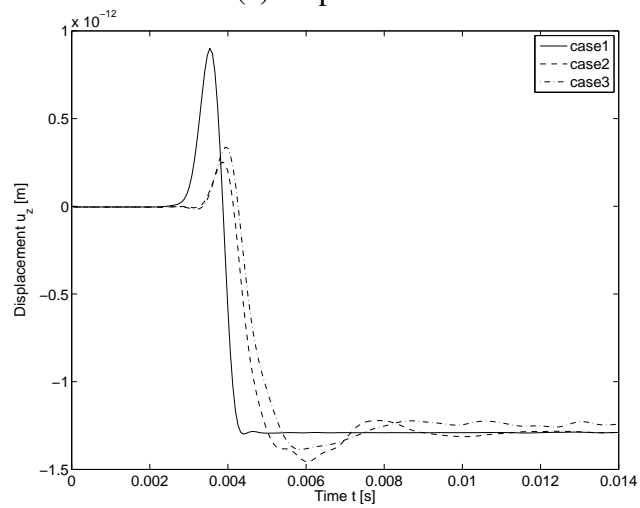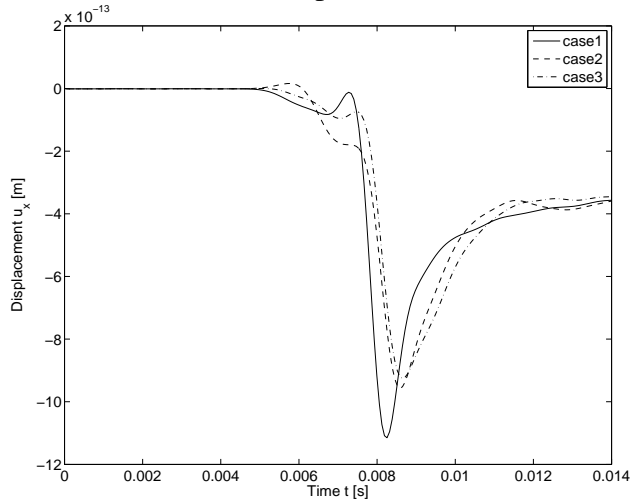

(b) At point B
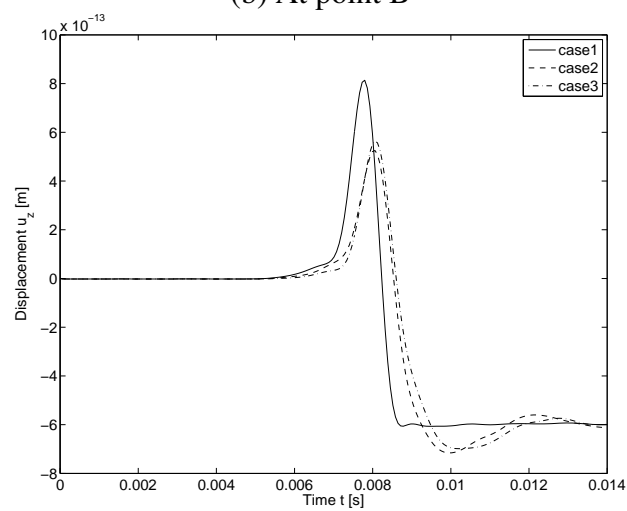
(c) At point C

Figure 6.20: Vertical displacement u_z versus time at different points
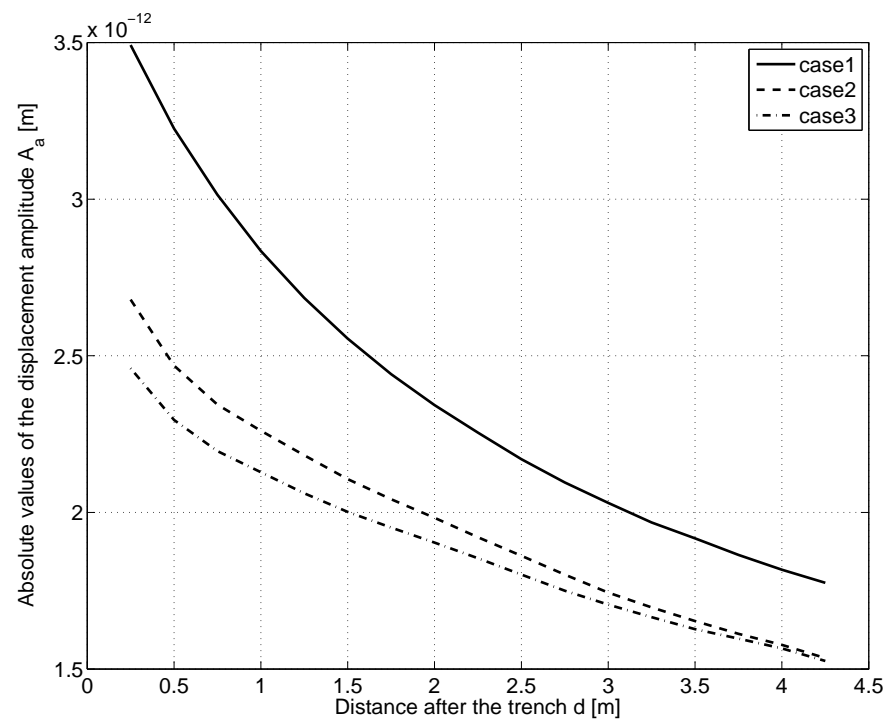
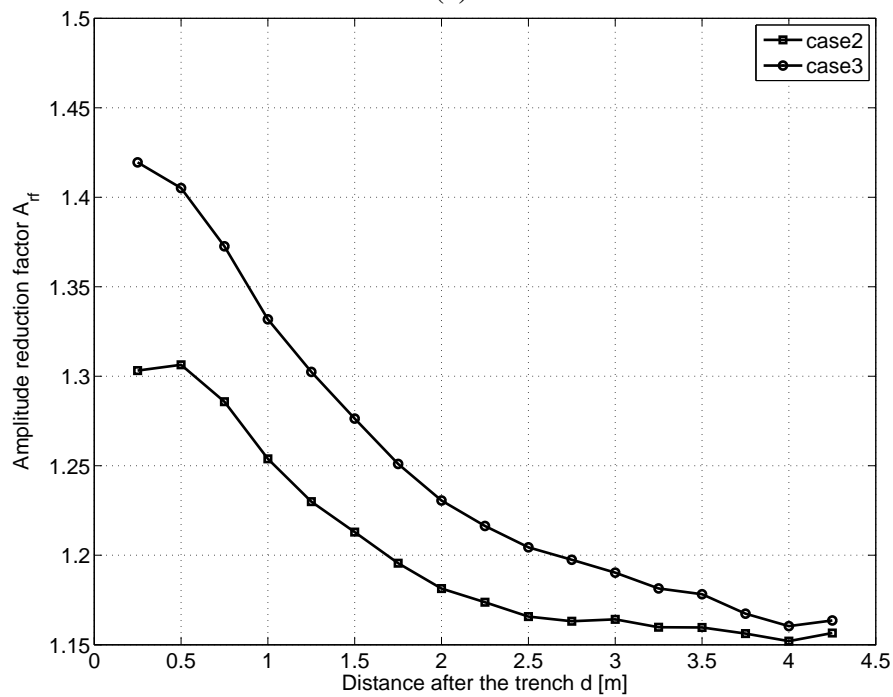(a) At point A

(b) At point B

(c) At point C

Figure 6.21: Radial displacement u_x versus time at different points

(a)

(b)

Figure 6.22: Absolute values of the displacement amplitude A_a distribution and the corresponding amplitude reduction factor A_{rf} distribution behind the trench
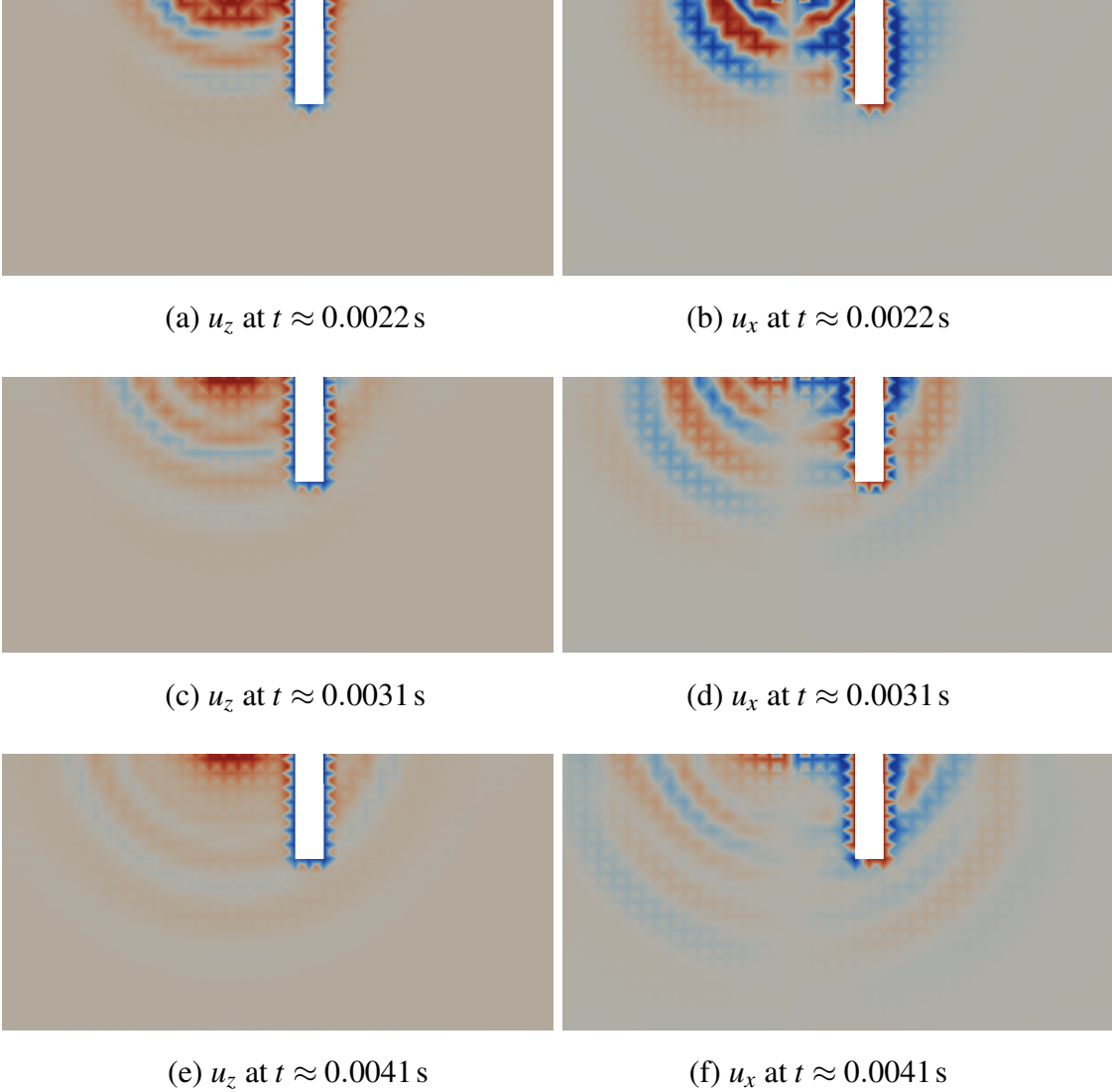
(a) u_z at $t \approx 0.0022\,\text{s}$ (b) u_x at $t \approx 0.0022\,\text{s}$

(c) u_z at $t \approx 0.0031\,\text{s}$ (d) u_x at $t \approx 0.0031\,\text{s}$

(e) u_z at $t \approx 0.0041\,\text{s}$ (f) u_x at $t \approx 0.0041\,\text{s}$

Figure 6.23: Color pictures of the vertical and the radial displacement below the surface

7 CONCLUSION

The main topic of this thesis is to establish a collocation boundary element method for partially saturated poroelasticity. This partially saturated poroelastic continuum is a mixture of three phases, the solid phase, the wetting fluid, and the non–wetting fluid. The solid phase has a skeleton formed structure, and the fluid exists in the voids distributed around the solid skeleton. Based on the set of balance equations and constitutive assumptions, the corresponding governing equations are derived. For the boundary element method, a linearized set of governing equations is preferable. With regard to this characteristic, the gradients of the porosity, the densities, and the saturation degree of the partially saturated media are neglected. By introducing the so called capillary pressure function, the part including the partial derivative of the saturation degree over the capillary pressure is transferred to some linear function which makes the governing equations suitable for the boundary element method. Because a closed form of the governing equations in time domain is not easy to obtain, for the unknown solid displacement and the two pore pressures, in this case, the Laplace transform is applied. Based on the experiment, different kinds of capillary pressure equation are known from the literature. In this thesis, the capillary pressure equation based on the Brooks and Corey [27] are introduced. Certainly other choices are possible and can be applied to the proposed formulation. In the following calculations and numerical examples, the parameters of Massilon sandstone are chosen.

Starting from a simple case, chapter 3 is devoted to the analytical solution of a one dimensional partially saturated poroelastic column. With corresponding boundary conditions, the one dimensional governing equations are obtained and used to derive the analytical solution. The necessity for this step consists in the verification of the proposed governing equations and being used for the validation of the subsequent boundary element results. For the one dimensional case, the governing equations are reduced to a set of scalar coupled ordinary differential equations. With the corresponding boundary conditions in the Laplace domain, the scalar coupled ordinary differential equations result in an eigenvalue problem by inserting the exponential ansatz for the unknown variables displacement and both pore pressures. The closed form analytical solution in the Laplace domain is obtained by solving the system of linear equations with regard to different types of boundary conditions. Prior to the discussion of the displacement and pore pressure results, the wave velocity is investigated. As formulated in the governing equations, there exist three different compressional waves, the fast compressional wave and the second and the third slow compressional wave. The shear wave disappears in the one dimensional case. By comparing to the Gassmann's prediction and Murphy's experimental results, the fast compressional wave velocity coincides very well for different water saturations. The second

and the third compressional wave velocities also match well with Wei and Muraleetharan [120]'s results as well as the attenuation results. For the displacement and pore pressure results versus the frequency, more eigenfrequencies can be seen in a given frequency range for the nearly saturated and saturated cases than those of partially saturated cases. In order to calculate the time domain results, the Convolution Quadrature Method is applied. With a limiting process of the water saturation S_w to nearly one, both the frequency and time domain results are investigated and validated by comparing with the analytical one dimensional saturated poroelastic column results. Besides, by eliminating the viscosity of the fluid, the second and third slow compressional waves are detected.

Different from elastodynamic problems, the differential operator for partially saturated poroelasticity is not self–adjoint. To obtain the fundamental solutions, the coupled differential equations have to be solved with a Dirac distribution as right hand side, and following Hörmander's method, finding them is reduced to find a scalar function. The fundamental solutions for partially saturated poroelasticity have nine entries in the matrix, i.e., displacement, pore pressure, and coupling parts of the fundamental solutions. The validation of the fundamental solutions is also done by a limiting process of the water saturation to the nearly saturated case and an comparison with the fundamental solutions of saturated poroelasticity.

Once the fundamental solutions are obtained, the boundary integral equations can be established based on the weighted residuals method as well as the collocation method. However, before the final step, it is necessary to get a knowledge of the singular behavior of the fundamental solutions. A series expansion with respect to the distance between the field and the load point is applied to determine the singularity. As anticipated, the singularity shows similarity compared with the fundamental solutions of poroelasticity. Of all the entries of the fundamental solutions, only weak and strong singularities exist where the strong singularities come from the traction and flux fundamental solutions. The strong singular parts are regularized with the method of integrating by parts. Since only the Laplace domain fundamental solutions are deduced, the time domain boundary element formulation is established based on the convolution quadrature method. The numerical implementation is accomplished by using the open source C++ BEM library HyENA.

Three numerical examples are presented with the proposed boundary element formulation. Due to the heavy computing work, only the case $S_w = 0.90$ is considered. First of all, the code is validated by calculating a three dimensional partially saturated poroelastic column and comparing with the proposed one dimensional analytical solution. Two numerical parameters, the time step size and the mesh size are studied. For partially saturated poroelasticity, the stability of the time domain numerical results is very good. A partially saturated poroelastic halfspace is also studied for investigating the plane waves, i.e., the fast compressional wave, the shear wave and the Rayleigh wave. The results show that with proper numerical parameters, the numerical results can be improved a lot. The last example is an attempt for the application of the vibration isolation problem. An open

trench is modeled in a halfspace with an impulse before the trench. The displacements behind the trench at different observation points are calculated as well as the amplitude.

At last, some deficiencies of the proposed method must be pointed out. According to the regularization method, a closed domain is desirable. This contradicts with the half-space example. Nevertheless, the error introduced is such small that the results are still acceptable. This problem could be solved by applying infinite elements coupled with the boundary element method, or by using proper integral equations. Although the dimensionless variables are introduced, still for the extreme cases, when the saturation degree is extremely close to one or zero, an numercial instability will happen because of the bad condition number, and this problem can hardly be solved. But, it must be mentioned that these extreme values are highly academic. As shown in the former chapters, due to the complexity of the fundamental solutions, the problem to be solved is usually quite time consuming and needs considerable memory. For such complex problem, the so called fast boundary element method could be a solution as the Adaptive Cross Approximation, fast multipole method and clustering computing techniques.

A APPENDIX

A.1 Abreviations

A.1.1 Abreviations for the one dimensional analytical solutions

In section 3.1, the following abbreviations are used:

$$B_1 = K + \frac{4}{3}G$$

$$B_2 = \rho - \beta S_w \rho_w - \gamma S_a \rho_a$$

$$B_3 = (\alpha - \beta)S_w$$

$$B_4 = (\alpha - \gamma)S_a$$

$$B_5 = \zeta S_{ww} S_w + \frac{n}{K_w} S_w - S_u$$

$$B_6 = \frac{\beta S_w}{\rho_w}$$

$$B_7 = \zeta S_{aa} S_w + S_u$$

$$B_8 = \zeta S_{ww} S_a + S_u$$

$$B_9 = \zeta S_{aa} S_a + \frac{n}{K_a} S_a - S_u$$

$$B_{10} = \frac{\gamma S_a}{\rho_a}$$

$$C_1 = B_1 B_6 B_{10}$$

$$C_2 = -(B_1 B_5 B_{10} + B_1 B_6 B_9 + B_2 B_6 B_{10} + B_3^2 B_{10} + B_4^2 B_6)$$

$$C_3 = B_1(B_5 B_9 - B_7 B_8) + B_2(B_5 B_{10} + B_6 B_9) - B_3 B_4(B_7 + B_8) + B_3^2 B_9 + B_4^2 B_5$$

$$C_4 = B_2(B_7 B_8 - B_5 B_9)$$

$$N_1 = -\frac{C_2}{3C_1}$$

$$N_2 = \frac{\sqrt[3]{2}}{N_3}$$

$$N_3 = \sqrt[3]{-2C_2^3 + 9C_1 C_2 C_3 - 27C_1^2 C_4 + \sqrt{4(-C_2^2 + 3C_1 C_3)^3 + (-2C_2^3 + 9C_1 C_2 C_3 - 27C_1^2 C_4)^2}}$$

A.1.2 Abreviations for the fundamental solutions

In section 4.3, the following abbreviations are used:

$$r_1 = s^{-2}(a_1 a_7 a_{11})$$

$$r_2 = -(a_1 a_7 a_{10} + a_1 a_6 a_{11} + a_2 a_7 a_{11})$$

$$r_3 = s^2(-a_1 a_8 a_9 + a_1 a_6 a_{10} + a_2 a_7 a_{10} + a_2 a_6 a_{11})$$

$$r_4 = s^4(a_2 a_8 a_9 - a_2 a_6 a_{10})$$

$$r_5 = s^{-2}(-a_3 a_7 a_{11})$$

$$r_6 = a_5^2 a_7 + a_3 a_7 a_{10} + a_4^2 a_{11} + a_3 a_6 a_{11}$$

$$r_7 = s^2(-a_5^2 a_6 - a_4 a_5 a_8 - a_4 a_5 a_9 + a_3 a_8 a_9 - a_4^2 a_{10} - a_3 a_6 a_{10})$$

$$r_8 = -a_1 a_4 a_{11}$$

$$r_9 = s^2(a_1 a_5 a_8 + a_1 a_4 a_{10} + a_2 a_4 a_{11})$$

$$r_{10} = s^4(-a_2 a_5 a_8 - a_2 a_4 a_{10})$$

$$r_{11} = -a_1 a_5 a_7$$

$$r_{12} = s^2(a_1 a_5 a_6 + a_2 a_5 a_7 + a_1 a_4 a_9)$$

$$r_{13} = s^4(-a_2 a_5 a_6 - a_2 a_4 a_9)$$

$$r_{14} = -s^{-1} a_1 a_4 a_{11}$$

$$r_{15} = s(a_1 a_5 a_9 + a_1 a_4 a_{10} + a_2 a_4 a_{11})$$

$$r_{16} = s^3(-a_2 a_5 a_9 - a_2 a_4 a_{10})$$

$$r_{17} = -s^{-1} a_1 a_5 a_7$$

$$r_{18} = s(a_1 a_5 a_6 + a_2 a_5 a_7 + a_1 a_4 a_8)$$

$$r_{19} = s^3(-a_2 a_5 a_6 - a_2 a_4 a_8)$$

$$r_{20} = s^{-1} a_1 a_{11}(a_1 + a_3)$$

$$r_{21} = s(-a_1 a_5^2 - a_1^2 a_{10} - a_1 a_3 a_{10} - 2a_1 a_2 a_{11} - a_2 a_3 a_{11})$$

$$r_{22} = s^3(a_2 a_5^2 + 2a_1 a_2 a_{10} + a_2 a_3 a_{10} + a_2^2 a_{11})$$

$$r_{23} = s^5(-a_2^2 a_{10})$$

$$r_{24} = s(a_1 a_4 a_5 - a_1^2 a_9 - a_1 a_3 a_9)$$

$$r_{25} = s^3(-a_2 a_4 a_5 + 2a_1 a_2 a_9 + a_2 a_3 a_9)$$

$$r_{26} = s^5(-a_2^2 a_9)$$

$$r_{27} = s(a_1 a_4 a_5 - a_1^2 a_8 - a_1 a_3 a_8)$$

$$r_{28} = s^3(-a_2 a_4 a_5 + 2a_1 a_2 a_8 + a_2 a_3 a_8)$$

$$r_{29} = s^5(-a_2^2 a_8)$$

$$r_{30} = s^{-1}a_1a_7(a_1 + a_3)$$
$$r_{31} = s(-a_1a_4^2 - a_1^2a_6 - a_1a_3a_6 - 2a_1a_2a_7 - a_2a_3a_7)$$
$$r_{32} = s^3(a_2a_4^2 + 2a_1a_2a_6 + a_2a_3a_6 + a_2^2a_7)$$
$$r_{33} = s^5(-a_2^2a_6)$$

A.2 Fast compressional wave velocities of the Massilon sandstone

The theoretical fast compressional wave velocity v_p^G is calculated based on the Gassmann equation

$$K^* = K + \frac{\alpha^2}{\dfrac{\alpha - n}{K_s} + n(\dfrac{S_w}{K_w} + \dfrac{S_a}{K_a})}$$

$$v_p^G = \sqrt{\frac{K^* + \dfrac{4}{3}G}{\rho}} \quad,$$

where it can also be calculated according to (3.18a) with a given frequency value named as v_{p1}, which has been verified in section 3.2 that $v_{p1} = v_p^G$.

For Massilon sandstone, the pore size distribution index ϑ is set to 1.5, the residual water saturation S_{rw} is set to 0, and the air entry saturation S_{ra} is set to 1.

Table A.1: Fast compressional wave velocities of the Massilon sandstone

Water saturation S_w	Fast compressional wave velocity	Value	Unit
0.5	v_p^G	1168.12	m/s
0.6	v_p^G	1162.01	m/s
0.7	v_p^G	1156.02	m/s
0.8	v_p^G	1150.20	m/s
0.9	v_p^G	1144.76	m/s
0.95	v_p^G	1142.72	m/s
0.99	v_p^G	1147.32	m/s
0.999	v_p^G	1217.77	m/s
0.9999	v_p^G	1595.09	m/s
0.99999	v_p^G	2042.81	m/s

A.3 Convolution Quadrature Method

The Convolution Quadrature Method developed by Lubich [74, 75] numerically approximates a convolution integral as

$$y(t) = \int_0^t f(t-\tau)g(\tau))d\tau \rightarrow y(n\Delta t) = \sum_{k=0}^n \omega_{n-k}(\hat{f}, \Delta t)g(k\Delta t) \quad n = 0, 1, ..., N \quad \text{(A.2)}$$

by a quadrature rule whose weights are determined by the Laplace transformed function $\hat{f}$ and a linear multistep method. Here, a brief overview of the method is given.

In formula (A.2), the time t is divided in N equal steps Δt. The weights $\omega_n(\hat{f}, \Delta t)$ are the coefficients of the power series

$$\hat{f}\left(\frac{\gamma(z)}{\Delta t}\right) = \sum_{n=0}^{\infty} \omega_n(\hat{f}, \Delta t)z^n \quad \text{(A.3)}$$

with the complex variable z. The coefficients of a power series are usually calculated with Cauchy's integral formula. After a polar coordinate transformation, this integral is approximated by a trapezoidal rule with L equal steps $2\pi/L$. This leads to

$$\omega_n(\hat{f}, \Delta t) = \frac{1}{2\pi i} \int_{|z|=\mathcal{R}} \hat{f}\left(\frac{\gamma(z)}{\Delta t}\right) z^{-n-1}dz \approx \frac{\mathcal{R}^{-n}}{L} \sum_{\ell=0}^{L-1} \hat{f}\left(\frac{\gamma(\mathcal{R}e^{i\ell\frac{2\pi}{L}})}{\Delta t}\right) e^{-in\ell\frac{2\pi}{L}} \quad , \quad \text{(A.4)}$$

where $\mathcal{R}$ is the radius of a circle in the domain of analyticity of $\hat{f}(z)$.

The function $\gamma(z)$ is the quotient of the characteristic polynomials of the underlying multistep method. For hyperbolic problems only A–stable methods are admissible, the most often used methods being the backward difference formulas of order 1 (BDF 1) and order 2 (BDF 2) for which

$$\gamma(z) = 1 - \gamma \quad \text{(BDF 1)} \quad \text{(A.5a)}$$

$$\gamma(z) = 1.5 - 2z + 0.5z^2 \quad \text{(BDF 2)} \quad . \quad \text{(A.5b)}$$

For the convergence of the linear multistep based convolution quadrature, the proof can be found in [76]. Because of the restriction to A–stable linear multistep methods, the highest order attainable is order 2. To achieve higher orders of convergence one has to turn to Runge–Kutta methods such as Radau IIA and Lobatto IIIC methods. For a detailed introduction to Runge–Kutta based CQM see [10, 29].

If one assumes that the values of $\hat{f}(z)$ in (A.4) are computed with an error bounded by ϵ, then the choice $L = N$ and $\mathcal{R}^N = \sqrt{\epsilon}$ yields an error in ω_n of size $\mathcal{O}(\sqrt{\epsilon})$. Several tests conducted in [103] lead to the conclusion that the parameter $\epsilon = 10^{-10}$ is the best choice for the kind of functions. The assumption $L = N$ results in N^2 coefficients $\omega_n(\Delta t)$ to be calculated. Due to the exponential function at the end of formula (A.4) this can be done very fast using the technique of the Fast Fouier Transformation (FFT).

A.4 Partially Saturated Poroelastic Fundamental Solutions

The explicit expressions of the partially saturated poroelastodynamic fundamental solutions for the unknowns solid displacement and pore pressure are

$$\hat{U}_{ij}^{ss} = \frac{w_0}{4\pi r^3} \sum_{m=1}^{4} w_m \left[r_{,i} r_{,j} R_m (\lambda_m^2 r^2 + 3\lambda_m r + 3) + \delta_{ij} (S_m r^2 - R_m \lambda_m r - R_m) \right] \quad \text{(A.6a)}$$

$$\hat{P}_j^{sw} = -\frac{w_0 r_{,j}}{4\pi r^2} \sum_{m=1}^{4} w_m (\lambda_m^4 r_{14} + \lambda_m^2 r_{15} + r_{16})(1 + \lambda_m r) \quad \text{(A.6b)}$$

$$\hat{P}_j^{sa} = -\frac{w_0 r_{,j}}{4\pi r^2} \sum_{m=1}^{4} w_m (\lambda_m^4 r_{17} + \lambda_m^2 r_{18} + r_{19})(1 + \lambda_m r) \quad \text{(A.6c)}$$

$$\hat{U}_i^{ws} = -\frac{w_0 r_{,i}}{4\pi r^2} \sum_{m=1}^{4} w_m (\lambda_m^4 r_8 + \lambda_m^2 r_9 + r_{10})(1 + \lambda_m r) \quad \text{(A.6d)}$$

$$\hat{P}^{ww} = \frac{w_0}{4\pi r} \sum_{m=1}^{4} w_m (\lambda_m^6 r_{20} + \lambda_m^4 r_{21} + \lambda_m^2 r_{22} + r_{23}) \quad \text{(A.6e)}$$

$$\hat{P}^{wa} = \frac{w_0}{4\pi r} \sum_{m=1}^{4} w_m (\lambda_m^4 r_{27} + \lambda_m^2 r_{28} + r_{29}) \quad \text{(A.6f)}$$

$$\hat{U}_i^{as} = -\frac{w_0 r_{,i}}{4\pi r^2} \sum_{m=1}^{4} w_m (\lambda_m^4 r_{11} + \lambda_m^2 r_{12} + r_{13})(1 + \lambda_m r) \quad \text{(A.6g)}$$

$$\hat{P}^{aw} = \frac{w_0}{4\pi r} \sum_{m=1}^{4} w_m (\lambda_m^4 r_{24} + \lambda_m^2 r_{25} + r_{26}) \quad \text{(A.6h)}$$

$$\hat{P}^{aa} = \frac{w_0}{4\pi r} \sum_{m=1}^{4} w_m (\lambda_m^6 r_{30} + \lambda_m^4 r_{31} + \lambda_m^2 r_{32} + r_{33}) \quad , \quad \text{(A.6i)}$$

where

$$R_m = \lambda_m^4 r_5 + \lambda_m^2 r_6 + r_7 \ (m = 1, 2, 3, 4)$$

$$S_m = \lambda_m^6 (r_1 - r_5) + \lambda_m^4 (r_2 - r_6) + \lambda_m^2 (r_3 - r_7) + r_4 \ (m = 1, 2, 3, 4)$$

$$w_0 = \frac{\rho_w \rho_a s^2}{G \beta \gamma S_w S_a (K + 4G/3)}$$

$$w_m = \frac{e^{-\lambda_m r}}{\prod_{j=1, j \neq m}^{4} (\lambda_m^2 - \lambda_j^2)} \quad .$$

The traction and flux fundamental solutions are

$$\hat{T}_{ij}^{ss} = \left\{ \left[(K - \frac{2}{3}G) \hat{U}_{kj,k}^{ss} + \alpha s (S_w \hat{P}_j^{sw} + S_a \hat{P}_j^{sa}) \right] \delta_{il} + G(\hat{U}_{ij,l}^{ss} + \hat{U}_{lj,i}^{ss}) \right\} n_l \quad \text{(A.7a)}$$

$$\hat{T}_i^{ws} = \left\{ \left[(K - \frac{2}{3}G)\hat{U}_{k,k}^{ws} + \alpha s (S_w \hat{P}^{ww} + S_a \hat{P}^{wa}) \right] \delta_{il} + G(\hat{U}_{i,l}^{ws} + \hat{U}_{l,i}^{ws}) \right\} n_l \qquad \text{(A.7b)}$$

$$\hat{T}_i^{as} = \left\{ \left[(K - \frac{2}{3}G)\hat{U}_{k,k}^{as} + \alpha s (S_w \hat{P}^{aw} + S_a \hat{P}^{aa}) \right] \delta_{il} + G(\hat{U}_{i,l}^{as} + \hat{U}_{l,i}^{as}) \right\} n_l \qquad \text{(A.7c)}$$

$$\hat{Q}_j^{sw} = \frac{\beta S_w}{\rho_w s} (\hat{P}_{j,i}^{sw} - \rho_w s \hat{U}_{ji}^{ss}) n_i \qquad \text{(A.7d)}$$

$$\hat{Q}^{ww} = \frac{\beta S_w}{\rho_w s} (\hat{P}_{,j}^{ww} - \rho_w s \hat{U}_j^{ws}) n_j \qquad \text{(A.7e)}$$

$$\hat{Q}^{aw} = \frac{\beta S_w}{\rho_w s} (\hat{P}_{,j}^{aw} - \rho_w s \hat{U}_j^{as}) n_j \qquad \text{(A.7f)}$$

$$\hat{Q}_j^{sa} = \frac{\gamma S_a}{\rho_a s} (\hat{P}_{j,i}^{sa} - \rho_a s \hat{U}_{ji}^{ss}) n_i \qquad \text{(A.7g)}$$

$$\hat{Q}^{wa} = \frac{\gamma S_a}{\rho_a s} (\hat{P}_{,j}^{wa} - \rho_a s \hat{U}_j^{ws}) n_j \qquad \text{(A.7h)}$$

$$\hat{Q}^{aa} = \frac{\gamma S_a}{\rho_a s} (\hat{P}_{,j}^{aa} - \rho_a s \hat{U}_j^{as}) n_j \quad , \qquad \text{(A.7i)}$$

where

$$\hat{U}_{kj,k}^{ss} \delta_{il} n_l = - \frac{w_0 r_{,j} n_i}{4\pi r^2} \sum_{m=1}^{4} w_m (1 + \lambda_m r)(S_m + \lambda_m^2 R_m) \qquad \text{(A.8a)}$$

$$\hat{U}_{k,k}^{ws} \delta_{il} n_l = \frac{w_0 n_i}{4\pi r} \sum_{m=1}^{4} w_m (\lambda_m^6 r_8 + \lambda_m^4 r_9 + \lambda_m^2 r_{10}) \qquad \text{(A.8b)}$$

$$\hat{U}_{k,k}^{as} \delta_{il} n_l = \frac{w_0 n_i}{4\pi r} \sum_{m=1}^{4} w_m (\lambda_m^6 r_{11} + \lambda_m^4 r_{12} + \lambda_m^2 r_{13}) \qquad \text{(A.8c)}$$

$$(\hat{U}_{ij,l}^{ss} + \hat{U}_{lj,i}^{ss}) n_l = \frac{w_0 (r_{,i} n_j + \delta_{ij} r_{,n})}{4\pi r^4} \sum_{m=1}^{4} w_m \left[2R_m (\lambda_m^2 r^2 + 3\lambda_m r + 3) - r^2 (1 + \lambda_m r) S_m \right]$$

$$+ \frac{w_0 r_{,j} n_i}{2\pi r^4} \sum_{m=1}^{4} w_m R_m (\lambda_m^2 r^2 + 3\lambda_m r + 3)$$

$$- \frac{w_0 r_{,i} r_{,j} r_{,n}}{2\pi r^4} \sum_{m=1}^{4} w_m R_m (\lambda_m^3 r^3 + 6\lambda_m^2 r^2 + 15\lambda_m r + 15) \qquad \text{(A.8d)}$$

$$(\hat{U}_{i,l}^{ws} + \hat{U}_{l,i}^{ws}) n_l = \frac{w_0 r_{,i} r_{,n}}{2\pi r^3} \sum_{m=1}^{4} w_m (\lambda_m^2 r^2 + 3\lambda_m r + 3)(\lambda_m^4 r_8 + \lambda_m^2 r_9 + r_{10})$$

$$- \frac{w_0 n_i}{2\pi r^3} \sum_{m=1}^{4} w_m (1 + \lambda_m r)(\lambda_m^4 r_8 + \lambda_m^2 r_9 + r_{10}) \qquad \text{(A.8e)}$$

$$(\hat{U}_{i,l}^{as} + \hat{U}_{l,i}^{as})n_l = \frac{w_0 r_{,i} r_{,n}}{2\pi r^3} \sum_{m=1}^{4} w_m(\lambda_m^2 r^2 + 3\lambda_m r + 3)(\lambda_m^4 r_{11} + \lambda_m^2 r_{12} + r_{13})$$

$$- \frac{w_0 n_i}{2\pi r^3} \sum_{m=1}^{4} w_m(1 + \lambda_m r)(\lambda_m^4 r_{11} + \lambda_m^2 r_{12} + r_{13})$$

(A.8f)

$$\hat{P}_{j,i}^{sw} n_i = \frac{w_0 r_{,j} r_{,n}}{4\pi r^3} \sum_{m=1}^{4} w_m(\lambda_m^2 r^2 + 3\lambda_m r + 3)(\lambda_m^4 r_{14} + \lambda_m^2 r_{15} + r_{16})$$

$$- \frac{w_0 n_{,j}}{4\pi r^3} \sum_{m=1}^{4} w_m(1 + \lambda_m r)(\lambda_m^4 r_{14} + \lambda_m^2 r_{15} + r_{16})$$

(A.8g)

$$\hat{P}_{j,i}^{sa} n_i = \frac{w_0 r_{,j} r_{,n}}{4\pi r^3} \sum_{m=1}^{4} w_m(\lambda_m^2 r^2 + 3\lambda_m r + 3)(\lambda_m^4 r_{17} + \lambda_m^2 r_{18} + r_{19})$$

$$- \frac{w_0 n_{,j}}{4\pi r^3} \sum_{m=1}^{4} w_m(1 + \lambda_m r)(\lambda_m^4 r_{17} + \lambda_m^2 r_{18} + r_{19})$$

(A.8h)

$$\hat{P}_{,j}^{wa} n_j = - \frac{w_0 r_{,n}}{4\pi r^2} \sum_{m=1}^{4} w_m(1 + \lambda_m r)(\lambda_m^4 r_{27} + \lambda_m^2 r_{28} + r_{29})$$

(A.8i)

$$\hat{P}_{,j}^{aw} n_j = - \frac{w_0 r_{,n}}{4\pi r^2} \sum_{m=1}^{4} w_m(1 + \lambda_m r)(\lambda_m^4 r_{24} + \lambda_m^2 r_{25} + r_{26})$$

(A.8j)

$$\hat{P}_{,j}^{ww} n_j = - \frac{w_0 r_{,n}}{4\pi r^2} \sum_{m=1}^{4} w_m(1 + \lambda_m r)(\lambda_m^6 r_{20} + \lambda_m^4 r_{21} + \lambda_m^2 r_{22} + r_{23})$$

(A.8k)

$$\hat{P}_{,j}^{aa} n_j = - \frac{w_0 r_{,n}}{4\pi r^2} \sum_{m=1}^{4} w_m(1 + \lambda_m r)(\lambda_m^6 r_{30} + \lambda_m^4 r_{31} + \lambda_m^2 r_{32} + r_{33}) \quad .$$

(A.8l)

LIST OF FIGURES

119

LIST OF TABLES

REFERENCES

[1] M. Abramowitz and I. A. Stegun. *Handbook of Mathematical Functions*. Dover, 1972.

[2] G. D. Aitchison. *Moisture Equilibria and Moisture Changes in Soils Beneath Covered Areas*. Australia: Butterworths, 1965.

[3] G. D. Aitchison. The quantitative description of the stress deformation behavior of expansive soils. In *Proc. 3rd Int. Conf. Expansive Soils*, 1973.

[4] B. Albers. Analysis of the propagation of sound waves in partially saturated soils by means of a macroscopic linear poroelastic model. *Transp. Porous. Med.*, 80(1), 2009.

[5] B. Albers. *Modeling and Numerical Analysis of Wave Propagation in Saturated and Partially Saturated Porous Media*. Shaker Verlag, 2010.

[6] B. Albers and K. Wilmanski. On modeling acoustic waves in saturated poroelastic media. *J. Engrg. Mech., ASCE*, 131(9), 2005.

[7] W. F. Ames. *Nonlinear Partial Differential Equations in Engineering*. Academic Press, 1965.

[8] L. Andersen and S. R. K. Nielsen. Reduction of ground vibration by means of barriers or soil improvement along a railway track. *Soil Dyn. Earthq. Eng.*, 25: 701–716, 2005.

[9] I. Ashayeri, M. Kamalian, M. K. Jafari, and B. Gatmiri. Analytical 3d transient elastodynamic fundamental solution of unsaturated soils. *Int. J. Numer. Anal. Methods Geomech.*, 35:1801–1829, 2010.

[10] L. Banjai and M. Schanz. Wave propagation problems treated with convolution quadrature and bem. In U. Langer, M. Schanz, O. Steinbach, and W. L. Wendland, editors, *Fast Boundary Element Methods in Engineering and Industrial Applications*, chapter 2. Springer, 2011.

[11] C.G. Bao, B.W. Gong, and L.T. Zhan. Properties of unsaturated soils and slope stability of expansive soils. In *Second International Conference on Unsaturated Soils*. International Academic Publishers, 1998.

[12] J. Bear. *Dynamics of Fluids in Porous Media*. Dover Publications, 1988.

[13] E. Becache, J. C. Nedelec, and N. Nishimura. Regularization in 3d for anisotropic elastoduynamic crack and obstacle problems. *J. Elasticity*, 31:25–46, 1993.

[14] J. G. Berryman. Waves in partially saturated porous media. In W. E. Fitzgibbon and M. F. Wheeler, editors, *Wave Propagation and Inversion*, pages 1–25. SIAM, Philadelphia, 1992.

[15] M. A. Biot. General theory of three–dimensional consolidation. *J. Appl. Phys.*, 12: 155–164, 1941.

[16] M. A. Biot. Theory of propagation of elastic waves in a fluid-saturated porous solid.I. Low-frequency range. *J. Acoust. Soc. Am.*, 28(2):168–178, 1956.

[17] M. A. Biot. Theory of propagation of elastic waves in a fluid-saturated porous solid.II. Higher frequency range. *J. Acoust. Soc. Am.*, 28(2):179–191, 1956.

[18] M. A. Biot. Mechanics of deformation and accoustic propagation in porous media. *J. Appl. Phys.*, 33(4):1482–1498, 1962.

[19] A. W. Bishop. The principle of effective stress. *Teknisk Ukeblad*, 106:859–863, 1959.

[20] A. W. Bishop. The measurement of pore pressure in the triaxial test. In *Proceeding of Conference Pore Pressure and Suction in Soils*. London: Butterworths, 1960.

[21] A. W. Bishop and G. E. Blight. Some aspects of effective stress in saturated and partly saturated soils. *Geotechnique*, 13:177–197, 1963.

[22] A. W. Bishop and A. K. G. Eldin. Undrained triaxial tests on saturated sands and their significance in the general theory of shear strength. *Geotechnique*, 2:13–32, 1950.

[23] G. E. Blight. Flow of air through soils. *J. Soil Mech. Found. Eng. Div.*, 97:607–624, 1971.

[24] R. M. Bowen. Theory of mixtures. In A. Eringen, editor, *Continuum Physics*, chapter 3. Academic Press, 1976.

[25] R. M. Bowen. Incompressible porous media models by use of the theory of mixture. *Int. J. Engng. Sci.*, 18:1129–1148, 1980.

[26] R. M. Bowen. Compressible porous media models by use of the theory of mixtures. *Int. J. Engng. Sci.*, 20:697–763, 1982.

[27] R. H. Brooks and A. T. Corey. Hydraulic properties of porous media. In *Hydraulic Papers*. Colorado State Univ., 1964.

[28] E. Buckingham. *Studies of the Movement of Soil Moisture*. Govt. print. off., 1907.

[29] J. C. Butcher. *The Numerical Analysis of Ordinary Differential Equations*. A Wiley Interscience Publication, 1987.

[30] J. M. Carcione, F. Cavallini, J. E. Santos, C. L. Ravazzoli, and P. M. Gauzellino. Wave propagation in partially saturated porous media: Simulation of a second slow wave. *Wave Motion*, 39:227–240, 2004.

[31] J. Chen and G. F. Dargush. Boundary element method for dynamic poroelastic and thermoelastic analysis. *Int. J. Solids Struct*, 32:2257–2278, 1995.

[32] A. H-D. Cheng and H. Antes. On free space green's function for high order Helmholtz equations. In *Proceedings of the IABEM Symposium*, 1991.

[33] A. H.-D. Cheng, T. Badmus, and D. E. Beskos. Integral equations for dynamic poroelasticity in frequency domain with bem solution. *J. Engrg. Mech., ASCE*, 117: 1136–1157, 1991.

[34] A. H.-D. Cheng, H. Antes, and N. Ortner. Fundamental solutions of products of helmholtz and polyharmonic operators. *Eng. Anal. Bound. Elem.*, 14:187–191, 1994.

[35] E. C. Childs. *An Introduction to the Physical Basis of Soil Water Phenomena*. Wiley–Interscience, 1969.

[36] E. C. Childs and N. C. George. The permeability of porous materials. *Proc. Royal. Soc.*, 201A:392–405, 1950.

[37] L. Collatz. *The Numerical Treatment of Differential Equations*. Springer, 1960.

[38] A. T. Corey and W. D. Kemper. Concept of total potential in water and its limitations. *Soil Sci.*, 91:299–305, 1961.

[39] S. H. Crandall. *Engineering Analysis*. McGraw–Hill, 1956.

[40] T. A. Cruse. An improved boundary–integral equation method for three–dimensional elastic stress analysis. *Comput. Struct.*, 4:741–754, 1974.

[41] H. Darcy. *Histoire Des Foundataines Publique de Dijon*. Dalmont, 1856.

[42] R. de Boer. *Theory of Porous Media*. Springer-Verlag, Berlin, 2000.

[43] G. Degrande, G. De Roeck, and P. Van Den Broeck. Wave propagation in layered dry, saturated and unsaturated poroelastic media. *Int. J. Solids Struct*, 35:4753–4778, 1998.

[44] J. Dominguez. Boundary element approach for dynamic poroelastic problems. *Int. J. Numer. Methods Eng.*, 35:307–324, 1992.

[45] N. E. Edlefsen and A. B. C. Anderson. Thermodynamics of soil moisture. *Hilgardia*, 15:31–298, 1943.

[46] C. A. Fang. *Thermo–mechanical Continuum Theory with Internal Length of Cohesionless Granular Materials*. PhD thesis, TU Darmstadt, 2005.

[47] D. G. Fredlund and N. R. Morgenstem. Stress static variables for unsaturated soils. *J. Geotech. Eng. Div. ASCE*, 103:447–466, 1977.

[48] W. Gardner and J. A. Widtsoe. The movement of soil moisture. *Soil Sci.*, 11:215–232, 1921.

[49] S. K. Garg, A. H. Nafeh, and A. J. Good. Compressional waves in fluid-saturated elastic porous media. *J. Appl. Phys.*, 45(5):1968–1974, 1974.

[50] F. Gassmann. Über die Elastizität poröser Medien. *Viertel. Naturforsch. Ges. Zürich*, 96(1):1–23, 1951.

[51] B. Gatmiri and E. Jabbari. Time-domain Green's functions for unsaturated soils. Part I: Two-dimensional solution. *Int. J. Solids Struct*, 42:5971–5990, 2005.

[52] B. Gatmiri and E. Jabbari. Time-domain Green's functions for unsaturated soils. Part II: Three-dimensional solution. *Int. J. Solids Struct*, 42:5991–6002, 2005.

[53] B. Gatmiri, P. Maghoul, and D. Duhamel. Two–dimensional transient thermo–hydro–mechanical fundamental solutions of multiphase porous media in frequency and time domains. *Int. J. Solids Struct*, 47:595–610, 2009.

[54] M. Goodman and S. Cowin. A continuum theory of granular materials. *Arch. Rat. Mech. Anal.*, 44:249–266, 1972.

[55] K. F. Graff. *Wave Motion in Elastic Solids*. Oxford University Press, 1975.

[56] G. Gudehus and M. Külzer. Einfluss von Ionen und Gasblasen auf die Kollapsneigung feinstkörniger Böden. *Geotechnik*, 25:12–20, 2002.

[57] M. Guiggiani. Formulation and numerical treatment of boundary integral equations with hypersingular kernels. In V. Sladek and J. Sladek, editors, *Singular Integrals in Boundary Element Methods*, pages 85–124. Computational Mechanics Publications, 1998.

[58] M. Guiggiani and P. Casalini. Direct computation of cauchy principle value integrals in advanced boundary elements. *Int. J. Numer. Methods Eng.*, 24:1711–1720, 1987.

[59] N. M. Günter. *Potential Theory, and its Applications to Basic Problems of Mathematical Physics*. Frederick Ungar Publishing, New York, 1967.

[60] H. Han. The boundary integro–differential equations of three–dimensional neumann problem in linear elasticity. *Math. Comput.*, 68:269–281, 1994.

[61] S. M. Hassanizadeh and W. G. Gray. Mechanics and thermodynamics of multiphase flow in porous media including interphase boundaries. *Adv. Water Resources*, 13: 169–186, 1990.

[62] R. Helmig. *Multiphase Flow and Transport Processes in The Subsurface*. Springer, 1997.

[63] H. Hörmander. *Linear Partial Differential Operators*. Springer–Verlag, 1963.

[64] A. Karlström and A. Boström. Efficiency of trenches along railways for trains moving at sub– or supersonic speeds. *Soil Dyn. Earthq. Eng.*, 27:625–641, 2007.

[65] L. Kielhorn. *A Time-Domain Symmetric Galerkin BEM for Viscoelastodynamics*, volume 5 of *Computation in Engineering and Science*. Verlag der Technischen Universität Graz, 2009.

[66] L. Kielhorn and M. Schanz. Convolution quadrature method based symmetric galerkin boundary element method for 3d elastodynamics. *Int. J. Numer. Methods Eng.*, 76:1724–1746, 2008.

[67] N. Kirchner and K. Hutter. Thermodynamic modelling of granular continua exhibiting quasi–static frictional behaviour. In G. P. Capriz and V. Ghionna, editors, *Modelling and Mechanics of Granular and Porous Materials*. Birkhäuser, 2002.

[68] R. Klein, H. Antes, and D. Le Houedec. Efficient 3d modelling of vibration isolation by open trench. *Comput. Struct.*, 64:809–817, 1997.

[69] V. D. Kupradze, T. G. Gegelia, M. O. Basheleishvili, and T. V. Burchuladze. *Three–Dimensional Problems of the Mathematical Theory of Elasticity and Thermoelasticity*. North–Holland, 1979.

[70] T. W. Lambe and R. V. Whitman. *Soil Mechanics*. Wiley, 1979.

[71] R. W. Lewis and B. A. Schrefler. *The Finite Element Method in the Static and Dynamic Deformation and Consolidation of Porous Media*. John Wiley and Sons, Chichester, 1998.

[72] P. Li and M. Schanz. Wave propagation in a 1–d partially saturated poroelastic column. *Geophys. J. Int.*, 184:1341–1353, 2011.

[73] W. Lo, G. Sposito, and E. Majer. Low–frequency dilatational wave propagation through unsaturated porous media containing two immiscible fluids. *Transp. Porous. Med.*, 68:91–105, 2007.

[74] C. Lubich. Convolution quadrature and discretized operational calculus. I. *Numer. Math*, 52:129–145, 1988.

[75] C. Lubich. Convolution quadrature and discretized operational calculus. II. *Numer. Math*, 52:413–425, 1988.

[76] C. Lubich. On the multistep time discretization of linear initial–boundary value problems and their boundary integral equations. *Numer. Math*, 67:365–389, 1994.

[77] P. Maghoul, B. Gatmiri, and D. Duhamel. Three–dimensional transient thermo–hydro–mechanical fundamental solutions of unsaturated soils. *Int. J. Numer. Anal. Methods Geomech.*, 34:297–329, 2010.

[78] V. Mantic. A new formula for the c-matrix in the somigliana identity. *J. Elasticity*, 33:191–201, 1993.

[79] A. W. Maue. Zur Formulierung eines allgemeinen Beugungsproblems durch eine Integralgleichung. *Z. Phys.*, 126:601–618, 1949.

[80] H. Meissner and A. Becker. Dynamic behaviour of partially saturated sand. *T. Built Environ.*, 14:45–55, 1995.

[81] M. Messner and M. Schanz. A regularized collocation boundary element method for linear poroelasticity. *Comput. Mech.*, 47:669–680, 2011.

[82] M. Messner, M. Messner, F. Rammerstorfer, and P. Urthaler. Hyperbolic and elliptic numerical analysis bem library. http://www.mech.tugraz.at/HyENA, 2010.

[83] I. Müller. *Thermodynamics*. Pitman, 1985.

[84] K. K. Muraleetharan and C. Wei. Dynamic behaviour of unsaturated porous media: Governing equations using the theory of mixtures with interfaces (TMI). *Int. J. Numer. Anal. Methods Geomech.*, 23(13):1579–1608, 1999.

[85] W.F. Murphy. Effects of partial water saturation on attenuation in Massilon sandstone and Vycor porous glass. *J. Acoust. Soc. Am.*, 71, 1982.

[86] W.F. Murphy. Acoustic measures of partial gas saturation in tight sandstones. *J. Geophys. Res.*, 89(B13), 1984.

[87] J. Nedelec. Integral equations with non integrable kernels. *Integer. Equat. Oper. Th.*, 5:563–672, 1982.

[88] J. Nie, D. Yang, and H. Yang. Wave dispersion and attenuation in partially saturated sandstones. *Chin. Phys. Lett.*, 21:572–575, 2004.

[89] N. Nishimura and S. Kobayashi. A regularized boundary integral equation method for elastodynamic crack problems. *Comput. Mech.*, 4:319–328, 1989.

[90] C. L. Pekeris. The seismic surface pulse. *Proc. Nat. Acad. Sci. U.S.A.*, 41:469–480, 1955.

[91] A. J. Philippacopoulos. Waves in partially saturated medium due to surface loads. *J. Engrg. Mech., ASCE*, 114(10):1740–1759, 1988.

[92] N. Ravichandran and K. K. Muraleetharan. Dynamics of unsaturated soils using various finite element formulations. *Int. J. Numer. Anal. Methods Geomech.*, 33(5): 611–631, 2009.

[93] J. W. S. Rayleigh. On waves propagated along the plane surface of an elastic solid. *Proc. London Math. Soc.*, 17:4–11, 1887.

[94] L. A. Richards. The usefulness of capillary potential to soil moisture and plant investigators. *J. Agric. Res.*, 37:719–742, 1928.

[95] L. A. Richards. The significance of moisture flow and equilibria in unsaturated soils inrelation to the design of engineering structures built on shallow foundations in Australia. In *Sym. Permeability and Capillarity*. ASTM, 1966.

[96] L. A. Richards and G. Ogata. A thermocouple for vapour pressure measurement in biological and soil systems at high humidity. *Science*, 128:1089–1090, 1958.

[97] F. E. Richart, J. R. Hall, and R. D. Woods. *Vibrations of Soils and Foundations*. Prentice–Hall, 1970.

[98] V. Sarihan and S. Mukherjee. Axisymmetric viscoplastic deformation by the boundary element method. *Int. J. Solids Struct*, 18:1113–1128, 1982.

[99] S. A. Sauter and C. Lage. Transformation of hypersingular integrals and black–box cubature. *Math. Comput.*, 70:223–250, 2001.

[100] M. Schanz. *Wave Propagation in Viscoelastic and Poroelastic Continua: A Boundary Element Approach*, volume 2 of *Lecture Notes in Applied Mechanics*. Springer-Verlag, Berlin, Heidelberg, New York, 2001.

[101] M. Schanz. Poroelastodynamics: Linear models, analytical solutions, and numerical methods. *AMR*, 62(3):030803–1–030803–15, 2009.

[102] M. Schanz and A. H.-D. Cheng. Transient wave propagation in a one-dimensional poroelastic column. *Acta Mech.*, 145(1-4):1–18, 2000.

[103] M. Schanz and L. Kielhorn. Dimensionaless variables in a poroelastodynamic time domain boundary element formulation. *Build. Res. J.*, 53:175–189, 2005.

[104] B. A. Schrefler and R. Scotta. A fully coupled dynamic model for two-phase fluid flow in deformable porous media. *Comput. Methods Appl. Mech. Engrg.*, 190(24–25), 2001.

[105] J. F. Semblat and A. Pecker. *Waves and Vibrations in Soils: Earthquakes, Traffic, Shocks, Construction Works*. IUSS Press, 2009.

[106] A. W. Skempton. Effective stress in soils, concrete and rocks. In *Proceeding of Conference Pore Pressure and Suction in Soils*. London: Butterworths, 1961.

[107] D. Smeulders, J. De La Rosette, and M. Van Dongen. Waves in partially saturated porous media. *Transp. Porous. Med.*, 9(1–2), 1992.

[108] O. Steinbach. *Numerical Approximation Methods for Elliptic Boundary Value Problems*. Springer, 2008.

[109] K. Terzaghi. *Theoretical Soil Mechanics*. Wiley, 1943.

[110] S. D. Thomas. A finite element model for the analysis of wave induced stresses, displacements and pore pressures in an unsaturated seabed I: Theory. *Comput. Geotech*, 8:1–38, 1989.

[111] S. D. Thomas. A finite element model for the analysis of wave induced stresses, displacements and pore pressures in an unsaturated seabed II: Model verification. *Comput. Geotech*, 17:107–132, 1995.

[112] C. A. Truesdell. *Rational Thermodynamics*. Springer, 1984.

[113] M. Th. van Genuchten. A closed-form equation for predicting the hydraulic conductivity of unsaturated soils. *Soil Sci. Soc. Am. J*, 44, 1980.

[114] D. Velea, F. D. Shields, and J. M. Sabatier. Elastic wave velocities in partially saturated ottawa sand: Experimental results and modeling. *Soil Sci. Soc. Am. J*, 64: 1226–1234, 2000.

[115] I. Vgenopoulou and D. E. Beskos. Dynamics of saturated rocks. IV: Column and borehole problems. *J. Engrg. Mech., ASCE*, 118(9):1795–1813, 1992.

[116] Z. Wang, Y. Lu, and H. Hao. Numerical investigation of effects of water saturation on blast wave propagation in soil mass. *J. Engrg. Mech., ASCE*, 130:551–561, 2004.

[117] J. O. Watson. Effective numerical treatment of boundary integral equations: A formulation for three–dimensional elastostatics. *Int. J. Numer. Methods Eng.*, 10: 991–1005, 1976.

[118] J. O. Watson. Advanced implementation of the boundary element method for two– and three–dimensional elastostatics. In P. K. Banerjee and P. Butterfield, editors, *Developments in Boundary Element Methods-I*, chapter Ch.3, pages 31–63. Applied Science Publishers, 1979.

[119] C. Wei and K. K. Muraleetharan. A continuum theory of porous media saturated by multiple immiscible fluids: I. Linear poroelasticity. *Int. J. Engng. Sci.*, 40(16): 1807–1833, 2002.

[120] C. Wei and K. K. Muraleetharan. A continuum theory of porous media saturated by multiple immiscible fluids: II. Lagrangian description and variational structure. *Int. J. Engng. Sci.*, 40(16):1835–1854, 2002.

[121] K. Wilmanksi. *Thermomechanics of Continua*. Springer, 1998.

[122] K. Wilmanski. Porous media at finite strains–the new model with the balance equation for porisity. *Arch. Mech.*, 48:591–628, 1996.

[123] K. Wilmanski. A thermodynamic model of compressible porous materials with the balance equation of porosity. *Transp. Porous. Med.*, 32:21–47, 1998.

[124] K. Wilmanski. Thermodynamical admissibility of biot's model of poroelastic saturated materials. *Arch. Mech.*, 54:5–6, 2002.

[125] K. Wilmanski. Tortuosity and objective relative accelerations in the theory of porous materials. *Proc. R. Soc. A*, 461:1533–1561, 2005.

[126] K. Wilmanski. Elastic modelling of surface waves in single and multicomponent systems. In C. G. Lai and K. Wilmanski, editors, *Surface Waves in Geomechanics: Direct and Inverse Modelling for Soils and Rocks*, volume 481 of *CISM*, chapter 5, pages 203–276. Springer-Verlag, Wien, 2005.

[127] K. Wilmanski. A few remarks on biot's model and linear acoustics of poroelastic saturated materials. *Soil Dyn. Earthq. Eng.*, 26:509–536, 2006.

[128] R. K. Wilson and E. C. Aifantis. On the theory of consolidation with double porosity. *Int. J. Engng. Sci.*, 20:1009–1035, 1982.

[129] R. D. Woods. Screening of surface waves in soils. *J. Soil Mech. Found. Eng. Div.*, 94:951–979, 1968.

[130] J. Yang. Influence of water saturation on horizontal and vertical motion at a porous soil interface induced by incident p wave. *Soil Dyn. Earthq. Eng.*, 19:575–581, 2000.

[131] O. C. Zienkiewicz, A. H. C. Chan, M. Pastor, D. K. Paul, and T. Shiomi. Static and dynamic behaviour of soils: A rational approach to quantitative solutions. I. fully saturated problems. *Proc. R. Soc. Lond. A*, 429(1877):285–309, 1990.

[132] O. C. Zienkiewicz, Y. M. Xie, B. A. Schrefler, A. Ledesma, and N. Bicanic. Static and dynamic behaviour of soils: A rational approach to quantitative solutions. II. semi–saturated problems. *Proc. R. Soc. Lond. A*, 429(1877):311–321, 1990.